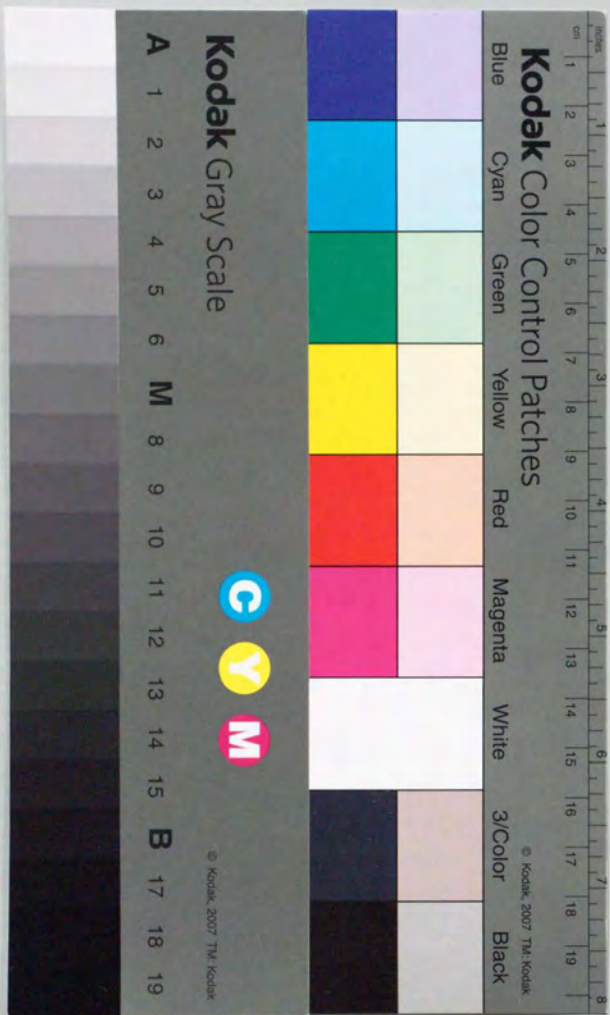


Measurement of Neutrinos
and Search for Anti-Neutrinos
from the Sun at Kamiokande
神岡実験における太陽ニュートリノの測定
および太陽反ニュートリノの探索

Kunio INOUE
井上邦雄



①

Acknowledgment

Measurement of Neutrinos and Search for Anti-Neutrinos from the Sun at Kamiokande

Kunio Inoue

December 1993

A DISSERTATION

in

PHYSICS

The University of Tokyo

Acknowledgment

First of all, my sincere appreciation goes to my advisor, Professor Yoichiro Suzuki. He introduced me to experimental physics and his serious attitude toward physics always refreshed me. I will never forget the exciting R&D in my master course with him, which was my first work in experimental physics. Without his excellent guidance and encouragement on many occasions, this thesis would never have been completed.

I would like to thank Professor Yoji Totsuka, spokesman of Kamiokande experiment, for accepting me to work at ICRR. His deep insight into physics and experiments was indispensable to the Kamiokande experiment. I also thank Professor Kenzo Nakamura, who is the leader at Kamioka, for managing and keeping the Kamiokande experiment in a good state. I wish to thank Professor T.Kajita for his excellent leadership in the upgrading to Kamiokande-3. The light reflector is his idea.

I am grateful to Professor M.Koshihara, who is the former leader and the father of the Kamiokande experiment, for his initiation of the experiment. Thanks also go to the late Professor T.Suda, who is the former leader at Kamioka, for his efforts in designing and operating the experiment.

I would like to thank Dr.M.Nakahata for his kind instruction in the operation of the computer and in solar neutrino analysis. He established the solar neutrino analysis in Kam-2. I am also indebted to members of the low energy analysis group, Dr.Y.Fukuda, T.Ishida, A.Sakai, and Y.Koshihara who manages daily analysis on solar neutrinos, and J.Suzuki from ICRR, Y.Takeuchi from TIT, and Dr.K.S.Hirata and Dr.K.Kihara from KEK. They shared the hard jobs of solar neutrino analysis, manipulating huge amounts of low energy data.

I would like to thank Professor A.Suzuki for his excellent ideas and work on the water purification system. His work in lowering the low energy background was indispensable to the solar neutrino analysis in Kamiokande. I would like to express special thanks to my collaborators at Osaka university, where I spent my first 2 years of graduate school; Professor Y.Nagashima who was my advisor in my master course,

and Dr.M.Takita who is managing the H.V. system and the water purification system in Kamiokande-3. They taught me many things on many occasions.

My great appreciation also goes to all the other collaborators and research fellows for their hard works on the experiment and for their useful discussions: Dr.T.Kumita, T.Hayakawa, M.Shiozawa, S.Jokou, S.Kasuga and K.Matsumoto from ICRR; Dr.M.Mori (expert of Kam-3 electronics), Dr.Y.Oyama and Dr.M.Yamada from KEK; Dr.K.Nishijima from Tokai university; T.Kajimura and Dr.Atsumu Suzuki from Kobe university; Dr.H.Takei, M.Koga, Professor K.Miyamo, Dr.H.Miyata, T.Ishizuka and H.Okazawa from Niigata university; T.Hara (expert of H.V. system), A.Yoshimoto, N.Kishi and T.Yamaguchi from Osaka university; K.Kaneyuki, and Professor T.Tanimori (expert of Kam-3 electronics) from TIT; Professor S.Tasaka (expert of SSD radon monitor system) from Gifu university; Professor K.Nishikawa from INS; and Professor E.W.Berier, Dr.E.D.Frank, Professor W.Frati, Dr.S.B.Kim, Professor A.K.Mann, F.M.Newcomer, R.Van.Berg, and Dr.W.Zhang from the PENN group for their great contributions to the Kamiokande-2 experiment. I also owe thanks to collaborators in early stage of the Kamiokande experiment for their help with constructions and developments.

I gratefully acknowledge the cooperation of the Kamioka Mining and Smelting Company.

Most of the analysis has been made on the FACOM M780 of INS, University of Tokyo. I wish to thank the staff in the computer room for their help.

Abstract

The Kamiokande-III solar neutrino observation started in December 1990 and has accumulated 514 days of data until February 1993. The ^8B solar neutrino flux observed in Kam-3 was $\frac{\text{data}}{\text{SSM}_{\text{BP92}}} = 0.574^{+0.064}_{-0.059}$ (stat) ± 0.061 (syst), which yields $0.514^{+0.043}_{-0.037} \pm 0.061$ combined with 1043 days of the Kam-2 data. The solar neutrino problem still remains.

The neutrino oscillation solution for the problem was investigated using these data, together with the data from other solar neutrino experiments. Non-adiabatic and quasi-vacuum solutions can reconcile all available experimental results except for a possible time variation in the ^{37}Cl experiment, and the "just-so" vacuum oscillation solution was excluded by these results.

The combined Kamiokande data from 1557 days of observation covers an entire solar maximum period. No significant correlation between the flux and the sun-spot numbers was found in these data. A hybrid solution assuming Majorana neutrinos was explored in order to explain simultaneously the anti-correlation between the flux and the sun-spot numbers indicated in the ^{37}Cl experiment and no such correlation in the Kamiokande data, and four regions depending on the profile of the magnetic field in the sun were obtained as hybrid model solutions: (s1) $\sin^2 2\theta \sim 1$, $\delta m^2 \sim 2 \times 10^{-9} \text{ eV}^2$ for an Akhmedov type profile with B_1 (radiation zone) $\leq 1 \text{ MGauss}$ (assuming $\mu_\nu = 10^{-11} \mu_B$); (s2) $\sin^2 2\theta \sim 0.01$, $\delta m^2 \sim 6 \times 10^{-8} \text{ eV}^2$ for an Akhmedov type profile, but with $B_1 \sim 3 \text{ MGauss}$; (s3) $\sin^2 2\theta \lesssim 6 \times 10^{-2}$, $\delta m^2 \sim 10^{-8}$ for a flat field in $0.65 < r/R_{\text{sun}} < 1$, and zero in $r/R_{\text{sun}} < 0.65$; and (s4) $\sin^2 2\theta \lesssim 3 \times 10^{-2}$, $\delta m^2 \sim 10^{-8}$ for a flat field in the sun $0 < r/R_{\text{sun}} < 1$. These solutions require the time-varying magnetic field in the convection zone such that from 20 kGauss to 50 kGauss.

The data also yielded a spectrum-independent $\bar{\nu}_e$ flux limit at the solar maximum time as $4.5\% \times \text{MeV}$ at $E_\nu = 12.5 \text{ MeV}$ with respect to the expected ^8B solar neutrino flux. A much stricter limit was obtained when specific models such as (s1)-(s4) above were considered, such that an $O(1\%)$ transition of ^8B neutrinos into $\bar{\nu}_e$ was excluded.

Assuming a hybrid model with Majorana neutrinos, an excluded region in the δm^2 - $\sin^2 2\theta$ plane was obtained for the following profiles of the solar magnetic field: (e1) for B (radiation zone) $\geq 3 \text{ MGauss}$, $10^{-7} \leq \delta m^2 \leq 10^{-4}$, $10^{-1.4} \leq \sin^2 2\theta \leq 10^{-0.4}$, and (e2) for B (convection zone) $\geq 50 \text{ kGauss}$, $\sin^2 2\theta \geq 10^{-1.5}$, $\delta m^2 \leq 10^{-6.5}$. The excluded region (e2) overlaps with the obtained hybrid model solution with large mixing (s1), and therefore is completely excluded, but the other hand, the small mixing solutions (s2), (s3) and (s4) survive against (e1) and (e2).

Contents

| | |
|--|----|
| 1. Introduction | 1 |
| 1.1. Overview | 1 |
| 1.2. Solar Neutrinos | 3 |
| 1.3. Experimental Situation and Solar Neutrino Problem | 7 |
| 1.3.1. ^{37}Cl experiment | 7 |
| 1.3.2. The Kamiokande-II experiment | 9 |
| 1.3.3. The SAGE and GALLEX experiments (^{71}Ga experiments) | 10 |
| 1.3.4. Summary of the current solar neutrino experiments | 12 |
| 1.3.5. A problem in SSM? | 13 |
| References | 14 |
| 2. Neutrino Mass and Magnetic Moment | 17 |
| 2.1. Neutrino Mass Limits | 17 |
| 2.2. Limits on Magnetic Moment | 18 |
| References | 20 |
| 3. Neutrino Oscillation and Resonant Spin Flavor Precession | 21 |
| 3.1. Neutrino Oscillation in Vacuum | 21 |
| 3.2. Neutrino Oscillation in Matter (MSW) | 24 |
| 3.3. Resonant Spin Flavor Precession (RSFP) | 30 |
| 3.4. Hybrid Model (RSFP+MSW) | 32 |
| References | 34 |
| 4. The Kamiokande-III detector | 35 |
| 4.1. Short history of Kamiokande | 35 |
| 4.2. Ring imaging water Cherenkov detector | 36 |
| 4.3. Neutrino interactions in Kamiokande | 38 |
| 4.3.1. Dominant processes in the energy region of solar neutrinos | 38 |
| 4.3.2. Neutrino-electron elastic scattering | 39 |
| 4.3.3. Capture cross section of a free proton for $\bar{\nu}_e$ | 41 |
| 4.4. Water tank | 42 |
| 4.5. Photo multiplier tube ($20''\phi$ PMT) | 43 |
| 4.5.1. Improvement of PMTs for Kamiokande-III | 43 |
| 4.5.2. Light reflector | 44 |
| 4.5.3. High Voltage monitoring system | 45 |

| | |
|--|-----|
| 4.6. Electronics | 46 |
| 4.6.1. Electronics for Kamiokande-III | 47 |
| 4.6.2. Trigger | 50 |
| 4.7. Background from Radon contamination | 51 |
| 4.7.1. General description | 51 |
| 4.7.2. Water purification system | 52 |
| 4.7.3. Radon-free air system | 54 |
| 4.7.4. Radon measurement | 55 |
| References | 58 |
| 5. Data analysis | 61 |
| 5.1. Event reconstruction | 62 |
| 5.1.1. Fast vertex reconstruction | 62 |
| 5.1.2. Precise vertex reconstruction | 63 |
| 5.1.3. Direction reconstruction | 65 |
| 5.1.4. Energy reconstruction | 65 |
| 5.1.5. Muon track reconstruction | 68 |
| 5.2. Detector simulation | 69 |
| 5.2.1. Particle transport | 70 |
| 5.2.2. Cherenkov photon propagation | 70 |
| 5.2.3. Tuning of the detector simulation | 71 |
| 5.3. Data reduction and Background | 73 |
| 5.3.1. Muon reduction | 74 |
| 5.3.2. Event reconstruction and Fiducial volume cut | 75 |
| 5.3.3. Spallation cut | 77 |
| 5.3.4. Gamma ray cut | 80 |
| 5.3.5. Consideration of the remaining background | 81 |
| References | 85 |
| 6. Results | 87 |
| 6.1. Solar neutrino flux | 87 |
| 6.1.1. Signal extraction | 87 |
| 6.1.2. ^8B solar neutrino flux | 90 |
| 6.2. Systematic errors for the solar neutrino flux calculation | 92 |
| 6.3. Neutrino flux in correlation with the sun-spot number | 96 |
| 6.3.1. Anti-correlation in the ^{37}Cl experiment | 96 |
| 6.3.2. 200 days plot | 97 |
| 6.3.3. Correlation of the ^8B neutrino flux with the sun-spot numbers | 99 |
| 6.4. Anti-neutrino flux | 100 |
| 6.4.1. Spectrum independent $\bar{\nu}_e$ flux limit | 100 |

| | |
|---|-----|
| 6.4.2. Systematic errors for the $\bar{\nu}_e$ flux limit..... | 102 |
| References..... | 103 |
| 7. Interpretation and Discussions..... | 105 |
| 7.1. The "standard" interpretation of the solar neutrino deficit..... | 105 |
| 7.1.1. MSW solution..... | 105 |
| 7.1.2. Just-so oscillation solution..... | 107 |
| 7.2. Hybrid Solution..... | 108 |
| 7.2.1. Numerical calculation of neutrino propagation..... | 109 |
| 7.2.2. Allowed region for the non-time-variation solution with a magnetic field..... | 113 |
| 7.2.3. Allowed region of the hybrid solution..... | 114 |
| 7.3. Implication of the $\bar{\nu}_e$ flux limit to the hybrid solution..... | 117 |
| 7.3.1. $\bar{\nu}_e$ creation in the hybrid model..... | 117 |
| 7.3.2. Excluded region of hybrid model..... | 118 |
| References..... | 119 |
| 8. Conclusion & Summary..... | 121 |
| Appendix A. PMTs for Kamiokande-II..... | 125 |
| References..... | 127 |
| Appendix B. Electronics for Kamiokande-II..... | 128 |
| References..... | 130 |
| Appendix C. Calibration & Stability Check..... | 131 |
| C.1. Energy Calibration..... | 131 |
| C.1.1. Ni(n, γ)Ni' calibration..... | 131 |
| C.1.2. μ -e decay..... | 134 |
| C.2. Timing Calibration..... | 134 |
| C.3. Transparency of the water..... | 136 |
| C.4. Gain Stability..... | 138 |
| C.5. Dead tubes..... | 138 |
| References..... | 139 |
| Appendix D. Future Prospects..... | 140 |
| References..... | 144 |
| Table and Figure Captions..... | 147 |

Introduction

The solar neutrino problem has been a major puzzle in particle physics and astrophysics for several decades. The standard solar model (SSM) predicts a flux of solar neutrinos that is significantly higher than what is observed by experiments like Kamiokande-II and Super-Kamiokande. This discrepancy has led to the development of various theoretical models to explain the deficit, including neutrino oscillations and magnetic field effects in the solar interior.

This report presents a detailed study of the solar neutrino problem, focusing on the hybrid solution and its implications. It includes a comprehensive review of the experimental data, a theoretical analysis of the neutrino propagation in the solar interior, and a discussion of the allowed regions for the hybrid solution. The report also includes a detailed description of the Kamiokande-II experiment, including the PMTs, electronics, calibration, and stability checks.

The report is organized as follows: Chapter 6 discusses the systematic errors for the $\bar{\nu}_e$ flux limit. Chapter 7 provides an interpretation and discussion of the solar neutrino deficit, including the standard interpretation, the MSW solution, the just-so oscillation solution, and the hybrid solution. Chapter 8 concludes the report with a summary of the findings. Appendixes A through D provide detailed information about the Kamiokande-II experiment, including the PMTs, electronics, calibration, and future prospects.

1. Introduction

1.1. Overview

The Sun is known as a standard main sequence star and is theoretically predicted that nuclear fusion reactions at the center, called as p-p chain, maintain its luminosity. The first confirmation of the energy generation by the nuclear fusion reactions was made by Davis et al [ref 1-1]. They have performed an experiment to measure neutrinos produced in the sun with ^{37}Cl detector. Their experiment, lasting for more than 20 years, has yielded the results that the counting rate of neutrinos is only a quarter to a half [ref 1-2] of the theoretical predictions from any standard solar model (SSM) [ref 1-3,1-4,1-5]. This is so-called the "Solar Neutrino Problem." The Kamiokande-II solar neutrino experiment, started in 1987, also observed such a neutrino deficit [ref 1-6,1-7]. Kamiokande can obtain directional information of the incoming neutrinos and the energy spectrum of recoil electrons on an event by event basis. Due to this advantage, Kamiokande has obtained the first evidence that neutrinos really come from the sun, although the observed solar neutrino flux [ref 1-8] is about a half of the SSM prediction. The recent ^{71}Ga experiments, SAGE [ref 1-9,1-10] and Gallex [ref 1-11,1-12], also reported a smaller solar neutrino flux than the SSM prediction.

In order to explain the solar neutrino problem, many approaches such as modifications of the SSM (low Z modelⁱ, WIMPsⁱⁱ and so on) and neutrino oscillations with finite mass of the neutrino which is a clue that a theory beyond the standard electro-weak theory exists, have been proposed [ref 1-13]. We know that a modification of the solar model does not change the spectrum shape of solar neutrinos in any neutrino production processes. Any approach of SSM modification is hard to reconcile with the flux measured by the ^{37}Cl experiment and that from the Kamiokande

ⁱ A low Z model assumes a solar composition of which the mean atomic number is smaller than that of the SSM. Such operation lowers the opacity of the sun, and finally causes a lower temperature of the solar core.

ⁱⁱ Weakly Interacting Massive Particles (WIMPs) effectively take out the energy from the core to the surface of the sun, and as a result, the temperature of the solar core is degraded.

experiment. The most convincing model that explains the neutrino deficit is the matter enhanced neutrino oscillation model (MSW effect [ref 1-14,1-15]) which needs neutrino mass and mixing.

On the other hand, it is very interesting to point out that the ^{37}Cl experiment suggested a 11 year time variation of the neutrino flux [ref 1-16]. It seems to have an anti-correlation with the solar activity. Such time variation implies new features of neutrinos such as a magnetic moment. However, Kamiokande-II does not have any significant time variation [ref 1-17]. It is interesting to try to reconcile the time variation observed in the ^{37}Cl experiment and no time variation in Kamiokande. As a special case, just-so oscillation [ref 1-18] (long oscillation length comparable to one astronomical unit) and the earth effect may cause seasonal variation and day/night flux variation, respectively. But, neutrino oscillations generally cannot yield a time variation such as 11 year time variation indicated by the ^{37}Cl experiment. The most plausible solution for the anti-correlation would be a spin flavor precession of neutrinos because it is believed that the solar magnetic field in the convection zone of the sun changes with the periodicity of 22 years. One might expect that the 11 year periodicity of the solar activity or the sunspot number should be caused by the change of the magnetic field in the convection zone, because sunspots are the places where the strong magnetic field is concentrated. If neutrinos have a magnetic moment, they can be converted from left-handed neutrinos to undetectable (with the ^{37}Cl detector) right-handed neutrinos through a magnetic interaction with the solar magnetic field. Okun first pointed out in 1986 [ref 1-19] a scenario in which a reasonable reduction and a time variation of the solar neutrino flux are possible, with a rather large neutrino magnetic moment, $\mu_\nu \sim (0.3-1.0) \times 10^{-10} \mu_B$ with $B_{\text{sun}} \sim 10^3-10^4$ Gauss. The scenario was later revised to include the resonant effect of a spin-flavor precession. Assuming the magnetic moment of $\mu_\nu B = 10^{-10} \mu_B k \text{Gauss}$, a finite neutrino mass and a flavor mixing, one could expect that the resonant spin-flavor precession gives rise to an anti-correlation with the sunspot numbers due to the time varying magnetic field and reduces the average flux of neutrinos simultaneously. Such an attractive mechanism called as a Hybrid-model, was

first proposed by Lim and Marciano [ref 1-20], and Akhmedov [ref 1-21] in 1988. Following that, extended models were vigorously explored [ref 1-22].

Some hybrid models assuming transition magnetic moments of Majorana type neutrinos predict an interesting $\bar{\nu}_e$ creation. It may be observable in the Kamiokande detector considering that the cross section of $\bar{\nu}_e p$ is about two orders of magnitude larger than that of $\nu_e e$.

In April 1990, the Kamiokande-II experiment was stopped and the detector was upgraded by the replacement of dead PMTs, by placing light reflectors around the inner PMTs to increase the photo-coverage, and by installing the new electronics. We resumed the solar neutrino observation in December 1990, and we have continued to take the solar neutrino data which now covers an entire active period in the solar cycle 22.

In this thesis, we show the Kamiokande-III solar neutrino data covering the entire solar maximum period which enabled us to study a time variation in correlation with the sunspot numbers in detail. A solar $\bar{\nu}_e$ flux limit was first obtained in this thesis. With high statistics data now available (combined data from Kam-2 and Kam-3), we evaluated the MSW solution and the Just-so neutrino oscillation solution. Extensive study was made of a solution of hybrid models ($\sin^2 2\theta$, δm^2 and $\mu_\nu B$) to reconcile all of the existing experiments including their time dependence. A limit for the $\bar{\nu}_e$ flux will constrain an allowed region of $\sin^2 2\theta$, δm^2 and $\mu_\nu B$, for a hybrid model.

1.2. Solar Neutrinos

The Sun is the nearest star to the earth and we know its properties much better than any other star. The distance from the earth is 1.5×10^{11} m, its age is 4.6 billion years and its luminosity is 3.86×10^{33} erg/sec. Its mass, radius and surface temperature are 1.99×10^{33} g, 6.96×10^8 m and 5.78×10^3 °K, respectively. Its surface chemical components are also known precisely by the measurements of an absorption spectrum and so on. The Sun is a standard main sequence star. This fact is important in

understanding the detailed mechanism of the evolution of stars. We can justify a theory of star evolution by testing whether the theory can reproduce the present sun. Unfortunately, precise measurements have been done only on the surface phenomena of the sun, and therefore the observation of its interior has been desired very much. We now have two completely different methods to investigate the interior of the sun: one is helioseismology and the other is a solar neutrino observation.

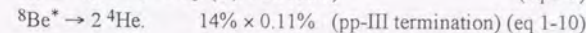
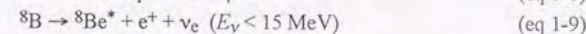
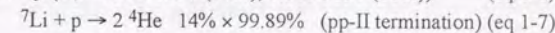
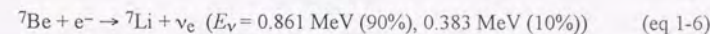
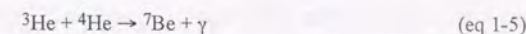
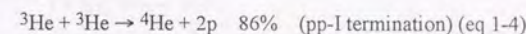
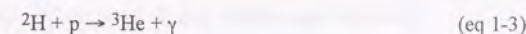
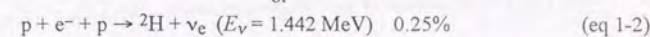
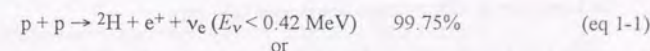
Helioseismology [ref 1-23] brings us the information of a rather shallow part of the sun, such as the depth of the convection zone (about $0.3R_{sun}$ from the surface), by the accurate measurement of oscillations of its surface. It is known that the energy production by fusion reactions takes place at the center of the sun ($\leq 0.3R_{sun}$). Such a deep region is hardly tested by helioseismology.

It takes millions of years for photons to emerge on the surface, possibly bringing information from the center of the sun. If we only have the method of optical observation then we will know millions of years from now what is happening now at the center of the sun. On the other hand, neutrinos have so small a cross section that neutrinos created in the series of the fusion reactions at the center can traverse the sun at light speed within a couple of seconds. We can then obtain real-time information on the center of the sun through the neutrino observation.

Solar neutrino observation is very important to study neutrino properties because solar neutrinos are pure electron neutrinos with energy below 18 MeV and their intensity is strong (6.6×10^{10} /cm²/sec at the earth). Another advantage is that the distance from the earth (observer) to the sun (source) is 1.5×10^{11} m which is extraordinary longer than that achieved in terrestrial experiments. In laboratory experiments we can produce $\bar{\nu}_e$ from a reactor or mainly ν_μ at high energy accelerators, and we can place the detector up to several hundred meters distant (at most, the diameter of the earth, 12800 km, is the limit). The study of the solar neutrino, therefore, enables us to search for a neutrino mixing at very small mass region ($\delta m^2 \geq 10^{-12} \text{eV}^2$). The neutrinos traverse the matter (the density changes from ~ 150 to 0 g/cm^3) through a very long distance (about 7×10^8 m, radius of the sun), and hence the

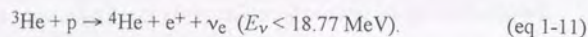
matter effect plays an important role in a very wide parameter region ($10^{-8} \leq \delta m^2 \leq 10^{-4}$, $\sin^2 2\theta \geq 10^{-4}$). Solar neutrinos also traverse a possible strong magnetic field, which is expected to be greater than 1 kGauss in the sun, and we are able to investigate the magnetic properties of the electron neutrino and the profile of the magnetic field in the sun. Therefore, solar neutrino observation is a good probe to study neutrino properties such as a mass and a magnetic moment.

The "Standard Solar Model-s (SSM)s" have been obtained by several authors. But we will use the solar neutrino spectrum in the thesis of Bahcall and Pinsonneault in 1992 (BP92) [ref 1-5] unless otherwise indicated. The solar luminosity is maintained by the p-p chain taking place at the center of the sun. There exists also the CNO cycle as side reactions. The p-p chain has three branches called pp-I, pp-II and pp-III. Those relevant reactions are (reaction flow is shown in Fig. 1.1):



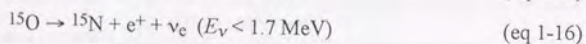
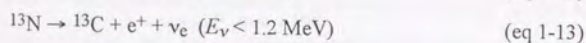
The fluxes for the neutrinos from p-p and pep reactions are 6.00×10^{10} /cm²/sec and 1.43×10^8 /cm²/sec, respectively, and the theoretical errors for those fluxes are small (2% and 4% at 3σ level) since the luminosity of the sun is closely related to the pp-fusion process. The flux of ⁷Be neutrinos is 4.89×10^9 /cm²/sec and the theoretical

error of the flux 18% (3σ) is rather large. The ^8B neutrino is the energetic one and is the only neutrino from the sun which the Kamiokande detector can measure, and the flux of ^8B neutrinos is estimated to be 5.69×10^6 /cm²/sec (recent calculation by Bahcall [ref 1-24] indicates a 7.5% increase of the flux). The theoretical error for the flux, 43% (3σ), is larger than that for other neutrinos because of the large uncertainty of 28% (3σ) for the capture cross section of $^7\text{Be} + p \rightarrow ^8\text{B} + \gamma$ and a small branching ratio to the pp-III chain. There is also an unique reaction called the hep reaction in the p-p chain. The hep reaction emits the most energetic neutrino through the following process:

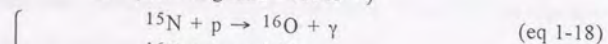


But, the expected flux is too small (1.23×10^3 /cm²/sec at the earth) to be observed at the Kamiokande detector. Only an upper limit is obtained for the hep neutrino flux from the Kamiokande solar neutrino observation [ref 1-25].

The CNO chain consists of the following reactions (Fig. 1.2):



or (branching ratio $\sim 4 \times 10^{-4}$)



The fluxes of the neutrinos from the CNO cycle have large uncertainties because those reactions are side reactions and do not play an important role on the luminosity of the sun. The fluxes of ^{13}N , ^{15}O and ^{17}F neutrinos are predicted to be 4.92×10^8 , 4.26

$\times 10^8$ and 5.39×10^6 /cm²/sec and the theoretical errors for them are 51%, 58% and 48% (3σ), respectively.

In summary, neutrinos from the sun predicted by the SSM (BP92) are as follows:

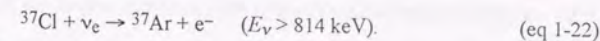
| | Energy (MeV) | Flux at the earth (/cm ² /sec) | 3σ error (%) |
|-----------------|------------------------|---|---------------------|
| p-p | < 0.42 | 6.00×10^{10} | 2 |
| pep | 1.442 | 1.43×10^8 | 4 |
| ^7Be | 0.861(90%), 0.383(10%) | 4.89×10^9 | 18 |
| ^8B | < 15 | 5.69×10^6 | 43 |
| hep | < 18.77 | 1.23×10^3 | - |
| ^{13}N | 1.2 | 4.92×10^8 | 51 |
| ^{15}O | 1.7 | 4.26×10^8 | 58 |
| ^{17}F | 1.7 | 5.39×10^6 | 48 |

Expected solar neutrino spectrum from the SSM are shown in Fig. 1.3.

1.3. Experimental Situation and Solar Neutrino Problem

1.3.1. ^{37}Cl experiment [ref 1-1,1-2]

The first observation of solar neutrinos has been conducted by Davis et al. beginning in the early 1970's. Their detector is located 1480 meters underground in the Homestake Gold Mine in South Dakota, USA. They prepared 3.8×10^5 liters (615 metric-tons) of perchloroethylene (C_2Cl_4) containing about 2.3×10^{30} of ^{37}Cl atoms. ^{37}Cl captures an electron neutrino with an energy larger than 814 keV;



Then, produced ^{37}Ar decays back to ^{37}Cl through electron capture with $T_{1/2} = 35$ days. The atom emits an Auger electron of 2.82 keV, the only signature for the experiment, and therefore the experiment is not real-time.

The ^{37}Ar atoms from the liquid of perchloroethylene were extracted by bubbling with helium gas, 5 or 6 times a year. The extraction efficiency of the bubbling was

estimated to be more than 90%. Then, ^{37}Ar was condensed and brought to a small proportional counter which provided about 40 to 45% detection efficiency. The measurement of the Auger electron continues for about a year.

Although the energy threshold of the ^{37}Cl reaction is 814 keV, its capture cross section is dominated by transitions to an excited state of 5 MeV. Therefore, the monoenergetic ^7Be neutrinos (0.86 MeV) account only for a small fraction. Neutrinos which can contribute to the capture reaction are pep (0.2 SNU), ^7Be (1.2 SNU), ^8B (6.2 SNU), ^{13}N (0.1 SNU), ^{15}O (0.3 SNU), hep (0.03 SNU) and ^{17}F (0.003 SNU) neutrinos. The total capture rate predicted by the SSM is 8.0 ± 3.0 (3σ) SNU, where the SNU (solar neutrino unit) is 10^{-36} captures per target atom per second.

Their observation has lasted for more than 20 years and the result from the data during the period September 1970 (1970.8) through July 1991 (1991.6) is 0.509 ± 0.031 ^{37}Ar productions per day including background induced by cosmic ray muons. After subtracting the estimated background rate of 0.08 ± 0.03 ^{37}Ar / day, the neutrino capture rate is given by 0.429 ± 0.043 ^{37}Ar /day corresponding to 2.28 ± 0.23 SNU although the expected rate is 8.0 ± 3.0 SNU. This deficit of solar neutrinos is the so-called "Solar Neutrino Problem."

They also indicated a possible time variation of the event rate in anti-correlation with the sunspot numbers. Fig. 1.4 shows the ^{37}Ar production rate superimposed on the inverse of the sunspot numbers. Although the statistical error is large, they claim an anti-correlation. We assumed a linear correlation between them to treat the anti-correlation quantitatively. Then, the correlation function was obtained as (see also section 6.3):

$$R_{\text{Ar}} = (-1.36 \times 10^{-3} \pm 0.51 \times 10^{-3}) \times N_{\text{SS}} + (0.524 \pm 0.055), \quad (\text{eq 1-23})$$

where R_{Ar} is the production rate of ^{37}Ar and N_{SS} the sunspot number. The significance is a 2.7σ effect. Note that the significance level further depends on the treatment of the statistical error [ref 1-16]. Nevertheless, if we take this anti-correlation positively, a new property of the neutrino such as a finite mass and a large magnetic moment must be considered, because the core of the sun where neutrinos are produced is believed to be

stable on the scale of millions of years, much larger than the scale of 10 years (sunspot number has the periodicity of about 11 years). This anti-correlation is the second puzzle of the solar neutrino.

1.3.2. The Kamiokande-II experiment

The Kamiokande-II solar neutrino observation confirmed the deficit of the solar neutrino with a quite different detector technique. Kamiokande is a ring imaging Cherenkov detector filled with 3000 tons of pure water and is located in the Kamioka mine, Kamioka-cho Gifu, Japan. The detector is covered by 1000 meters of rock (Mt. Ikenoyama) which corresponds to 2700 meter water equivalent (m.w.e.). The fiducial volume for the solar neutrino analysis was 680 tons. The fundamental reaction for the solar neutrino observation is an elastic scattering of neutrinos off electrons:



For this reaction it is easy to estimate the interaction rate by the standard electro-weak theory. The advantages of this detection technique are:

- a real-time observation,
- strong directionality of the recoil electron which provides information on the direction of the incoming neutrino, and
- an ability to obtain the energy spectrum of neutrinos via the measurement of the energy spectrum of the recoil electrons.

Due to these features, the Kamiokande experiment has gotten the first evidence that the neutrinos are really coming from the sun.

Kamiokande-II results obtained from 1040 days of data for the period January 1987 through April 1990 (the analysis threshold was 9.3 MeV for first 450 days and 7.5 MeV for last 590 days) was already published [ref 1-7,1-8]:

$$\frac{\text{data}}{\text{"SSM}_{\text{BU88}}} = 0.46 \pm 0.05 \text{ (stat)} \pm 0.06 \text{ (syst)}, \quad (\text{eq 1-25})$$

or

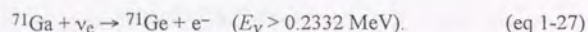
$$\frac{\text{data}}{\text{"SSM}_{\text{BP92}}} = 0.47 \pm 0.05 \text{ (stat)} \pm 0.06 \text{ (syst)}, \quad (\text{eq 1-26})$$

where the expected flux from "SSM_{BU88}" is $5.8 \times 10^6 \text{ cm}^{-2}\text{sec}^{-1}$ [ref 1-26]. There are apparent discrepancies between the observed solar neutrino flux and the SSM predictions.

1.3.3. The SAGE and GALLEX experiments (^{71}Ge experiments)

The most intense neutrinos are from the p-p fusion reaction whose flux is estimated to be $6 \times 10^{10} \text{ cm}^{-2}\text{sec}^{-1}$. This flux is less sensitive to the details of solar model calculations and the ambiguity of the flux is very small. It is useful to observe p-p neutrinos ($E_\nu < 0.42 \text{ MeV}$) for fundamental input into the solar neutrino problem.

Experiments to observe pp-neutrinos must accomplish a low energy threshold and must overcome backgrounds. A radio-chemical experiment using ^{71}Ge can observe p-p neutrinos [ref 1-9,1-11]. ^{71}Ge captures neutrinos via the following reaction [ref 1-27]:



The neutrino capture rate calculated by the "SSM" for individual neutrino sources are pp (70.8 SNU), pep (3.1 SNU), ^7Be (35.8 SNU), ^8B (13.8 SNU), ^{13}N (3.0 SNU), ^{15}O (4.9 SNU), hep (0.06 SNU) and ^{17}F (0.06 SNU), respectively [ref 1-5]. The total capture rate is 131.5^{+21}_{-17} SNU. ^{71}Ge has a half life of 11.4 days and decays back to ^{71}Ga by an electron capture reaction emitting an Auger electron (and X ray) [ref 1-28].

| E.C. mode | De-excitation mode | Energy (keV) |
|--------------------|-----------------------------------|----------------------|
| K electron (88%) | Auger (41.5%) | 10.37 (e) |
| | Auger + K_α (41.2%) | 1.12 (e) + 9.25 (X) |
| | Auger + K_β (5.3%) | 0.11 (e) + 10.26 (X) |
| L electron (10.3%) | Auger (10.3%) | 1.3 (e) |
| M electron (1.7%) | Auger (1.7%) | 0.16 (e) |

There are two ongoing gallium experiments, SAGE [ref 1-29] and GALLEX [ref 1-28]. The SAGE (Baksan Neutrino Laboratory, 4800 m.w.e.) experiment consists of 30 tons (January 1990 to July 1991) / 60 tons (after August 1991) of metallic gallium ($T_m \sim 30^\circ\text{C}$) (natural abundance of ^{71}Ga is 39.89%), and the GALLEX (Gran Sasso, 3300

m.w.e.) experiment uses 30 tons of gallium in an aqueous solution of gallium chloride (GaCl_3) and hydrochloric acid (HCl). The differences between the two experiments are: (1) the mass of target material (60 tons or 30 tons), (2) the form of gallium (metal or solution) and (3) the performance of the proportional counters (SAGE observes only K-capture, while GALLEX can observe K and L-capture).

The advantages of the metal target is less sensitivity to the background reactions produced by radioactive impurities and a smaller volume which reduces some other backgrounds because of its large density, and which provides a larger interaction rate for the calibration experiment (for example, with a ^{51}Cr neutrino source [ref 1-30]). The disadvantage of the metal target is the more complicated procedure for extracting ^{71}Ge from the metal. The schematic flowchart for extracting ^{71}Ge atoms from the target materials are shown in Fig. 1.5.

In any case, both experiments extract ^{71}Ge and finally count the Auger electrons from the decay of ^{71}Ge with a miniaturized proportional counter. The extraction efficiencies of ^{71}Ge are about 75% (SAGE) and 70% to 95% (GALLEX, the value is calibrated for each extraction). The counting efficiencies for Auger electrons are 35% in SAGE, and 65% (shared half and half at K and L-regions) in GALLEX. Background event rates in these experiments are 0.061 counts/day (SAGE, K-region) and 0.02 counts/day (GALLEX, K-region), 0.04 counts/day (GALLEX, L-region) in a best case, while the expected event rate is $1.2 \times \epsilon$ (detection efficiency) $^{71}\text{Ge} \text{ day}^{-1}$ for 30 tons of gallium (which corresponds to about 0.3 counts/day (or 3 counts in total) both for the K and L regions at the beginning of a counting).

The observed event rates in SAGE [ref 1-9,1-10] and GALLEX [ref 1-11,1-12] are:

| R_{Ga} (SNU) | Experiment | Data taking period |
|---|---------------|-------------------------|
| 20^{+15}_{-20} (stat) ± 32 (syst) | SAGE 30 tons | 1990 |
| 85^{+22}_{-32} (stat) ± 20 (syst) | SAGE 60 tons | 1991 |
| 58^{+17}_{-24} (stat) ± 14 (syst) | SAGE combined | 1990, 1991 |
| 82 ± 17 (stat) ± 7 (syst) | GALLEX-I | June '91 to April '92 |
| 97 ± 23 (stat) ± 7 (syst) | GALLEX-II | August '92 to April '93 |

87 ± 14 (stat) ± 7 (syst) GALLEX-I,II combined June '91 to April '93

while the expected rate is 131.5^{+21}_{-17} SNU [ref 1-5].

Their results are both consistent with the SSM prediction or an absence of ^8B and ^7Be neutrinos (and also no pp-neutrinos) within the experimental and theoretical errors.

Time variation of the neutrino flux in correlation with the sun-spot number can not be evaluated from these experiments because the data taking time does not cover a solar minimum period.

1.3.4. Summary of the current solar neutrino experiments

There are being performed three types of solar neutrino observations and they are observing different energy ranges of solar neutrinos:

- ^{71}Ga radio chemical experiments which mainly observe low energy neutrinos, p-p (54%), ^7Be (27%) and ^8B (10%). The flux of p-p neutrinos does not have a large theoretical uncertainty.
- ^{37}Cl radio-chemical experiment which observes middle energy neutrinos, ^7Be (15%) and ^8B (78%).
- Kamiokande real-time counting experiment which observes higher energy neutrinos, ^8B (100%).

The results (data / "SSM_{BP92}") from those experiments are;

| | | | |
|------------------|---|--|-----------|
| ^{71}Ga | : | $0.44^{+0.13}_{-0.18} \pm 0.10$ (SAGE) | (eq 1-28) |
| | : | $0.66 \pm 0.11 \pm 0.05$ (GALLEX) | (eq 1-29) |
| ^{37}Cl | : | 0.285 ± 0.029 | |
| Kamiokande | : | $0.47 \pm 0.05 \pm 0.06$. | |

Furthermore, combining the SAGE and GALLEX results with the assumption that all errors have no correlation each other, the results from ^{71}Ga become 0.59 ± 0.10 . These deficits of the solar neutrino flux are the solar neutrino problem.

Another problem reported by Davis et al. was that the production rate of ^{37}Ar is varying in anti-correlation with the sunspot numbers as described in subsection 6.3.1;

$$R_{\text{Ar}} = (-1.36 \times 10^{-3} \pm 0.51 \times 10^{-3}) \times N_{\text{SS}} + (0.524 \pm 0.055)$$

Such time variation, if it exists, cannot be explained without a neutrino magnetic moment. The significance of the anti-correlation is only 2.7σ and the result from Kamiokande-II seems not to have an anti-correlation. But we should not ignore this interesting result, because some hybrid models [ref 1-31,1-32] can reconcile a large anti-correlation in the ^{37}Cl experiment with a small anti-correlation in the Kamiokande experiment which is consistent with its result within statistical error.

1.3.5. A problem in SSM?

It is also possible to think of SSM modifications [ref 1-33] to explain the solar neutrino problem. Since the p-p neutrino flux should not be greatly changed in order to reproduce the solar luminosity, usual approaches are to invent mechanism to lower the ^8B and/or ^7Be neutrino fluxes. The temperature dependence of individual neutrino fluxes are calculated as [ref 1-33]:

$$\phi(^8\text{B}) \propto \sim T_{\text{core}}^{18}, \quad (\text{eq 1-30})$$

$$\phi(^7\text{Be}) \propto \sim T_{\text{core}}^8, \quad (\text{eq 1-31})$$

$$\phi(\text{pp}) \propto \sim T_{\text{core}}^{-1.2}. \quad (\text{eq 1-32})$$

Taking into account effects (low Z, WIMPs and so on) that lower the temperature of the solar core, the flux of ^8B and ^7Be can be drastically suppressed. It is also known that the different opacity coefficient and capture cross section of $^7\text{Be}+p$, input parameters of SSM calculation, influence the ^8B neutrino flux very much, and the SSM calculation by Turck-Chi  ze et al predicts a much smaller ^8B neutrino flux: $4.4 \pm 1.1(1\sigma) \times 10^6 \text{ cm}^{-2}\text{sec}^{-1}$ [ref 1-4] than the prediction by Bahcall et al.: $5.69 \pm 2.45(3\sigma) \times 10^6 \text{ cm}^{-2}\text{sec}^{-1}$ [ref 1-5].

But experimental observations and the consequences of any approach to modify SSMs cause an inconsistency. The ^8B neutrino flux can be fixed at data/SSM = 0.47 ± 0.08 (or the latest result described in this thesis is $0.514^{+0.043}_{-0.037} \pm 0.061 \rightarrow 0.514 \pm \sim 0.074$) by the Kamiokande result which observes only ^8B neutrinos. SSM modifications cannot change neutrino spectra from each reaction except for their relative

normalization. The flux of p-p (and pep) neutrinos cannot be changed while maintaining the energy generation of the sun. Hence, the event rate in ^{37}Cl experiment which observes ^8B , pep, ^7Be and some other neutrinos, must be larger than their sum:

$$R_{37\text{Cl}} > R(\text{pep}) + R(^8\text{B}_{\text{kam}}) = R(\text{pep}) + (0.514 \pm 0.074) \times R(^8\text{B}_{\text{SSM}}) \\ = 3.39 \pm 0.46 \text{ SNU.} \quad (\text{eq 1-33})$$

The observed rate with the ^{37}Cl experiment is only 2.28 ± 0.23 SNU. The discrepancy (inconsistency) between them is at about the 2σ level. This estimation was made under the non-realistic assumption that the contribution from ^7Be and other neutrinos is zero. Therefore, the practical significance will be larger than the 2σ level. If one takes this discrepancy to be serious, SSM modifications cannot be the answer to the solar neutrino problem. This discrepancy arises in any SSMs calculated by other authors [ref 1-3,1-4] that consider the p-p reaction chain as a main energy source in the sun.

References

- [1-1] R.Davis et al., Phys.Rev.Lett. **20**(1968)1205.
 [1-2] R.Davis Jr., Proceedings of the International Symposium on Neutrino Astrophysics, Takayama/Kamioka, Japan, 1992, p47, edited by Y.Suzuki and K.Nakamura (Universal Academy Press, Inc. Tokyo, Japan 1993).
 [1-3] Berthomieu, Provost and Morel, Astron.Astroph. **268**(1993)775.
 [1-4] Turck-Chièze and Lopes, Astroph.J. **408**(1993)347.
 [1-5] Bahcall and Pinsonneault, Rev.Mod.Phys. **64**(1992)885.
 [1-6] K.S.Hirata et al., Phys.Rev.Lett. **63**(1989)16.
 [1-7] K.S.Hirata et al., Phys.Rev.Lett. **65**(1990)1297.
 [1-8] K.S.Hirata et al., Phys.Rev. **D44**(1991)2241.
 [1-9] A.I.Abazov et al., Phys.Rev.Lett. **24**(1991)3332.
 [1-10] G.T.Zatsepin, Proceedings of the International Symposium on Neutrino Astrophysics, Takayama/Kamioka, Japan, 1992, p71, edited by Y.Suzuki and K.Nakamura (Universal Academy Press, Inc. Tokyo, Japan 1993).
 [1-11] GALLEX collaboration, Phys.Lett. **B285**(1992)376.
 [1-12] F.von Feilitzsch, International Conference "Neutral Current Twenty Years Later", Paris, France, July 6-9, 1993; GALLEX collaboration, preprint GX27a-1993,MPIH-V11a-1993,Chem(BNL)C-3991a(1993),LNGS 93/78, submitted to Phys.Lett. B.

- [1-13] see references in "Neutrino Astrophysics", J.N.Bahcall (Cambridge University Press, 1989).
 [1-14] L.Wolfenstein, Phys.Rev. **D17**(1978)2369, **D20**(1979)2634.
 [1-15] S.P.Mikheyev and A.Yu.Smirnov, Sov.J.Nucl.Phys. **42**(1985)913.
 [1-16] R.Davis Jr., Proceedings of the Seventh Workshop on Grand Unification, ICOBAN '86, Toyama, Japan, 1986, p237, edited by J.Arafune (World Scientific, Singapore, 1987); J.N.Bahcall, G.B.Field and W.H.Press, Astroph.J. **320**(1987)L69; H.J.Haubold and E.Gerth, Solar Physics 127:347, 1990 (Kluwer Academic Publishers, Belgium); B.W.Filippone and P.Vogel, Phys.Lett. **B246**(1990)546.
 [1-17] K.S.Hirata et al., Phys.Rev.Lett. **66**(1991)9.
 [1-18] L.Glashow and L.M.Krauss, Phys.Lett. **B190**(1987)199.
 [1-19] L.B.Okun, M.B.Voloshin and M.I.Vysotsky, Sov.J.Nucl.Phys. **44**(1986)440.
 [1-20] C.S.Lim and W.J.Marciano, Phys.Rev. **D37**(1988)1368.
 [1-21] E.Kh.Akhmedov, Phys.Lett. **B213**(1988)64; Sov.Phys.JETP**68**(1989)690.
 [1-22] H.Minakata and H.Nunokawa, Phys.Rev.Lett. **63**(1989)121; Phys.Rev. **D43**(1991)R297; C.S.Lim, M.Mori, Y.Oyama and A.Suzuki, Phys.Lett. **B243**(1990)389; A.B.Balantekin, P.J.Hatchell and F.Loreti, Phys.Rev. **D41**(1990)3583.
 [1-23] see references in the proceedings of the 121st Colloquium of the International Astronomical Union "Inside the Sun", Versailles, France, 1989 (Kluwer Academic Publishers, 1990); K.G.Libbrecht, M.F.Woodard and J.M.Kaufman, Astroph.J.S. **74**(1990)1129.
 [1-24] M.Kamionkowski and J.N.Bahcall, Astrophysics Preprint Series, IASSNS-AST 93/20, submitted to the Astroph.J.
 [1-25] Y.Suzuki, Proceedings of the International Symposium on Neutrino Astrophysics, Takayama/Kamioka, Japan, 1992, p61, edited by Y.Suzuki and K.Nakamura (Universal Academy Press, Inc. Tokyo, Japan 1993).
 [1-26] J.N.Bahcall and R.K.Ulrich, Rev.Mod.Phys. **60**(1988)297.
 [1-27] V.A.Kuzmin, Sov.Phys. JETP**22**(1966)1051.
 [1-28] R.Wink et al., NIM **A329**(1993)514; O.Cremonesi, talk presented at the XXVIIIth Rencontre de Moriond "Electroweak Interaction and Unified Theories", Les Arcs, Sovie, France, 1993.
 [1-29] V.N.Garvin et al., Proceedings of the 121st Colloquium of the International Astronomical Union "Inside the Sun", p201, Versailles, France, 1989 (Kluwer Academic Publishers, 1990).
 [1-30] M.Cribier et al., NIM **A265**(1988)574.
 [1-31] K.S.Babu, R.N.Mohapatra and I.Z.Rothstein, Phys.Rev. **D44**(1991)2265.
 [1-32] H.Nunokawa, Ph.D. thesis, Tokyo Metro. Univ. (1992).

[1-33] J.N.Bahcall, Neutrino Astrophysics (Cambridge University Press, 1989).

2. Neutrino Mass and Magnetic Moment

The neutrino mass and magnetic moment are two of the most important parameters in neutrino physics. In this section, we discuss the current status of these parameters and the experimental constraints on them.

2.1. Neutrino Mass

The neutrino mass is one of the most fundamental parameters in particle physics. It is the only mass parameter in the Standard Model of particle physics that is not predicted by the theory. The neutrino mass is also one of the most interesting parameters in neutrino physics because it is the only mass parameter that is not predicted by the theory.

The neutrino mass is also one of the most interesting parameters in neutrino physics because it is the only mass parameter that is not predicted by the theory. The neutrino mass is also one of the most interesting parameters in neutrino physics because it is the only mass parameter that is not predicted by the theory.

We do not know the neutrino mass, but we know that it is not zero. The neutrino mass is also one of the most interesting parameters in neutrino physics because it is the only mass parameter that is not predicted by the theory.

The neutrino mass is also one of the most interesting parameters in neutrino physics because it is the only mass parameter that is not predicted by the theory. The neutrino mass is also one of the most interesting parameters in neutrino physics because it is the only mass parameter that is not predicted by the theory.

The neutrino mass is also one of the most interesting parameters in neutrino physics because it is the only mass parameter that is not predicted by the theory. The neutrino mass is also one of the most interesting parameters in neutrino physics because it is the only mass parameter that is not predicted by the theory.

The neutrino mass is also one of the most interesting parameters in neutrino physics because it is the only mass parameter that is not predicted by the theory. The neutrino mass is also one of the most interesting parameters in neutrino physics because it is the only mass parameter that is not predicted by the theory.

2. Neutrino Mass and Magnetic Moment

The experimental status of the direct searches for finite neutrino masses and neutrino magnetic moments are briefly summarized in this chapter.

2.1. Neutrino Mass Limits

Recent LEP e^+e^- collider experiment made a precise study of electro-weak physics on the Z mass (91.187 ± 0.007 GeV) [ref 2-1]. It measured a Z line shape precisely and the number of light neutrinos:

$$N_\nu = 2.98 \pm 0.03 \quad (\text{eq 2-1})$$

(lighter than a half of Z mass), was obtained [ref 2-2]. We already know the ν_e and ν_μ , and ν_τ should exist though there is no direct observation of the ν_τ .

We do not have any experimental evidence of finite neutrino masses, but many models beyond the standard electro-weak theory imply the possibility of a non-zero neutrino mass. The upper limits for the masses have been obtained by several experimental techniques:

(i) ν_e

The decay of tritium, ${}^3\text{H} \rightarrow {}^3\text{He} + e^- + \bar{\nu}_e$, is an adequate reaction to explore the mass of ν_e , because the end point energy of the electron is low at 18.6 keV. The combined limit from all direct measurements is [ref 2-3]:

$$m_{\nu_e} < 7.3 \text{ eV (95\% C.L.)}. \quad (\text{eq 2-2})$$

The double beta decay experiment, $(Z, A) \rightarrow (Z+2, A) + 2e^- + (2\bar{\nu}_e)$ or $(Z, A) \rightarrow (Z-2, A) + 2e^+ + (2\nu_e)$, can study the ν_e mass indirectly. Assuming Majorana neutrinos, the transition amplitude of neutrino-less double beta decay can be translated to a neutrino mass (if mixing exists, the mass means a quantity $\langle m_{\nu_e} \rangle = \left| \sum_j V_{ej}^2 m_{\nu_j} \right|$, where the matrix V connects mass eigen-states ν_i ($i = 1$ to 3)

and flavor eigen-states ν_α ($\alpha = e, \mu, \tau$) by $|\nu_\alpha\rangle = \sum_i V_{\alpha i} |\nu_i\rangle$. The lack of evidence for neutrino-less double beta decay from the reaction $^{76}\text{Ge} \rightarrow ^{76}\text{Se} + 2e^-$ was used to place an upper limit on the ν_e mass [ref 2-4]:

$$\langle m_{\nu_e} \rangle < 1.2 \text{ eV (90\% C.L.)} \quad (\text{eq 2-3})$$

(ii) ν_μ

The mass limit for ν_μ is derived from the precise measurement of the momentum distributions from $\pi \rightarrow \mu\nu_\mu$ decay [ref 2-5]:

$$m_{\nu_\mu} < 250 \text{ keV (90\% C.L.)} \quad (\text{eq 2-4})$$

(iii) ν_τ

The mass limit of ν_τ is obtained from the analysis of the invariant mass of 5 pions in the τ decay mode of $\tau^- \rightarrow \nu_\tau \pi^- \pi^- \pi^+ \pi^+$ [ref 2-6]:

$$m_{\nu_\tau} < 35 \text{ MeV (95\% C.L.)} \quad (\text{eq 2-5})$$

2.2. Limits on Magnetic Moment

If neutrinos have a magnetic moment, the cross section for elastic ν -e scattering via a photon exchange is given by the formula [ref 2-7]:

$$\sigma(E_\nu, E_e > E_{th}) = \frac{\mu_\nu}{\mu_B} \pi r_0^2 \left[\frac{E_{th}}{E_\nu} - \log\left(\frac{E_{th}}{E_\nu}\right) - 1 \right] \quad (\text{eq 2-6})$$

where

E_ν is the incident neutrino energy,

E_e the recoil electron energy,

E_{th} the threshold energy,

μ_ν the magnetic moment of the neutrino,

$\mu_B = e/2m_e = 5.788 \times 10^{-15} \text{ MeV/Gauss}$ is the Bohr magneton,

$r_0 = e^2/m_e$ the classical electron radius, and

m_e the mass of electron.

A scattering amplitude consistent with zero magnetic moment resulted in the upper limits:

$$\mu_{\nu_e} < 4 \times 10^{-10} \mu_B \quad (90\% \text{ C.L.}) \quad [\text{ref 2-7,2-8}], \quad (\text{eq 2-7})$$

$$\mu_{\bar{\nu}_e} < 10.8 \times 10^{-10} \mu_B \quad (90\% \text{ C.L.}) \quad [\text{ref 2-9}], \quad (\text{eq 2-8})$$

$$\mu_{\nu_\mu} < 7.4 \times 10^{-10} \mu_B \quad (90\% \text{ C.L.}) \quad [\text{ref 2-10}], \quad (\text{eq 2-9})$$

These constraints do not contradict to the requirement of the hybrid model for $\sim 10^{-11} \mu_B$ in order to explain the time variation of the ^{37}Cl experiment.

The upper bound on μ_ν from cosmology and astrophysics is much more restrictive.

(i) If neutrinos have a large magnetic moment, the right-handed neutrinos can be produced through the magnetic interaction and they contribute to the energy density of neutrinos which increase the expansion rate in the early universe. This leads to a larger ^4He abundance than observed. Hence, the upper limit:

$$\mu_\nu < (0.1-0.2) \times 10^{-10} \mu_B, \quad (\text{eq 2-10})$$

is obtained in [ref 2-11].

(ii) Sterile right-handed neutrinos take energy away from a star effectively. Therefore, a large magnetic moment shorten the life of stars. This effect enlarges the difference of the stellar luminosity before and after a helium flash. This argument contradicts the difference of the luminosity which is obtained from red giant observations, and the magnetic moment is limited to [ref 2-12]:

$$\mu_\nu < 3 \times 10^{-12} \mu_B. \quad (\text{eq 2-11})$$

Note that this scenario is not true for the Majorana neutrino because a right-handed helicity means an anti-neutrino which is not sterile.

(iii) The bound from the observation of SN1987A gives the most severe limit. Helicity flipped neutrinos during the creation of a neutron star rapidly and efficiently bring out energy and, as a consequence, the time scale of $\bar{\nu}$ emission and the total

energy emitted in $\bar{\nu}$'s would both have been much less than what was observed from SN1987A. One obtains the upper bound [ref 2-13] of:

$$\mu_{\nu} < 7.4 \times 10^{-13} \mu_B, \quad (\text{eq 2-12})$$

but this limit is debatable [ref 2-14] and the limit also do not apply to Majorana neutrinos.

References

- [2-1] The LEP Collaborations: ALEPH, DELPHI, L3 and OPAL, Phys.Lett. **B276**(1992)247.
- [2-2] C.Declercq, talk presented at the XXVIIIth Rencontre de Moriond "Electroweak Interaction and Unified Theories", Les Arcs, Savoy, France, 1993.
- [2-3] K.Hikasa et al., Phys.Rev. **D45**(1992)S1.
- [2-4] A.Balysh et al., Proceedings of the XXVIIth Rencontre de Moriond "Progress in Atomic Physics Neutrinos and Gravitation", p177, Les Arcs, Savoie, France, 1992, edited by G.Chardin, O.Fackler and J.Tran Thanh Van (Editions Frontiers, 1992).
- [2-5] R.Abelo et al., Phys.Lett. **B146**(1984)431.
- [2-6] H.Albrecht et al., Phys.Lett. **B202**(1988)149.
- [2-7] A.V.Kyuldjiev, Nucl.Phys. **B243**(1984)387.
- [2-8] F.Reines, H.Gurr and H.Sobel, Phys.Rev.Lett. **37**(1976)315; P.Vogel and J.Engel, Phys.Rev. **D39**(1989)3378.
- [2-9] L.A.Ahrens et al., Phys.Rev. **D41**(1990)3301.
- [2-10] D.A.Krakauer et al., Phys.Lett. **B252**(1990)177.
- [2-11] J.A.Morgan, Phys.Lett. **B102**(1981)247.
- [2-12] G.G.Raffelt, Phys.Rev.Lett. **64**(1990)2856.
- [2-13] S.Nussinov and Y.Rephaeli, Phys.Rev. **D36**(1987)2278; I.Goldman, Y.Aharonov, G.Alexander and S.Nussinov, Phys.Rev.Lett. **60**(1988)1789; J.M.Lattimer and J.Cooperstein, Phys.Rev.Lett. **61**(1988)23; R.Barbieri and R.N.Mohapatra, Phys.Rev.Lett. **61**(1988)27; D.Notzold, Phys.Rev. **D38**(1988)1658.
- [2-14] M.B.Voloshin, Phys.Lett. **B209**(1988)360.

3. Neutrino Oscillation and Resonant Spin Flavor Precession

3.1. Neutrino Oscillation in Vacuum

The three known neutrinos paired with their charged partners are classified into three generations:

$$\begin{pmatrix} \nu_e \\ e^- \end{pmatrix}, \begin{pmatrix} \nu_\mu \\ \mu^- \end{pmatrix} \text{ and } \begin{pmatrix} \nu_\tau \\ \tau^- \end{pmatrix},$$

which are weak eigenstates. These weak eigenstates may differ from the mass eigenstates and may mix with each other, as quarks do. If we denote weak eigenstates as $|\nu_\alpha\rangle$ ($\alpha = e, \mu, \tau$) and mass eigenstates as $|\nu_i\rangle$ ($i = 1$ to 3), we can connect these states through the matrix V like the Kobayashi-Masukawa matrix in the quark sector:

$$|\nu_\alpha\rangle = \sum V_{\alpha i} |\nu_i\rangle. \quad (\text{eq 3-1})$$

In order to simplify the problem, we will assume only two flavors. Then the above expression can be written by

$$\begin{pmatrix} \nu_e \\ \nu_\mu \end{pmatrix} = \begin{pmatrix} \cos\theta & \sin\theta \\ -\sin\theta & \cos\theta \end{pmatrix} \begin{pmatrix} \nu_1 \\ \nu_2 \end{pmatrix}. \quad (\text{eq 3-2})$$

The propagation of the mass eigenstates of neutrinos $|\nu_i\rangle$ in time is determined by the formula $|\nu_i\rangle_t = e^{-iE_i t} |\nu_i\rangle_0$. Assuming that $|\nu_e\rangle$ was created at $t = 0$, then the initial neutrino state,

$$|\nu\rangle_0 = |\nu_e\rangle = \cos\theta |\nu_1\rangle_0 + \sin\theta |\nu_2\rangle_0 \quad (\text{eq 3-3})$$

evolves to

$$|\nu\rangle_t = \cos\theta e^{-iE_1 t} |\nu_1\rangle_0 + \sin\theta e^{-iE_2 t} |\nu_2\rangle_0. \quad (\text{eq 3-4})$$

It can be expressed by using flavor eigenstates,

$$|\nu\rangle_t = (\cos^2\theta e^{-iE_1 t} + \sin^2\theta e^{-iE_2 t}) |\nu_e\rangle + \cos\theta \sin\theta (e^{-iE_1 t} - e^{-iE_2 t}) |\nu_\mu\rangle. \quad (\text{eq 3-5})$$

Chapter 3. Neutrino Oscillation and Resonant Spin Flavor Precession

This means that neutrinos may oscillate into one another, if they have different masses,

$$m_1 \neq m_2 \quad (E_1 \neq E_2), \quad (\text{eq 3-6})$$

(of course it means non-zero neutrino mass) and non-zero mixing,

$$\theta \neq 0. \quad (\text{eq 3-7})$$

Most of the grand-unified theories require such finite mass and mixing of neutrinos. In the solar neutrino case, the neutrino energy is much greater than its mass, $E \gg m$, and the energy can be approximated by:

$$E_i \approx p + \frac{m_i^2}{2p} \approx E + \frac{m_i^2}{2E}. \quad (\text{eq 3-8})$$

Then the probabilities that a neutrino which, being born as a $|\nu_e\rangle$, remains a $|\nu_e\rangle$ or becomes $|\nu_\mu\rangle$ after a travel of the distance L are,

$$P(\nu_e \rightarrow \nu_e(t)) = 1 - \sin^2 2\theta \sin^2 \frac{\Delta}{2}, \quad (\text{eq 3-9})$$

$$P(\nu_e \rightarrow \nu_\mu(t)) = \sin^2 2\theta \sin^2 \frac{\Delta}{2}, \quad (\text{eq 3-10})$$

respectively, where,

$$\Delta = \frac{(m_2^2 - m_1^2)L}{2E} = \frac{\delta m^2 L}{2E}. \quad (\text{eq 3-11})$$

Search for such neutrino oscillations has been vigorously conducted by using neutrinos produced at accelerators and nuclear reactors. The parameter regions ($\sin^2 2\theta, \delta m^2$) where those experiments can explore are limited by the neutrino energy E , the distance L to the neutrino source and the statistics of the experiment. The parameter E/L , which controls the phase of the transition probability, determines an explorable region of δm^2 , and the statistics of an experiment, N , which limit the measurable precision of the transition probability P to the order of $O(1/\sqrt{N})$, determine an explorable region of $\sin^2 2\theta$. Simply speaking, an experiment is most sensitive to neutrino oscillations in the parameter region of $\delta m^2 \sim \frac{2\pi E}{L}$ ($\Delta \sim \pi$). In the parameter region of $\delta m^2 \gg \frac{2\pi E}{L}$, neutrinos experience too many oscillation cycles and only the averaged probabilities,

Chapter 3. Neutrino Oscillation and Resonant Spin Flavor Precession

$$P(\nu_e \rightarrow \nu_e) = 1 - \frac{1}{2} \sin^2 2\theta, \quad (\text{eq 3-12})$$

$$P(\nu_e \rightarrow \nu_\mu) = \frac{1}{2} \sin^2 2\theta, \quad (\text{eq 3-13})$$

are measurable. These probabilities are actually obtained by averaging the equations (eq 3-9,10) over time ($t = L$).

Accelerator experiments use $\nu_\mu(\nu_e)$ produced by decays from π^\pm, K^\pm . The neutrino beam energy can be controlled from several hundred of MeV to a few tens of GeV. If neutrino oscillation such as $\nu_\mu \rightarrow \nu_e$ occurs, the new flavor of neutrino can produce its charged lepton partner through the interaction $\nu_e + X \rightarrow e^- + X'$. This is an "Appearance" experiment. One, therefore, can explore a wide parameter region of $\sin^2 2\theta$ down to about 10^{-3} with high statistics experiments (now limited by systematic error). But it is hard to have a large distance between the accelerator and the detector, and searches for neutrino oscillations have been performed down to 0.1 eV² [ref 3-1]. However, long base line neutrino oscillation experiments are now proposed [ref 3-2] and then the parameter region for δm^2 can be tested down to 10^{-3} eV².

Reactor experiments use $\bar{\nu}_e$ with an average energy around 3 MeV emitted from beta-decay nuclei of fission products. These low energy neutrinos cannot produce μ or τ particles and only a "Disappearance" experiment (search for a deficit in the $\bar{\nu}_e$ interaction rate) is possible. Since the neutrino energy is low, one performs a search for neutrino oscillations in the region $\delta m^2 \geq 0.01$ eV² [ref 3-3]. Supposing a reactor with a power of $P(\text{MW})$, the neutrino flux at distance $L(\text{m})$ becomes [ref 3-4]:

$$\phi_{\bar{\nu}_e} \sim 1.5 \times 10^{12} \text{cm}^{-2} \text{sec}^{-1} \frac{P(\text{MW})}{L^2(\text{m}^2)}. \quad (\text{eq 3-14})$$

Low statistics (P is several hundreds) limited the explored region to $\sin^2 2\theta \geq 0.1$ [ref 3-3].

Atmospheric neutrinos are also a useful neutrino source. π and K made by collisions of primary cosmic rays in the atmosphere decay into charged leptons and neutrinos. The neutrinos have energies from several tens of MeV to several tens of GeV and travel thousands to ten millions of meters before reaching a detector. Therefore, the experiment can explore the region of $\delta m^2 > 10^{-5}$ eV² [ref 3-5,3-6].

Chapter 3. Neutrino Oscillation and Resonant Spin Flavor Precession

Solar neutrinos have energies less than 18 MeV and travel long distances of about 1.5×10^{11} m. Solar neutrino experiments are, therefore, sensitive down to very small value of $\delta m^2 > 10^{-12}$ eV².

There is a possible solution of the solar neutrino problem in the framework of vacuum neutrino oscillations. Supposing that oscillation parameters were $\delta m^2 \sim 10^{-10}$ eV² (oscillation length is a few times smaller than the revolution radius of the earth) and $\sin^2 2\theta \sim O(1)$ (large mixing angle), vacuum neutrino oscillation would greatly enhance the neutrino deficit. The solar neutrino spectrum at the earth, for the parameters of $\delta m^2 = 8 \times 10^{-11}$ eV² and $\sin^2 2\theta = 1$, is shown in Fig. 3.1. Such neutrino oscillations with fine tuned parameters are called as "just-so" oscillations [ref 1-18]. It can be verified by a check of the seasonal variation of the neutrino flux whether the just-so oscillation takes place or not, because the earth revolves around the sun and the radius varies by about 5×10^9 m which is comparable to the oscillation length of the "just-so" neutrino oscillation. The ⁷Be neutrino, which has a monochromatic energy spectrum, would be the best neutrino source for this purpose [ref 3-7]. Next generation high statistics experiments such as Super-Kamiokande will also be able to identify the just-so oscillation [ref 3-8] by the precise measurement of a seasonal variation ($\sim \pm 1\%$) of the ⁸B neutrino flux.

3.2. Neutrino Oscillation in Matter (MSW)

Solar neutrinos traverse dense matter in the sun and in the earth, hence neutrino oscillation may be enhanced by the matter effect [ref 1-15]. The parameter regions where we can explore with various neutrino sources (reactor, accelerator, atmospheric and solar neutrinos) are drawn in Fig. 3.2. It tells us that solar neutrino is a useful source to search a very wide parameter region.

Wolfenstein first pointed out [ref 1-14] that the mass of ν_e increases in matter through the forward scattering amplitude of the charged current interaction. Mikheyev and Smirnov extended the theory in matter, changing its density (sun) [ref 1-15], and found a resonance behavior of the model which may explain the solar neutrino problem. This resonant oscillation in matter is called as MSW effect.

Chapter 3. Neutrino Oscillation and Resonant Spin Flavor Precession

In order to consider the propagation of neutrinos in matter, all interactions which give a forward scattering amplitude to an identical final state must be taken into account. This forward scattering works as an effective potential in matter. Target particles to be considered in solar neutrino propagation are electrons, protons and neutrons.

Effective potential from neutrino-electron scattering:

Neutral current interaction is common for any kind of neutrino. But ν_e and $\bar{\nu}_e$ can, additionally, have charged current interactions with electrons as shown in Fig. 3.3. The amplitudes of the scattering for ν_e are [ref 3-9],

neutral current :

$$H_{nc} = \frac{g_L}{\cos\theta_W}(\text{vertex}) \times \frac{1}{2m_Z^2}(\text{propagator}) \times \frac{g_L}{\cos\theta_W} \left(-\frac{1}{2} + 2\sin^2\theta_W\right)(\text{vertex})$$

$$= \frac{g_L^2}{2m_W^2} \left(-\frac{1}{2} + 2\sin^2\theta_W\right), \quad (\text{eq 3-15})$$

charged current :

$$H_{cc} = \frac{g_L}{\sqrt{2}}(\text{vertex}) \times \frac{1}{m_W^2}(\text{propagator}) \times \frac{g_L}{\sqrt{2}}(\text{vertex}) = \frac{g_L^2}{2m_W^2}, \quad (\text{eq 3-16})$$

respectively. g_L is a weak coupling constant, θ_W the Weinberg angle, m_Z the mass of the Z-boson and,

$$m_W = m_Z \cos\theta_W \quad (\text{eq 3-17})$$

the mass of the W-boson. Therefore, the effective potentials for $\nu_e + e^- \rightarrow \nu_e + e^-$ and $\nu_\mu + e^- \rightarrow \nu_\mu + e^-$ are,

$$H(\nu_e e^- \rightarrow \nu_e e^-: \text{NC+CC}) = \frac{1}{2}\sqrt{2}G(1 + 4\sin^2\theta_W), \quad (\text{eq 3-18})$$

$$H(\nu_\mu e^- \rightarrow \nu_\mu e^-: \text{NC only}) = \frac{1}{2}\sqrt{2}G(-1 + 4\sin^2\theta_W), \quad (\text{eq 3-19})$$

where $\frac{G}{\sqrt{2}} = \frac{g_L^2}{8m_W^2}$, and a factor $\frac{1}{2}$ is for a spin average.

Effective potential from neutrino-proton and neutrino-neutron interaction:

Only the neutral current interaction can take place for proton and neutron targets. The effective potential of the interaction on protons is same for ν_e and ν_μ and it is [ref 3-9],

Chapter 3. Neutrino Oscillation and Resonant Spin Flavor Precession

$$H(\nu_p \rightarrow \nu_p) = \frac{G}{\sqrt{2}}(1 - 4\sin^2\theta_W), \quad (\text{eq 3-20})$$

That from neutron is [ref 3-9],

$$H(\nu_n \rightarrow \nu_n) = -\frac{G}{\sqrt{2}}. \quad (\text{eq 3-21})$$

By the way, the different speed of the phase rotation of the neutrino wave function causes the neutrino oscillation, and an important factor in the diagonal elements of the propagation matrix is the only difference (this means the same contribution to the diagonal elements can be neglected in the neutrino oscillation calculation).

In the case of the MSW calculation we consider neutrinos but not anti-neutrinos, and every effective potential of the neutral current is the same for ν_e and ν_μ . Therefore, we need to consider only charged current interactions of $\nu_e e$. Hence, we obtain the diagonal element of the Hamiltonian (neutrino propagation matrix) in matter as,

$$H_M^{\nu_e} = \{H(\nu_e e^- \rightarrow \nu_e e^-) - H(\nu_\mu e^- \rightarrow \nu_\mu e^-)\} N_e = \sqrt{2}GN_e, \quad (\text{eq 3-22})$$

$$H_M^{\nu_\mu} = 0, \quad (\text{eq 3-23})$$

where N_e is the number density of electrons in matter.

The neutrino propagation equation in matter can be easily treated in the expression of flavor eigen-state, since the interaction with matter can be included in a simple way. To do this, it is convenient to begin with a propagation equation in vacuum. The neutrino wave function at time t can be written as,

$$|\nu\rangle_t = \begin{pmatrix} \cos\theta & \sin\theta \\ -\sin\theta & \cos\theta \end{pmatrix} \begin{pmatrix} e^{-iE_1 t} & 0 \\ 0 & e^{-iE_2 t} \end{pmatrix} \begin{pmatrix} \cos\theta & -\sin\theta \\ \sin\theta & \cos\theta \end{pmatrix} \begin{pmatrix} a\nu_e \\ b\nu_\mu \end{pmatrix}, \quad (\text{eq 3-24})$$

where a^2 is the probability that a neutrino is ν_e at $t = 0$, and b^2 the probability that a neutrino is ν_μ at $t = 0$, and $a^2 + b^2 = 1$.

Then, differentiating (eq 3-24), we get,

$$i \frac{d}{dt} |\nu\rangle_t = \left(E + \frac{\cos^2\theta m_1^2 + \sin^2\theta m_2^2}{2E} \right) \begin{pmatrix} 1 & 0 \\ 0 & 1 \end{pmatrix} |\nu\rangle_t + \begin{pmatrix} 0 & \frac{\delta m^2}{4E} \sin 2\theta \\ \frac{\delta m^2}{4E} \sin 2\theta & \frac{\delta m^2}{2E} \cos 2\theta \end{pmatrix} |\nu\rangle_t, \quad (\text{eq 3-25})$$

Chapter 3. Neutrino Oscillation and Resonant Spin Flavor Precession

where $\delta m^2 = m_2^2 - m_1^2$, and we have used the approximation $E_i \approx E + \frac{m_i^2}{2E}$ in the calculation. Comparing the equation (eq 3-25) with the formula, $i \frac{d}{dt} |\nu\rangle_t = H |\nu\rangle_t$ (propagation equation), we can get the Hamiltonian in vacuum as,

$$H_V = \begin{pmatrix} 0 & \frac{\delta m^2}{4E} \sin 2\theta \\ \frac{\delta m^2}{4E} \sin 2\theta & \frac{\delta m^2}{2E} \cos 2\theta \end{pmatrix}. \quad (\text{eq 3-26})$$

The first term in the equation (eq 3-25) is neglected because it does not contribute to neutrino oscillation. Then, adding the effective potential for the neutrino propagation in matter,

$$H_M = \begin{pmatrix} \sqrt{2}GN_e & 0 \\ 0 & 0 \end{pmatrix}, \quad (\text{eq 3-27})$$

which is obtained in (eq 3-22,23), and the vacuum propagation matrix (eq 3-26), we obtain the Hamiltonian in matter as,

$$H = H_V + H_M = \begin{pmatrix} \sqrt{2}GN_e & \frac{\delta m^2}{4E} \sin 2\theta \\ \frac{\delta m^2}{4E} \sin 2\theta & \frac{\delta m^2}{2E} \cos 2\theta \end{pmatrix} \quad (\text{eq 3-28})$$

$$= \frac{a_e + \Delta \cos 2\theta}{2} \begin{pmatrix} 1 & 0 \\ 0 & 1 \end{pmatrix} + \begin{pmatrix} \frac{a_e - \Delta \cos 2\theta}{2} & \frac{\Delta \sin 2\theta}{2} \\ \frac{\Delta \sin 2\theta}{2} & -\frac{a_e - \Delta \cos 2\theta}{2} \end{pmatrix},$$

where $a_e = \sqrt{2}GN_e$ and $\Delta = \frac{\delta m^2}{2E}$. The eigen-values of propagation in matter then becomes

$$\begin{pmatrix} \frac{(a_e - \Delta \cos 2\theta) \cos 2\phi - \Delta \sin 2\theta \sin 2\phi}{2} & 0 \\ 0 & -\frac{(a_e - \Delta \cos 2\theta) \cos 2\phi - \Delta \sin 2\theta \sin 2\phi}{2} \end{pmatrix} \quad (\text{eq 3-29})$$

and the eigen-vector of neutrinos in matter is;

$$\begin{pmatrix} \nu_{1m} \\ \nu_{2m} \end{pmatrix} = \begin{pmatrix} \cos\phi & -\sin\phi \\ \sin\phi & \cos\phi \end{pmatrix} \begin{pmatrix} \nu_e \\ \nu_\mu \end{pmatrix}. \quad (\text{eq 3-30})$$

Where ϕ is the effective mixing angle in matter, which is expressed by

Chapter 3. Neutrino Oscillation and Resonant Spin Flavor Precession

$$\tan 2\phi = \frac{\Delta \sin 2\theta}{\Delta \cos 2\theta - a_e} = \frac{\tan 2\theta}{1 - \frac{2\sqrt{2}GN_e E}{\delta m^2 \cos 2\theta}} \quad (\text{eq 3-31})$$

This equation means that the effective mixing angle in matter, ϕ , can become maximal even if the mixing in vacuum, θ , is very small (but not zero). Such a resonant condition is

$$\delta m^2 \cos 2\theta = 2\sqrt{2}GN_e E. \quad (\text{eq 3-32})$$

Solar neutrinos are produced in a high density region (the core of the sun) and escape from the surface where the density is low. We can qualitatively trace the change of the parameters N_e , ϕ and ν_{2m} for the case of solar neutrinos assuming $\delta m^2 > 0$, $\theta < \frac{\pi}{4}$ and $\theta \neq 0$.

$$\begin{aligned} N_e : \infty &\rightarrow N_e = \frac{\delta m^2 \cos 2\theta}{2\sqrt{2}GE} \rightarrow 0 \\ \phi : \frac{\pi}{2} &\rightarrow \frac{\pi}{4} \rightarrow \theta \\ |\nu_{2m}\rangle : |\nu_e\rangle &\rightarrow \frac{1}{\sqrt{2}}(|\nu_e\rangle + |\nu_\mu\rangle) \rightarrow \sin\theta |\nu_e\rangle + \cos\theta |\nu_\mu\rangle \end{aligned}$$

Therefore, the probability of the neutrino (which was born as ν_e) to become ν_μ is $\cos^2\theta$. If the mixing is small ($\theta \sim 0$), all of ν_e convert into ν_μ .

Neutrinos with energy E_ν greater than the critical energy E_{crit} ,

$$E_\nu \geq E_{\text{crit}} = \frac{\delta m^2 \cos 2\theta}{2\sqrt{2}GN_e^{\text{max}}}, \quad (\text{eq 3-33})$$

can satisfy the resonance condition (eq 3-32) in the sun, where N_e^{max} is the maximum density of electrons along the track of the neutrino.

Therefore, the neutrino spectrum is suppressed in the high energy region ($>E_{\text{crit}}$). This scheme (adiabatic process) takes place when the density of electrons in the resonance region varies slowly enough.

In the case that the density of electrons in the resonance region varies rapidly (non-adiabatic case), a jump transition from ν_{2m} to ν_{1m} arises. The probability of the jump transition is obtained with an approximation developed by Landau and Zener (LZ-approximation) [ref 3-10]. The approximation is exact when the density of electrons

Chapter 3. Neutrino Oscillation and Resonant Spin Flavor Precession

depends linearly upon the length traveled by the neutrino. The jumping probability is given by [ref 3-11]

$$P_{\text{jump}} = \exp\left[\frac{-\pi \delta m^2 \sin^2 2\theta}{4E \cos 2\theta} \left(\frac{N_e}{|N_e|_{\text{res}}}\right)\right], \quad (\text{eq 3-34})$$

with the LZ-approximation. Therefore, the condition;

$$\frac{\delta m^2}{E} \times \sin^2 2\theta \geq \left(\frac{|N_e|}{N_e}\right)_{\text{res}} \times \cos 2\theta \quad (\text{eq 3-35})$$

is required to not change from ν_{2m} to ν_{1m} (to convert from ν_e to ν_μ). This condition is easier for low energy neutrinos than high energy ones. Hence, the neutrino spectrum in the higher energy region is no longer suppressed effectively.

The parameter region in Fig. 3.2 shows a drastic deficit of solar neutrinos due to this MSW effect. The regions denoted by H, O and V are called the adiabatic, non-adiabatic and quasi-vacuum regions, respectively, and every region has its own characteristic effect on the energy spectrum of the solar neutrinos. In the region H, the high energy region of the energy spectrum is suppressed as seen in (eq 3-33). In the region O, high energy neutrinos can remain the same flavor as at their birth as seen in the condition (eq 3-35). In the region V, the neutrinos keep the shape of their energy spectrum the same as their original one, but are converted into another flavor with a same fraction in all energy regions.

It is also pointed out that regeneration ($\nu_e \rightarrow \nu_\mu \rightarrow \nu_e$) can occur along the neutrino path (sun \rightarrow vacuum \rightarrow earth) due to the earth effect [ref 3-12]. This regeneration causes a larger neutrino flux at night time (neutrinos go through the earth) than that at day time (neutrinos do not penetrate the earth). Separate measurements of the neutrino flux at day time and at night time can identify this regeneration effect. Of course, such measurements should be real-time, which only Kamiokande can perform now [ref 1-17]. Fig. 3.4 shows the 90% C.L. exclusion region obtained by the study of day/night variation in Kamiokande. It is generally known that the MSW effect cannot cause time variation of the neutrino flux except for day/night variation.

Chapter 3. Neutrino Oscillation and Resonant Spin Flavor Precession

As a special case, it is pointed out [ref 3-13] that the density fluctuation in the sun might affect neutrino oscillations and the change in the density, perhaps correlated to solar activity on the surface, may cause anti-correlation between the neutrino flux and sunspot numbers.

3.3. Resonant Spin Flavor Precession (RSFP)

The eleven year periodicity of the solar neutrino flux suggested by the ^{37}Cl experiment requires other explanation than the MSW effect. The interaction between a neutrino magnetic moment and a magnetic field in the sun can convert the neutrino helicity from left-handed to right-handed, and right-handed neutrinos are sterile to the ^{37}Cl neutrino capture reaction. Therefore, the 22 year periodicity of the change of the magnetic field may be the cause of such time variation. This scheme was first pointed out by Cisneros [ref 3-14]. Voloshin, Vysotskii and Okun [ref 1-19] first adopted the scheme for the solar neutrino problem. Following them, Lim, Marciano [ref 1-20] and Akhmedov [ref 1-21] found that a magnetic moment of the neutrino can cause the resonant transition of neutrino helicity like the MSW effect in the sun. This effect is called Resonant Spin Flavor Precession (RSFP).

When we consider the magnetic transition of neutrinos, right handed neutrinos play an important role. We cannot neglect the neutrino interactions with protons and neutrons in matter, because the amplitude of the forward scattering for right-handed neutrinos is different from that of left-handed neutrinos. Then the effective potentials for neutrinos in matter are now

$$\begin{aligned} H_M^{\nu e} &= H(\nu_e e \rightarrow \nu_e e)N_e + H(\nu_p \rightarrow \nu_p)N_p + H(\nu_n \rightarrow \nu_n)N_n \\ &= \frac{G}{\sqrt{2}}(1 + 4\sin^2\theta_W)N_e + \frac{G}{\sqrt{2}}(1 - 4\sin^2\theta_W)N_p - \frac{G}{\sqrt{2}}N_n \\ &= \frac{G}{\sqrt{2}}(2N_e - N_n), \end{aligned} \quad (\text{eq 3-36})$$

and

$$H_M^{\nu \mu} = -\frac{G}{\sqrt{2}}N_n, \quad (\text{eq 3-37})$$

Chapter 3. Neutrino Oscillation and Resonant Spin Flavor Precession

where N_p and N_n are the number densities of protons and neutrons, and the relation

$$N_e = N_p \quad (\text{eq 3-38})$$

in matter has already been considered.

Right-handed neutrinos are sterile in the Dirac neutrino case, and the effective potential does not arise. In the Majorana neutrino case, right-handed neutrinos are anti-neutrinos, hence they interact with matter. The effective potentials for $\bar{\nu}_e$ and $\bar{\nu}_\mu$ are [ref 3-9]

$$H_M^{\bar{\nu}_e} = -\frac{G}{\sqrt{2}}(2N_e - N_n) \quad (\text{eq 3-39})$$

$$H_M^{\bar{\nu}_\mu} = \frac{G}{\sqrt{2}}N_n. \quad (\text{eq 3-40})$$

Then the propagation equation of Dirac neutrinos with a (transition) magnetic moment can be written as

$$i\frac{d}{dt}\begin{pmatrix} \nu_{eL} \\ \nu_{\mu R} \end{pmatrix} = \begin{pmatrix} \frac{G}{\sqrt{2}}(2N_e - N_n) & \mu B \\ \mu B & a \end{pmatrix} \begin{pmatrix} \nu_{eL} \\ \nu_{\mu R} \end{pmatrix}. \quad (\text{eq 3-41})$$

There are two cases for the right handed neutrinos ν_R . In the case of $\nu_R = \nu_{eR}$, $\mu = \mu_{ee}$ is the magnetic moment, and $a = 0$. In the case of $\nu_R = \nu_{\mu R}$, $\mu = \mu_{e\mu}$ is the transition magnetic moment, and $a = \frac{\delta m^2}{2E}$.

In the Majorana neutrino case, CPT invariance requires [ref 3-9]

$$\mu_{\alpha\beta} = -\mu_{\beta\alpha} \quad (\alpha, \beta = e, \mu). \quad (\text{eq 3-42})$$

Therefore, only the transition magnetic moment is allowed ($\mu_{ee} = \mu_{\mu\mu} = 0$) and we must consider (eq 3-40), because the right-handed neutrino $\bar{\nu}_\mu$ is not sterile. The propagation equation is expressed as

$$i\frac{d}{dt}\begin{pmatrix} \nu_{eL} \\ \bar{\nu}_\mu \end{pmatrix} = \begin{pmatrix} \frac{G}{\sqrt{2}}(2N_e - N_n) & \mu B \\ \mu B & \frac{G}{\sqrt{2}}N_n + \frac{\delta m^2}{2E} \end{pmatrix} \begin{pmatrix} \nu_{eL} \\ \bar{\nu}_\mu \end{pmatrix}. \quad (\text{eq 3-43})$$

One finds that these RSFP models can explain the time variation with a very large magnetic moment such as $10^{-10}\mu_B$. Such large magnetic moment seems not to agree with the experimental limits (see section 2.2).

3.4. Hybrid Model (RSFP+MSW)

The difficulty of the RSFP model, which requires a very large magnetic moment, is overcome by a so-called hybrid model which is a powerful model extended from the RSFP by including the MSW effect simultaneously, and the required (transition) magnetic moment becomes about $10^{-11} \mu_B$. Now many physicists [ref 1-31,1-32] are trying to explain not only the time variation in the ^{37}Cl experiment but also the lack of a significant time variation of the Kamiokande result in the framework of the hybrid model.

In order to include the MSW effect, we must consider the mixing (eq 3-26) and effective potentials for ν_μ (eq 3-37) and for $\bar{\nu}_e$ (eq 3-39). Then the propagation equation of a Dirac neutrino under the hybrid model is expressed as

$$i \frac{d}{dt} \begin{pmatrix} \nu_{eL} \\ \nu_{\mu L} \\ \nu_{eR} \\ \nu_{\mu R} \end{pmatrix} = \begin{pmatrix} \frac{G}{\sqrt{2}}(2N_e - N_n) & \frac{\delta m^2}{4E} \sin 2\theta & \mu_{ee} B & \mu_{e\mu} B \\ \frac{\delta m^2}{4E} \sin 2\theta & -\frac{G}{\sqrt{2}} N_n + \frac{\delta m^2}{2E} \cos 2\theta & \mu_{\mu e} B & \mu_{\mu\mu} B \\ \mu_{ee} B & \mu_{e\mu} B & 0 & 0 \\ \mu_{\mu e} B & \mu_{\mu\mu} B & 0 & \frac{\delta m^2}{2E} \cos 2\theta \end{pmatrix} \begin{pmatrix} \nu_{eL} \\ \nu_{\mu L} \\ \nu_{eR} \\ \nu_{\mu R} \end{pmatrix} \quad (\text{eq 3-44})$$

In the Dirac neutrino case there are no weak potentials (interactions with electrons, protons and neutrons) for ν_{eR} and for $\nu_{\mu R}$ because they are sterile. Neutrino flavor mixing is considered only for left-handed neutrinos. The Hamiltonian for RSFP without flavor mixing is a special case of that for the hybrid model when the mixing angle $\theta = 0$.

In the Majorana neutrino case, $\bar{\nu}_e$ and $\bar{\nu}_\mu$ are not sterile. The propagation equation for Majorana neutrinos is found to be

$$i \frac{d}{dt} \begin{pmatrix} \nu_e \\ \nu_\mu \\ \bar{\nu}_e \\ \bar{\nu}_\mu \end{pmatrix} = \begin{pmatrix} \frac{G}{\sqrt{2}}(2N_e - N_n) & \frac{\delta m^2}{4E} \sin 2\theta & 0 & \mu B \\ \frac{\delta m^2}{4E} \sin 2\theta & -\frac{G}{\sqrt{2}} N_n + \frac{\delta m^2}{2E} \cos 2\theta & -\mu B & 0 \\ 0 & -\mu B & -\frac{G}{\sqrt{2}}(2N_e - N_n) & \frac{\delta m^2}{4E} \sin 2\theta \\ \mu B & 0 & \frac{\delta m^2}{4E} \sin 2\theta & \frac{G}{\sqrt{2}} N_n + \frac{\delta m^2}{2E} \cos 2\theta \end{pmatrix} \begin{pmatrix} \nu_e \\ \nu_\mu \\ \bar{\nu}_e \\ \bar{\nu}_\mu \end{pmatrix} \quad (\text{eq 3-45})$$

Neutrino flavor mixing is also considered for anti-neutrinos.

In the Majorana neutrino case, it must be noted that we can expect solar $\bar{\nu}_e$ creation [ref 3-15]. From the propagation equation (eq 3-45), resonance conditions for $\nu_e \rightarrow \nu_\mu$ by the MSW effect and for $\nu_e \rightarrow \bar{\nu}_\mu$ ($\nu_\mu \rightarrow \bar{\nu}_e$) by spin flavor precession are obtained by

$$2\sqrt{2}GN_e E = \delta m^2 \cos 2\theta \quad (\nu_e \rightarrow \nu_\mu) \quad (\text{eq 3-46})$$

$$2\sqrt{2}G(N_e - N_n)E = \delta m^2 \cos 2\theta \quad (\nu_e \rightarrow \bar{\nu}_\mu, \nu_\mu \rightarrow \bar{\nu}_e). \quad (\text{eq 3-47})$$

The resonance condition (eq 3-46) is the same as the condition (eq 3-32) obtained by the consideration of flavor mixing alone. The resonance region for MSW oscillation, where

$$N_{e\text{MSW}} = \frac{\cos 2\theta}{2\sqrt{2}GE}$$

is inside the resonance region for RSFP, where

$$N_{e\text{RSFP}} = \frac{\cos 2\theta}{2\sqrt{2}GE} + N_n > N_{e\text{MSW}}.$$

Therefore, the neutrinos produced at the center of the sun cannot satisfy the MSW resonance condition along their track to the surface of the sun before satisfying the RSFP condition, and we cannot expect $\bar{\nu}_e$ creation by the process,

$$\nu_e \xrightarrow{\text{MSW}} \nu_\mu \xrightarrow{\text{RSFP}} \bar{\nu}_e \quad (\text{eq 3-48})$$

But, instead of the process (eq 3-48), we can expect $\bar{\nu}_e$ creation through the process,

$$\nu_e \xrightarrow{\text{RSFP}} \bar{\nu}_\mu \xrightarrow{\text{Vacuum Oscillation}} \bar{\nu}_e \quad (\text{eq 3-49})$$

This conversion needs a large mixing angle to create a sufficient number of $\bar{\nu}_e$, because vacuum oscillation must take place in the conversion.

If the conversion (eq 3-49) happens, Kamiokande may detect the resultant $\bar{\nu}_e$, because the cross section $\sigma(\bar{\nu}_e p \rightarrow e^+ n)$ is fortunately two orders of magnitude larger than $\sigma(\nu_e e^-)$ at 10 MeV of neutrino energy, and the produced positron keeps the neutrino energy,

$$E_{e^+} = E_\nu - 1.293 \text{ MeV}. \quad (\text{eq 3-50})$$

In this thesis, we study and give a limit on this possible $\bar{\nu}_e$ creation with the Kamiokande detector.

Chapter 3. Neutrino Oscillation and Resonant Spin Flavor Precession

References

- [3-1] L.Ahrens et al., Phys.Rev. **D31**(1985)2732; L.S.Durkin et al., Phys.Rev.Lett. **61**(1988)1811; C.Angelini et al., Phys.Lett. **B179**(1986)307; B.Blumenfeld et al., Phys.Rev.Lett. **61**(1989)2237.
- [3-2] Review paper: S.Parke, preprint Fermilab-Conf-93/056-T, "Overview of Accelerator Long Baseline Neutrino Oscillation Experiments", April 1993.
- [3-3] G.Zacek et al., Phys.Rev. **D34**(1986)2621.
- [3-4] J.D.Vergados, Phys.Rep. **133**(1986)1.
- [3-5] M.Takita, Ph.D. thesis, Univ. of Tokyo (1989), ICRR-Report-186-89-3.
- [3-6] K.S.Hirata et al., Phys.Lett. **B280**(1992)146; K.Gabathuler et al., Phys.Lett. **B138**(1984)449; F.Daydak et al., Phys.Lett. **B134**(1984)281; F.Bergsma et al., Phys.Lett. **B142**(1984)103; Ch.Berger et al., Phys.Lett. **B245**(1990)305.
- [3-7] S.Pakvasa and J.Pantaleone, preprint of Dep.of Phys.and Astron., Univ.of Hawaii at Manoa Honolulu, HI96822, No.UH-511-701-90/UCRHEP-T56, 1990; R.S.Raghavan et al., AT&T Bell labs Tech. Memorandum 11121-910204-16 (Feb.4,1991).
- [3-8] A.Suzuki, preprint KEK Preprint 93-96, "Solar Neutrinos, Atmospheric Neutrinos and Proton Decays in Kamiokande", August 1993.
- [3-9] J.Pulido, Phys.Rep. **211**(1992)167.
- [3-10] L.D.Landau, Phys.Z.Sowjetunion **2**(1932)46; C.Zener, Proc.R.Soc.London **A137**(1932)696; E.C.G.Stueckelberg, Helv.Phys.Acta **5**(1932)369.
- [3-11] S.J.Parke, Phys.Rev.Lett. **57**(1986)1275; W.C.Haxton, Phys.Rev.Lett. **57**(1986)1271; T.K.Kuo and J.Pantaleone, Phys.Rev. **D39**(1989)1930.
- [3-12] A.J.Baltz and J.Weneser, Phys.Rev. **D35**(1987)528.
- [3-13] A.Schäfer and S.E.Koonin, Phys.Lett. **B185**(1987)417.
- [3-14] A.Cisneros, Astrop.Space.Sci. **10**(1981)87.
- [3-15] E.Kh.Akhmedov, preprint, I.V.Kurchatov Institute of Atomic Energy, No.IAE-5197/1,1990; R.Barbieri, G.Fiorentini,G.Mezzorani and M.Moretti, Phys.Lett. **B259**(1991)119.

4. The Kamiokande-III detector

4.1. Short history of Kamiokande

Kamiokande (Kamioka Nucleon Decay Experiment, or it may be better to call it the Kamioka Neutrino Detection Experiment in this thesis) started in July 1983 [ref 4-1]. The purpose of the experiment was, at first, to search for nucleon decays [ref 4-1,4-2]. The Kamiokande detector is located 1000 m underground (2700 m.w.e. due to a rock density of 2.7 g/cm^3) in the Kamioka mine at 36.42°N and 137.31°E (25.8°N for geomagnetic latitude), about 250 km west of Tokyo, in Japan. This mine is in active operation and produces mainly zinc and lead. This mine was chosen as the experimental site for the following reasons:

- It is necessary to reduce the cosmic ray background to a manageable level. The muon flux at the Kamiokande is 10^{-5} relative to the flux at the ground level. The Kamioka mine is one of the deepest mines in Japan.
- The rock is sufficiently hard and stable to excavate a large cavity.
- The experimental site is horizontally accessible by a small train (and now by a car), so it is convenient to maintain and operate the detector daily.
- A sufficient amount of clean water is available from a nearby natural water source.
- The temperature is low and stable ($\sim 13^\circ\text{C}$) because the location is not deep, therefore, moderate air conditioning is sufficient.

After some improvement of the detector (anti-counter, TDC, water purification system and so on), Kamiokande entered into a new phase to observe low energy neutrino interactions (i.e. solar neutrinos, supernova neutrinos and so on) in November 1985 [ref 4-3]. The previous phase and the new phase were called Kamiokande-I and Kamiokande-II, respectively.

At the beginning of Kamiokande-II, much work to reduce the background in the low energy region was done in order to accomplish solar neutrino observation. Especially,

elimination of radon was (and remains) the most important among them. Finally, the background level became sufficiently low and the solar neutrino observation started in January 1987. Right after the beginning of the observation, the famous neutrino burst from SN1987A was detected in February 1987 [ref 4-4]. This is the beginning of "Neutrino astronomy"; a new field in physics.

Kamiokande-II has been divided into two phases, because the PMT gain was increased by a factor of 2 (3×10^6 to 6×10^6) in June 1988 in order to improve the PMT response corresponding to a single photo-electron signal [ref 4-5]. Kamiokande-II ended its operation in April 1990 to replace dead PMTs after 1040 days of data accumulation for solar neutrino observation. We replaced 120 dead PMTs, installed new electronics which has better timing resolution than that of Kamiokande-II, and attached light reflectors around every inner-PMT to increase an effective photo-coverage. We resumed solar neutrino observation in December 1990. The new phase was named as Kamiokande-III.

Improvements for Kamiokande-III are;

- new electronics modules (see section 4.6),
- light reflectors around inner-PMTs (see subsection 4.5.2),
- powerful radon-free air system (see subsection 4.7.3), and
- powerful degasifier (see also subsection 4.7.2).

The Kamiokande-III was once used for a cold fusion experiment as an ultra low background laboratory [ref 4-6]. It could be another possibility for underground detectors to supply their ultra low background environments to other special experiments.

Kamiokande-III is still continuing, and we analyze and discuss 514 days of data (from December 1990 to February 1993) for solar neutrino observation in this thesis.

4.2. Ring imaging water Cherenkov detector

The Kamiokande detector is a ring imaging Cherenkov detector filled with 3000 tons of pure water.

Electro-magnetic radiation (Cherenkov photons) is emitted by a charged particle traversing a medium, if the velocity of the charged particle βc is larger than the light velocity in the medium, c/n , namely,

$$n\beta > 1, \quad (\text{eq 4-1})$$

where n is the refraction index of the medium. This emission was first discovered by Cherenkov in 1934 and was theoretically proved by Frank and Tamm [ref 4-7]. The value depends on the wavelength of the light. It varies from 1.350 to 1.336, in the relevant region for a water Cherenkov detector with photo-multiplier tubes ($\lambda = 330 \text{ nm} \sim 500 \text{ nm}$). The average value is 1.344. Cherenkov photons are emitted on a cone with an opening angle from the direction of the particle path,

$$\cos\theta = \frac{1}{n\beta}. \quad (\text{eq 4-2})$$

If the particle is relativistic in water (our detector), the opening angle is 42° . The number of photons emitted per unit track length per unit wave number is given by;

$$\frac{d^2N}{dx dv} = \frac{2\pi\alpha}{c} \left(1 - \frac{1}{n^2\beta^2}\right), \quad (\text{eq 4-3})$$

where α is the fine structure constant, x the path length of the charged particle, ν the wave number of the emitted photon and c the speed of light. The number of Cherenkov photons emitted in the visible region is about 250 per cm. The minimum energy requirement for Cherenkov light emission depends on the particle mass through $n\beta > 1$. It should be noted that Cherenkov radiation is a very small fraction ($\sim 10^{-4}$) of the total energy loss of a charged particle through matter. The total number of Cherenkov photons is proportional to the energy of the charged particle in the energy region where its mass is negligible, because the track length of the charged particle is almost proportional to its energy. The recoil electron energy of the solar neutrino interaction, several MeV to 18 MeV, satisfies this condition. These features (eq 4-2 and 4-3) are useful in determining the energy (momentum) and direction of charged particles.

Cherenkov photons are detected by photo-multiplier tubes (PMT) which are arranged two-dimensionally on the detector walls to view the entire target material (pure water). The image becomes a ring pattern in the case where the particle stopped inside the detector or a filled circle in the case where the particle escaped the detector. The vertex, direction and energy can be determined using the pattern, the charge and timing information of each hit PMT.

Advantages of the ring imaging water Cherenkov detector for solar neutrino observation are:

- It can provide real time observation.
- The energy spectrum of recoil electrons produced by solar neutrinos can be measured.
- The direction of recoil electrons, which have a strong directional correlation with that of the incoming neutrino, is measurable and we are able to know where the neutrinos come from.

4.3. Neutrino interactions in Kamiokande

4.3.1. Dominant processes in the energy region of solar neutrinos

The Kamiokande detector holds 2140 tons of water within its photo-sensitive volume. Therefore, the number of target particles in the detector are

$$e^- : 7.16 \times 10^{32},$$

$$\text{free protons} : 1.43 \times 10^{32},$$

$$\text{oxygen} : 7.16 \times 10^{31}.$$

There are three generations of neutrinos, ν_e , ν_μ , ν_τ and there also exist their anti-particles, $\bar{\nu}_e$, $\bar{\nu}_\mu$, $\bar{\nu}_\tau$. Interactions of these neutrinos below 20 MeV (the energy region of solar neutrinos) are dominated by the following processes:

$$\nu_e + e^- \rightarrow \nu_e + e^- \quad (\text{eq 4-4})$$

$$\nu_\mu(\tau) + e^- \rightarrow \nu_\mu(\tau) + e^- \quad (\text{eq 4-5})$$

$$\bar{\nu}_e + p \rightarrow e^+ + n \quad (\text{eq 4-6})$$

$$\bar{\nu}_\mu(\tau) + e^- \rightarrow \bar{\nu}_\mu(\tau) + e^- \quad (\text{eq 4-7})$$

Interaction with an oxygen nucleus is negligible because the energies of the neutrinos are too low to excite an oxygen nucleus and to make an observable signal [ref 4-8].

4.3.2. Neutrino-electron elastic scattering

The differential cross section of elastic scattering on electrons is given by [ref 4-9]

$$\frac{d\sigma(\nu e^-)}{dy} = \frac{G_F^2 m_e E_\nu}{2\pi} \left[A_0 + B_0(1-y)^2 + C_0 m_e \frac{y}{E_\nu} \right], \quad (\text{eq 4-8})$$

where y is the ratio of the kinetic energy of the recoil electron T_e to the incoming neutrino energy E_ν ; $y = \frac{T_e}{E_\nu}$, $G_F = 1.16639 \times 10^{-5} \text{ GeV}^{-2}$ [ref 2-3] and $m_e = 0.511 \text{ MeV}$ are the Fermi coupling constant and the electron rest mass, respectively. The parameters A_0 , B_0 , C_0 are defined by

$$A_0 = (g_V + g_A)^2, B_0 = (g_V - g_A)^2, C_0 = g_A^2 - g_V^2. \quad (\text{eq 4-9})$$

$$g_V = 2\sin^2\theta_W + \frac{1}{2} \quad \text{for } \nu_e \quad (\text{eq 4-10})$$

$$= 2\sin^2\theta_W - \frac{1}{2} \quad \text{for } \nu_\mu(\tau) \quad (\text{eq 4-11})$$

$$g_A = +\frac{1}{2} \quad \text{for } \nu_e \quad (\text{eq 4-12})$$

$$= -\frac{1}{2} \quad \text{for } \nu_\mu(\tau). \quad (\text{eq 4-13})$$

For anti-neutrinos, we can get the parameters by replacing g_A with $-g_A$. The recent accurate measurement gives $\sin^2\theta_W$ to be 0.2259 ± 0.0029 (in the on-shell scheme) [ref 2-3]. The values of A_0 , B_0 , C_0 for the neutrinos then become [ref 4-10];

| | A_0 | B_0 | C_0 |
|-----------------------|-------|-------|--------|
| ν_e | 2.123 | 0.220 | -0.683 |
| $\nu_\mu(\tau)$ | 0.295 | 0.220 | 0.255 |
| $\bar{\nu}_e$ | 0.220 | 2.123 | -0.683 |
| $\bar{\nu}_\mu(\tau)$ | 0.220 | 0.295 | 0.255 |

The total cross sections for these neutrinos to scatter are obtained by integrating the differential cross sections from 0 to y_{max} .

$$\sigma_{\text{total}} = \int_0^{y_{\text{max}}} \frac{d\sigma}{dy} dy = \frac{GF^2 m_e E_\nu}{2\pi} \left[A_0 y_{\text{max}} + \frac{B_0}{3} \{1 - (1 - y_{\text{max}})^3\} + C_0 \frac{m_e y_{\text{max}}^2}{2E_\nu} \right]. \quad (\text{eq 4-14})$$

where, y_{max} is a kinematical limit expressed by

$$y_{\text{max}} = \frac{2E_\nu}{2E_\nu + m_e}. \quad (\text{eq 4-15})$$

Note that $\nu_\mu e^-$ and $\nu_\tau e^-$ can take place only through a neutral current interaction and the total cross section is about six times less than that of $\nu_e e^-$ scattering which also has a contribution from the charged current interaction as shown in Fig. 4.1. The cross section of $\bar{\nu}_{\mu(\tau)} e^-$ is the same order as that of $\nu_{\mu(\tau)} e^-$ as also shown in Fig. 4.1. The overall factor in the total cross section is

$$\frac{GF^2 m_e E_\nu}{2\pi} = 4.31 \times 10^{-45} \times E_\nu \text{ (cm}^2\text{)}. \quad (\text{eq 4-16})$$

E_ν is the energy of incoming neutrino in units of MeV. For example, assuming $E_\nu = 10$ MeV, a typical energy of a ^8B solar neutrino, the cross sections of neutrino and electron elastic scattering are 0.916×10^{-43} cm² for ν_e , 0.158×10^{-43} cm² for $\nu_{\mu(\tau)}$, 0.390×10^{-43} cm² for $\bar{\nu}_e$ and 0.137×10^{-43} cm² for $\bar{\nu}_{\mu(\tau)}$.

The direction of the recoil electron with respect to the direction of the incoming neutrino is kinematically determined by

$$\cos\theta = \frac{1 + \frac{m_e}{E_\nu}}{\sqrt{1 + \frac{2m_e}{T_e}}}. \quad (\text{eq 4-17})$$

The opening angle of the recoil electron and incoming neutrino (direction of the sun) for neutrino-electron elastic scattering is less than 20° in the energy region of $E_e \geq 7.0$ MeV as shown in Fig. 4.2. The kinematical limit of the opening angle is obtained by setting $E_\nu \rightarrow \infty$ in (eq 4-17);

$$\theta^2 \leq \frac{2m_e}{T_e}. \quad (\text{eq 4-18})$$

The angular resolution is limited by the multiple scattering of electrons and is about 28° at 10 MeV. Therefore, we can count up the number of solar neutrino signals due to this strong correlation between the direction of recoil electrons and that of the sun.

4.3.3. Capture cross section of a free proton for $\bar{\nu}_e$

In the case of $\bar{\nu}_e$, the situation is different from that of ν_e . The dominant process is $\bar{\nu}_e + p \rightarrow e^+ + n$, not electron scattering. The total cross section of $\bar{\nu}_e + p \rightarrow e^+ + n$ is given by [ref 4-11]

$$\alpha(\bar{\nu}_e p) = \frac{G^2}{\pi} \frac{E_e}{m_e} \frac{p_e}{m_e}, \quad (\text{eq 4-19})$$

where G^2 is the appropriate β coupling constant, and m_e , E_e and p_e are the rest mass of the electron and the total energy and momentum of the produced positron, respectively. We can derive G^2 from the relation,

$$\frac{G^2}{2\pi} = \frac{\pi^2}{\tau_n m_e^3} \frac{1}{F(\eta_0)}. \quad (\text{eq 4-20})$$

$\tau_n = 889.1 \pm 2.1$ seconds [ref 2-3] is the mean life time of a neutron and $F(\eta_0) = F(\frac{p_{\text{max}}}{m}) = F(2.324) = 1.633$ is the Fermi function. Then, the total cross section of $\bar{\nu}_e + p \rightarrow e^+ + n$ is;

$$\alpha(\bar{\nu}_e p) = 1.00 \times 10^{-43} E_e p_e \text{ [cm}^2\text{MeV}^{-2}\text{]}. \quad (\text{eq 4-21})$$

The total cross section of $\bar{\nu}_e p$ is about a hundred times (actually 20 times, taking into account the composition of water; H₂O: two protons, ten electrons and one oxygen) larger than that of $\nu_e e^-$ elastic scattering at 10 MeV as shown in Fig. 4.1.

The produced positron has the kinetic energy of $T_e = E_\nu - 1.804$ MeV, while the energy of the recoil electron from neutrino electron elastic scattering distributes as $T_e^{\text{max}} = y_{\text{max}} \times E_\nu$ according to (eq 4-8) and (eq 4-15). By this means, we can observe the energy of $\bar{\nu}_e$ on an event by event basis.

The angular distribution of positron is given by [ref 4-12]

$$\frac{d\sigma}{d\Omega} = \frac{G^2}{4\pi^2} \frac{E_e}{m_e} \frac{p_e}{m_e} \left(1 - 0.093 \cos\theta \frac{p_e}{E_e}\right) \quad (\text{eq 4-22})$$

$$\left\{ = \frac{(G_F \cos \theta_c)^2}{4\pi^2} (g_V'^2 + 3g_A'^2) E_e p_e \left(1 - \frac{g_A'^2 - g_V'^2}{g_V'^2 + 3g_A'^2} \cos \theta \frac{p_e}{E_e} \right) \right\}$$

θ is the opening angle between incoming $\bar{\nu}_e$ and produced positron, $\cos \theta_e = 0.9753$ [ref 2-3], the Cabibbo angle, $g_V' = 1$ and $g_A' = -1.2573$ [ref 2-3]. This equation shows so small a directional correlation that it is hard to obtain the direction of the incoming neutrino from the observation of the positron. It also makes it difficult to count up the number of neutrino events without perfect knowledge of the background except in a special case such as a neutrino burst like SN1987A.

4.4. Water tank

The Kamiokande detector has a cylindrical shape and consists of inner and anti-counters. The cavity which houses the whole detector has a size of 19 m in diameter, 23 m high at the central axis and 16 m high at the straight section along the wall. The entire wall of the cavity is reinforced by the metal nets and sprayed concrete layers; moreover the wall is coated by rubber-asphalt for waterproofing. Helmholtz coils are arranged on the cavity walls to compensate the geomagnetic field (0.45 gauss) that would affect the PMT gain.

A cylindrical steel tank of 15.6 m in diameter and 16.1 m in height is placed inside this cavity. This tank is filled with 3000 tons of pure water. The steel water tank is 12 mm thick at the bottom and gradually becomes thinner toward the top where it is 4.5 mm thick. The inner surface of the tank is painted black with a specially prepared epoxy, the most suitable paint for pure water, and the thickness of the paint is 250 μm . The outside of the water tank is coated with the rubber-asphalt. A steel cover is placed on the top of the water tank to seal off the radon-rich air from the space above the top of the tank.

Inside the water tank is the inner detector (948 PMTs viewing 2140 tons of pure water), the top part of anti-counter (22 PMTs) and the bottom part of anti-counter (21 PMTs). These sections are separated by black sheets. The gap between the water tank and the cavity wall is filled with 1400 tons of water. This is the barrel anti-counter with

80 PMTs (5 in column and 16 in row). The total number of PMTs for the anti-counter is, thus, 123. The density of PMTs is about 1 PMT / m^2 for the inner detector (this corresponds to 20% photo-coverage) and 1 PMT / 9 m^2 for the anti-counter. The inner surface of the whole anti-counter is covered by aluminized Mylar sheets to get better light collection efficiency. The typical thickness of the anti-counter is 0.7 m for the top, 1.2 m for the bottom, and 1.5 m for the barrel part. The anti-counter is utilized for identifying a cosmic ray muon which penetrates the counter and is effective in shielding the detector against the gamma rays and neutrons being generated in the rock surrounding the detector.

The schematic view of the tank and the cavity is illustrated in Fig. 4.3.

4.5. Photo multiplier tube (20" ϕ PMT)

The characteristics of the PMTs used in Kamiokande-II are described in appendix A. Kamiokande-III contains 120 new improved PMTs, and the difference from the ones used in Kam-2 is described here.

4.5.1. Improvement of PMTs for Kamiokande-III

Kamiokande-III has 120 new type PMTs which were developed for the future larger water Cherenkov detector (i.e. Super-Kamiokande) [ref 4-13] with better timing resolution and better water resistance than the Kam-2 type and with a clear single photo-electron peak. For low energy events such as solar neutrinos, each PMT catches mainly one photon. The timing resolution and the resolution of the pulse height for a single photo-electron is crucial for the measurement.

The size and shape of the new 20" ϕ PMTs are almost same as that used in Kam-2 except for the minor modification of lengthening the glass-multisealing line near the socket to obtain better water resistance (see Fig. 4.4). The structure of the Venetian blind type dynode has been modified. The bleeder-chain was optimized with an 11 stage voltage divider (see Fig. 4.5) while the old PMT has 13 stages. Three types of focusing mesh-plates between the cathode and the first dynode were added in exchange for the reduction of the dynode stages. This design was made in such a way for

electrons not to hit the same nor neighboring dynode again and not to pass through the gap of the plates without hitting, and not to have long flight paths (see Fig. 4.6) which was based on the electron trajectory simulation mentioned in Appendix A. These are the main source of the transit time spread and the pulse height spread. Due to this improvement, the timing resolution for the single electron level became less than 3 nsec, and the single photo-electron peak can now be clearly seen. Fig. 4.7 shows the typical transit time distribution for the single photon, and Fig. 4.8 shows the typical pulse height distribution for the single photon. These improvements did not affect the magnetic properties (see Fig. 4.9) nor the cathode and anode uniformity (see Fig. 4.10).

The timing response for the new type PMTs is measured as described in appendix C.2. The timing resolution on the output pulse height is drastically improved at the single photon level as shown in Fig. 4.11. We can also see an improvement of the timing resolution for the old type PMTs in Kam-3 because the new electronics described in subsection 4.6.1 has a better timing resolution than that of Kam-2.

4.5.2. Light reflector

In order to increase the effective light-sensitive area, a light reflector was attached to each inner-PMT (for the Kamiokande-III detector) as shown in Fig. 4.12.

The reflector was made of a 25 μm aluminized PET (polyethylene terephthalate) sheet which was back-coated by 300 μm PET with a dry-ruminate glue to prevent the aluminum from coming in contact with the pure water. The reflection efficiency is about 80%.

The shape of the reflector was chosen to be a cone, and the size was optimized to maximize the light collection efficiency and to be not affected for the Cherenkov pattern by photons coming from the other light reflectors. The size thus chosen was 10 cm in height and the angle between the sheet and the wall was 60°.

The light collection efficiency (or the light coverage) was increased by about 27% (the light-sensitive area has increased effectively from 20% to 25%). The benefits from the increase of the collection efficiency are:

- The vertex resolution was improved by about 10 cm in the entire energy region as shown in Fig. 4.13. (Better timing resolution of the new electronics also contributes to this improvement.)
- The angular resolution became better in the low energy region around 7 MeV as shown in Fig. 4.14. The resolution is already limited by multiple scattering of electrons in the energy region above 10 MeV.
- The energy resolution was also improved in the low energy region (see Fig. 4.15). The limitation on the energy resolution in the energy region above 10 MeV comes from another effect of the light reflector as described below.

However an improvement for high energy events due to the light reflector was not accomplished, since we did not increase the number of PMTs, just the light coverage. The probability that a PMT catches more than 1 p.e. increased in the energy region above around 10 MeV. This probability gets much larger for events with vertices near the PMT plane. Hence, the number of hit PMTs varies depending on the vertex position. This effect is schematically illustrated in Fig. 4.16. Since we use the number of hit PMTs for the energy scale, the energy resolution for higher energy events cannot be improved because of this effect. Topics related to this effect are described in the section on the energy scale (subsection 5.1.4).

4.5.3. High Voltage monitoring system

The High Voltage (H.V.) monitoring system installed in Kamiokande-III consists of (i) computer controlled relay circuits to select each channel, and (ii) a 16-bit ADC to measure the H.V. (1/1000). Relay circuits to shut off the H.V. of any PMTs are also prepared.

PMTs have become out of order during their operation with a rate of about 20 PMTs per year. There is no single cause, but leakage of water is thought to be a major one.

When a PMT dies, it usually becomes a "flash-PMT" which emits bursts of light. Emission is sometimes consecutive and the rate is very high. In any case, it is very troublesome.

The H.V. monitoring system is also used to search for the "flash-PMTs" which occasionally pull a larger current resulting in a voltage drop that is detectable by measuring the H.V. The H.V. monitoring system can turn off the channel where a voltage drop is happening.

4.6. Electronics

For solar neutrino observation in Kamiokande, it is essential to have timing information and to increase the detection efficiency for a single photo-electron signal.

A typical Cherenkov pattern for an event around 10 MeV is shown in Fig. 4.17. The number of hit PMTs for a low energy event is small (a 10 MeV electron hits about 26, 30, and 40 PMTs in the Kam-2 gain \times 1, Kam-2 gain \times 2, and Kam-3, respectively). Its Cherenkov ring pattern is influenced by multiple scattering, moreover the number of hit PMTs is affected by the dark current of the PMTs (about 4 hits within the 1.1 μ sec window for the signal). Therefore, it is not good to reconstruct the vertex and the energy of the event only from the Cherenkov pattern. Timing information is useful for vertex reconstruction and rejection of the dark current. By making corrections on timing information of the flight time from the vertex to PMT and of the pulse height dependence of time, we can make a signal distribute over a narrower region (40 nsec). The number of accidental hits from the dark current can be suppressed to about 0.1 hits for an event.

The Kam-2 electronics has TDC modules for obtaining the timing information from each PMT. The details on the Kam-2 electronics are described in appendix B.

The installation of a new electronics for Kamiokande-III was completed in November 1990. It is a challenging electronics containing both analog and digital (for example, ADC) circuits on the same board to simplify the configuration. The new

electronics module does not need an additional signal delay cable because of the common stop scheme of time measurement.

4.6.1. Electronics for Kamiokande-III

The electronics installed for Kamiokande-III [ref 4-14] was specifically developed for this experiment. The Kamiokande-III electronics consists of 90 front-end modules (ATMs, short for Analog Timing Modules) (79 modules for the inner-detector and 11 modules for the anti-counter) in which each module has 12 input channels. The ATM modules are arranged in 5 TKO-system (abbreviation of TRISTAN / KEK Qn-line) crates where one crate can accommodate 20 ATM modules.

Each TKO-crate section needs additional modules; 1 bus-interface module (CH, short for Control Head) and 1 trigger distribution card (GONG, short for GO No-Go Module). The data buffer modules (MB, short for Memory Buffer) (1 MB for 1 CH) are arranged to store data from ATM for computer read-out. One trigger control card (TRG) and some support modules are also integrated for whole system. The ATM, CH and GONG are TKO-system modules, and the MB and TRG are CAMAC modules.

The data flow in the Kamiokande-III electronics is schematically drawn in Fig. 4.18. The strategy of the data taking in Kamiokande-III is similar to that of the Kam-2 electronics. But the ATM module has salient features with respect to the front-end module used in Kam-2. A detailed explanation of these modules are described below.

◆ Front end module (ATM):

The advantages of the ATM module are:

- (i) compact (it has 12 channel inputs) and all-in-one. The following are organized in one ATM module (on a 6 layer printed board): amplifiers, signal delays, discriminators, analog buffers with double depth for every channel, ADC, control logic, 8-bit event counter which generates the event ID, analog sum circuit, hit sum circuit which sums up the digital output (2.5 mV in height, 100 nsec in width) from the discriminators, FIFO memory, and so on.
- (ii) large FIFO memory which can store 170 hits of information,

- (iii) fast digitizer which enables high rate data taking such as a neutrino burst from a stellar collapse, and
- (iv) good timing resolution.

The ATM module processes the signal from a PMT as follows (see Fig. 4.19):

- (1) The ATM receives the signal from the front panel of the module with 50Ω impedance.
- (2) The signal is divided into four by the current splitter.
- (3) One of them is amplified by a factor of 400, and is sent to the discriminator. The threshold of the discriminator set through the GONG was adjusted to 36.6 mV, which corresponds to ~ 0.2 p.e. (all channels in a crate have the same threshold). If the pulse height exceeds the threshold, a rectangular pulse (2.5 mV in height and 100 nsec in width) is generated. Then, the digital pulses from each of the 12 channels, if generated, are summed and sent to the GONG to make a total "hit-sum" signal within a crate.
- (4) The "analog-sum" signal is produced in a similar way to the "hit-sum" signal. It uses one of the 4 split signals instead of the rectangular pulse.
- (5) The other two split signals are sent to the time-to-analog converter (TAC) and to the charge-to-analog converter (QAC) [ref 4-15] through a 200 nsec delay.
- (6) Each channel has two TACs (which are called the A and B channels) and QACs. When a discriminator is fired, the TAC for the channel starts to charge up the capacitor until the global trigger arrives. If the global trigger does not come within 1.1 μ sec, the channel is reset. If the global trigger occurs, the voltage (0-1 μ sec is converted to 0-5 V) is stored for the digitization, and another TAC is enabled for the next event.
- (7) The QAC also integrates charge and converts it to voltage (0-400 pC is converted to 0-5 V).
- (8) The event ID, which is counted up by the event counter, is latched for the hit channel.

- (9) The ATM has one analog-to-digital converter (ADC), which converts both the TAC output and the QAC output with a 12-bit full scale (conversion time is 1.5 μ sec). 1 nsec corresponds to 3 counts of the digital output, and 1 p.e. corresponds to 7.8 counts. If the global trigger occurs, the stored analog data (in the TAC and QAC) are digitized by the ADC. The latched event ID and the digitized data are then written on the two 9-bit \times 512 FIFO memories. It takes about 10 μ sec to process one hit signal (containing both time and charge information).
- (10) If the global trigger occurs, the event counter is incremented for the next event. The event ID for every hit-channels has previously been latched before the global trigger arrives.

◆ Bus-interface module, Control Header (CH):

The CH is a TKO module which controls the TKO digital-bus and receives commands from a MB module on the CAMAC bus and sends data to the MB. It can transfer the data in the ATM modules to the MB module with a transmission rate more than 2 mega-bytes / sec.

◆ Memory buffer (MB):

The MB module is a CAMAC 2 span module. It receives the data from the ATMs through the CH, and stores the data on its 32 kB memory. The transmission between the CH and the MB is done through RS-422. Then, the on-line computer reads the data stored in the MB module. The control of the MB is made by a 80186(8 MHz) CPU on board.

◆ Trigger distribution card (GONG)

The GONG is a TKO module. This module sums up both the "hit-sum" and the "analog-sum" signal from the ATM modules in a crate. The "sum" outputs from 4 GONG modules are sequentially connected, and the total sum for the entire inner detector is made. The total "hit-sum" is sent to the discriminator for a decision on the trigger, and the total "analog-sum" for the inner detector is sent to a flash ADC to see a decay electron from a muon. The "analog-sum" of the anti-counter delayed by

about 20 μ sec is also sent to a flash ADC and is used to observe a parent muon which did not deposit its energy in the inner detector.

The GONG module also receives the global trigger pulse from the TRG, and distributes it to the ATMs in the crate.

The GONG also has a 16-bit digital-to-analog converter (DAC) to set a threshold level for ATM modules. The threshold level is distributed to the ATMs through the back-plane.

◆ Trigger control module (TRG):

The TRG module is a CAMAC 2 span module. It operates the same as the timing card of the Kam-2 electronics (see appendix B). The TRG can accept four different trigger inputs and can record the trigger type in its FIFO memory. The TRG can store the time, which is counted by a 50 MHz (later changed to 25 MHz) scalar with 48-bit full scale, and the event ID, which is counted by the 8-bit event counter, on the FIFO memory. The data size of the TRG for one trigger is 8 bytes, and the FIFO memory has 1 kB. The trigger signal is distributed to all ATMs through the GONGs, to the flash ADCs, to the on-line computer and so on.

4.6.2. Trigger

As described in section 4.2, the electron energy is proportional to the total number of photo-electrons. A noisy PMT or a "flash-PMT" may obscure the number of photo-electrons at the desirable trigger threshold (~ 20 p.e.) for solar neutrino observation. Fortunately, the number of total p.e.s is almost the same as the number of hit PMTs in low energy region, and the number of hits is not so much influenced by a noisy PMT. Therefore, the number of hit PMTs is a good energy scale and is used for trigger discrimination. This strategy is used both in Kamiokande-II and in Kamiokande-III.

The threshold for each hit-signal is set to 0.35 p.e. (Kam-2 gain $\times 1$), 0.18 p.e. (Kam-2 gain $\times 2$) and 0.2 p.e. (Kam-3). The hit-signal of each channel has a rectangular shape with about a 5 mV height and 100 nsec width for Kam-2 and about a 2.5 mV height and 100 nsec width for Kam-3. The total "hit-sum" signal is discriminated with the "master threshold" of 112 mV (Kam-2) or of 45 mV (Kam-3). As the number of

dead tubes increases, the number of hit PMTs decreases, hence, the threshold must be lowered to keep the same energy threshold. The "master threshold" of the Kamiokande-III was lowered to 40 mV in June 1992 for this reason.

The trigger rate is another reason to change the "master threshold." Due to the decrease of radon in the water the trigger rate in Kam-2 has decreased, and the "master threshold" was lowered to 100 mV in October 1987 from 112 mV. It was changed back to 112 mV in June 1988 when the PMT gain was doubled.

These "master thresholds" correspond to the threshold energy of 7.6 MeV (Kam-2 gain $\times 1$, 112 mV), 6.7 MeV (Kam-2 gain $\times 1$, 100 mV), 6.1 MeV (Kam-2 gain $\times 2$) and about 5 MeV (Kam-3) in the fiducial volume for the solar neutrino analysis. The energy threshold means the energy at which the trigger efficiency becomes 50%. Fig. 4.20 shows the trigger efficiency curve of Kam-3 as a function of electron energy (detector resolution is convoluted). The fluctuation of the trigger threshold does not affect the solar neutrino analysis because the trigger threshold is low enough compared to the analysis threshold. Fig. 4.21 shows the trigger efficiency curve of Kam-3 as a function of visible energy (detector resolution is not convoluted). Fig. 4.22 shows the change of the trigger threshold chronologically.

We introduced dead time during data transfer for Kam-3 to avoid picking up noise. And, to reduce this dead time, the number of read-outs was down-scaled by one eighth. The dead time due to this veto has been continuously measured by two 100 Hz scalars (with and without the veto). The dead time due to this source is about 1.5%. In order not to lose a spallation event happening close in time to a muon, the beginning of the data transfer is delayed by 30 msec after the trigger. A single transfer lasts 10 to 20 msec depending on the data size.

4.7. Background from Radon contamination

4.7.1. General description

It is crucial for solar neutrino observation to reduce low energy background which is dominated by the β decay of ^{214}Bi , being a daughter from ^{222}Rn , contained in the water (the endpoint energy is 3.26 MeV).

^{222}Rn ($T_{1/2} = 3.8$ days) is (i) dissolved into the water from the air (subterranean water gathers radon from the rock, flows near the detector, and finally supplies radon to the air around the detector.), and (ii) produced in the water from the decay of ^{226}Ra and other materials (glass of PMT, stainless steel of support frame and so on). Tron gas (^{220}Rn), the daughter of ^{232}Th , is also a possible background source which can be dissolved in water from materials, or from the air. The decay chains of ^{238}U - ^{226}Ra and ^{232}Th are shown in Fig. 4.23.

Therefore, it is essential to purify the water in order to remove the ^{238}U , ^{226}Ra and ^{232}Th . The water purification system used for the purpose in Kamiokande-II and Kamiokande-III is described in subsection 4.7.2.

It is also important to make the detector air-tight in order to shut out the radon and tron gas, and to supply clean air around the detector. We installed a degasifier system to remove the air and radon gas from the water. We made a radon-free air system in order to supply clean air to the detector and to the water purification system. The radon-free air system is described in subsection 4.7.3.

To know the effect of the radon-free air system, a method of measuring and monitoring the radon contamination is necessary. We adopted two methods for the radon measurement and monitoring systems as described in subsection 4.7.4.

4.7.2. Water purification system

There are two separated water systems. The pure water system supplies, purifies and circulates the water of the inner-tank (the inner-detector, top and bottom anti-counters). The other is a constant flow of the mine water to the barrel anti-counter. The cavity is coated by rubber-asphalt, but water leaks through gaps in the rock at a rate of about 5 tons / hour. Therefore, we supply mine water into the barrel anti-counter through a $5\ \mu\text{m}$ filter at a rate of about 15 tons / hour. It is not essential to keep the anti-water pure for solar neutrino observation.

The water purification system for the inner-tank consists of the following elements as shown in Fig. 4.24:

- (1) $5\text{--}10\ \mu\text{m}$ filter,
- (2) de-ionization system or mixed bed ion-exchanger,
- (3) ion-exchange column to remove uranium (CR-55),
- (4) $1.2\ \mu\text{m}$ filter,
- (5) ultra-violet sterilizer to prevent proliferation of bacteria, and
- (6) $0.6\ \mu\text{m}$ filter.

The water taken from the top of the water tank was pumped back to the bottom of the water tank which induces a flow of water from the bottom to the top. The flow rate of the water was set to 4.5 tons / hour.

The ion-exchanger (CR-55) installed in April 1986 is a chelate resin for selectively removing uranium. Due to this resin, the concentration of uranium in the water was decreased from 0.17 pCi/l (mine water) to 10^{-3} pCi/l by December 1986. The concentration has become low enough that the spontaneous fission of uranium does not affect solar neutrino observation, thus, the ion-exchanger has been bypassed since December 1986.

The de-ionization system operated since September 1986 is also the ion-exchange column but optimized to remove ^{226}Ra as well as the other metal ions. The concentration of ^{226}Ra in the water before the operation of the de-ionization system was 8×10^{-3} pCi/l, and it was reduced to 10^{-4} pCi/l by April 1987, though it is 1.6×10^{-2} pCi/l in the mine water. At the same time, ^{238}U had decreased to 2×10^{-4} pCi/l by April 1987. The de-ionization system is now replaced by a mixed bed ion-exchanger which operates the same way.

Water purification is also effective in making the water transparent (attenuation length is about 60 m in Kamiokande-III), since the impurities, the metal ions such as Fe^{++} , Ni^{++} , and Co^{++} , and organic materials such as bacteria, absorb Cherenkov photons.

The water purification system for Kamiokande-III is essentially the same as that for Kamiokande-II. A minor upgrade was done for the ion-exchanger (radium resin was added), and a powerful degasifier system was installed. The degasifier which remove gas (and radon) from the water will be also effective in eliminating radon gas from the water. The membrane degasifier used in Kamiokande-II was replaced by the powerful vacuum degasifier system which will also be used for Super-Kamiokande [ref 4-16], which can remove 99% of the O_2 gas from the water and 96% of the radon gas. It can circulate water at more than $20 \text{ m}^3 / \text{hour}$.

4.7.3. Radon-free air system

Another procedure for eliminating the radon background is to seal out the air from the water and to supply clean air to the detector and the water purification system. Since radon has a short half life of $T_{1/2} = 3.8$ days, circulation of the water (or not to supply mine water which contains radon gas with 200-400 pCi/l) is the best way to reduce radon in the water. But, it is not sufficient to remove radon in the water, because air around the detector contains radon gas of 25-50 pCi/l and this radon gas can easily be dissolved into the detector water.

In Kamiokande-II, we used charcoal to trap radon. It reduced radon by a factor of 100 for the air in the mine. The radon contamination of the radon-free air was 0.3 pCi/l at the time. The radon-free air was supplied to the top of the detector and to the buffer tanks (see Fig. 4.24), and the concentration of radon in the top of the detector was measured to be 0.2 pCi/l. But the concentration of radon in the water was under the detectable limit of ~ 1 pCi/l (later we are able to measure this level of radon, see the next subsection).

We improved the radon-free air system for Kamiokande-III. We installed cooled charcoal (about -40°C) in the radon-free air line in December 1990, which further reduces radon by a factor of 30. The effect was clearly seen in the low energy event rate (dominated by β -decay of ^{214}Bi) as shown in Fig. 4.25. The decay curve is well described by the half life of radon. The event rate decreased by a factor 3 after the installation of the cooled charcoal. The concentration of radon in the water has

decreased from 0.1 pCi/l to 0.03 pCi/l, which is measured by the new method described in the next subsection. Solar neutrino observation with Kam-3 started after the significant reduction of radon from the installation of the cooled charcoal for radon-free air. The conventional charcoal filter, which can reduce radon by a factor of 100 and was used in Kam-2, was not operated at the time. It was returned to service in September 1991.

We further strengthened the conventional charcoal filter by connecting them in series in June 1992 (radon in the radon-free-air was degraded by another factor of 100). The flow rate was increased from 10 liters / min to about 20 liters / min. Finally, the radon concentration in the radon-free air was less than 10^{-4} pCi/l, which is 3×10^{-5} times less concentrated than the mine air. Due to the improvement of the radon-free air, the concentration of radon in the top of the detector was lowered to about 0.02 pCi/l, which is a 10 times smaller value than that of Kamiokande-II. The radon in the water is finally decreased to about 0.014 pCi/l.

4.7.4. Radon measurement

Although the measurement of radon is essential in evaluating various methods of "removing" radon and in knowing where the radon comes from, it is difficult to measure the radon concentration below 1 pCi/l level. We adopted two different types of radon measurement. The key points for the low level radon measurement are (i) how to condense radon and (ii) how to enhance the signal.

(I) The first method offers a direct measurement of Rn concentration in water. Radon gas in water is extracted through He bubbling and pushed into a scintillation counter cell made of ZnS(Ag), called a Lucas counter. Then the α -decay of ^{222}Rn itself and its daughters are measured. The detailed procedure is explained in the following (schematic diagram is shown in Fig. 4.26):

- (1) sucking in about 20 liters of water by vacuum so as not to mix with the mine air (the measurable limit of the concentration is determined by the volume. About 10^{-3}

pCi/l can be detected with 20 liters of water.) as denoted by the flow line (a) in Fig. 4.26,

- (2) bubbling out the radon gas from the water with He gas (flow rate is 0.75 liters /min, and flow continues for 2 hours.) as denoted by the flow line (b),
- (3) capturing the radon gas ($T_m = -71^\circ\text{C}$, $T_b = -61.9^\circ\text{C}$) with the cold trap (liquid nitrogen temperature; $T_b = 77.35^\circ\text{K} = -195.8^\circ\text{C}$),
- (4) removing CO_2 , H_2O and O_2 by passing through the silica-gel, ascarite (NaOH) and magnesium perchlorate ($\text{Mg}(\text{ClO}_4)_2$) as denoted by the flow line (c) (flow rate is 0.3 liters / min),
- (5) pushing radon gas into the Lucas counter through flow line (d) in Fig. 4.26, whose inside is coated with $\text{ZnS}(\text{Ag})$ scintillator (see Fig. 4.27), with He gas, and
- (6) counting the alpha decay rate coming from ^{222}Rn and its daughters, ^{218}Po and ^{214}Po . The ZnS layer is so thin that only alpha radiation is seen (this means less background in the measurement).

The detection efficiency of radon gas is calibrated by the measurement of the mine water which contains a known amount of radon. Fig. 4.28 shows the energy spectrum of the alpha counting. Since the energy resolution of the Lucas cell is not good, we can not distinguish the origins of the α -emission. But the resolution is sufficient to count up the alpha particles ($N_{\text{all}} \approx 3N_{\text{radon}}$) with sufficiently high efficiency. Fig. 4.29 shows the decay curve in time for the mine water calibration and for the measurement of the detector water. We can see the good signal to noise ratio. We obtained the detection efficiency (including the collection efficiency) of radon to be 77% and the radon concentration was found to be 0.1 pCi/l for this measurement. This measurement was done in November 1990 before the installation of the cooled charcoal. The radon concentration after the installation has been measured to be 0.03 pCi/l with the same procedure. Fig. 4.30 shows the rise time measurement right after the injection of the radon gas into the Lucas cell, and the drop of the curve is the time after removing the radon gas (but leaving the daughter nuclei) from the counter, respectively. These curves

are well described by the expectation based on the half lives of the nuclei in the decay chain.

We can estimate that how much of the remaining background in the final data sample is due to radon by considering the correlation between radon concentration and event rate in the final data sample before and after the installation of the cooled charcoal. We observed a factor of three reduction (0.1 pCi/l \rightarrow 0.03 pCi/l) of radon gas in the water, while the event rate above 7 MeV decreased by only a factor of two. Therefore, we can estimate that half of the background above 7 MeV is originated by radon gas, at the radon contamination level in the water, 0.03 pCi/l.

(II) The second method uses a solid state detector (SSD). The detector is schematically drawn in Fig. 4.31. The detection principle is described below:

- (1) The positively charged ions (^{218}Po , ^{214}Pb , ^{214}Bi or ^{214}Po), the daughters of ^{222}Rn , are collected onto the PIN photo-diode by an applied electric field (60~100 V / 7~10 cm). The collection efficiency is about 10~20% which depends on the humidity, the strength of the electric field and the shape of the detector.
- (2) Half (solid angle is 2π) of the decay from ^{218}Po and/or ^{214}Po is measured by the PIN photo-diode with sufficient energy resolution to distinguish the original nucleus (see Fig. 4.32). The detector is almost background free due to the good energy resolution.

The advantage of this detector is that the detector can be exposed for a long time. Because it is background free, the statistics increase with the square root of the exposure time. If we take the practical exposure time as less than one month, the detector can measure the radon concentration in the air down to about 10^{-3} pCi/l. It is also an advantage of the method that the detector is almost maintenance free, therefore, it can be used for continuous monitoring of the radon concentration. This feature is ideal for looking for leaks of radon gas and is suited to monitoring for accidents in the radon free air system. The disadvantage of the detector is that it cannot follow quick changes of the radon concentration at such a low level ($\sim 10^{-3}$ pCi/l).

This detector can also measure the radon concentration in the water by use of a membrane which passes radon gas but not water. There is a relation between the radon concentration in the air and that in the water, if we assume equilibrium, depending on the temperature. The coefficient for 11°C water (the temperature of the water in the Kamiokande detector is 11°C) is about 3; $\rho(\text{Rn})_{\text{air}} \sim 3 \times \rho(\text{Rn})_{\text{water}}$. Lowering the detector (shown in Fig. 4.33) into the water, the radon concentration in the water has been measured to be about 0.014 pCi/l, in January 1993. The collection efficiency of radon is also calibrated by the measurement of the mine water.

References

- [4-1] K. Arisaka et al., J.Phys.Soc.Jpn. **55**(1985)3213; K. Arisaka, Ph.D.thesis, Fac.of Science, Univ.of Tokyo (1985), UT-ICEPP-85-01.
- [4-2] T.Kajita et al., J.Phys.Soc.Jpn. **55**(1986)711; T.Kajita, Ph.D.thesis, Fac.of Science, Univ.of Tokyo (1986), UT-ICEPP-86-03.
- [4-3] M.Nakahata, Ph.D.thesis, Fac.of Science, Univ.of Tokyo (1988), UT-ICEPP-88-01.
- [4-4] K.Hirata et al., Phys.Rev.Lett. **58**(1987)1490; K.S.Hirata et al., Phys.Rev. **D38**(1988)448.
- [4-5] K.Kihara, Ph.D. thesis, Univ. of Tokyo (1992), ICRR-Report-274-92-12.
- [4-6] T.Ishida, Master thesis, Univ.of Tokyo (1992), ICRR-Report-277-92-15.
- [4-7] I.Frank and I.Tamm, C.R.Acad.Sci.USSR **14**(1937)109.
- [4-8] W.C.Haxton, NIM **A264**(1988)37.
- [4-9] For example see E.D.Commins and P.H.Bucksbaum, Weak Interactions of Leptons and Photons, (Cambridge University Press, 1983).
- [4-10] If we take into account a radiative correction according to;
- $$g_V = \rho_{\nu_e} \left(-\frac{1}{2} + \kappa_{\nu_e} \sin^2 \theta_W \right) \text{ and } g_A = \rho_{\nu_e} \left(-\frac{1}{2} \right),$$
- one [ref 2-3] obtains $\rho_{\nu_e} = 1.0072$ to 1.0172 and $\kappa_{\nu_e} = 1.0044$ to 1.0524 for $\nu = \nu_{\mu}(\tau)$, respectively, where the value depends on the top quark mass and the former value of the range is for $m_t = 100$ GeV and the latter is for $m_t = 200$ GeV. Hence g_V and g_A vary from -0.035 to -0.039 and from -0.504 to -0.509 , respectively. The listed values of A_0 , B_0 , C_0 in the text are obtained from the central value of above numbers.
- [4-11] R.E.Carter, F.Reines, J.J.Wagner and M.E.Wyman, Phys.Rev. **113**(1959)280.

- [4-12] Kubodera, private communication.
- [4-13] A.Suzuki et al., NIM **A329**(1993)299.
- [4-14] made by Toshiba Co., Japan
- [4-15] T.Tanimori, H.Ikeda, M.Mori, K.Kihara, H.Kitagawa and Y.Haren, IEEE Trans.Nucl.Sci. **NS-36**(1989)497.
- [4-16] Y.Totsuka, ICRR-Report-227-90-20, 1990, ICRR University of Tokyo.

The present study was designed to investigate the effects of a 12-week training program on the performance of young adults. The participants were divided into two groups: an experimental group and a control group. The experimental group received a structured training program, while the control group did not. The results showed that the experimental group significantly outperformed the control group in all measures of performance.

Introduction

The purpose of this study was to examine the effects of a 12-week training program on the performance of young adults. The study was designed to investigate the effects of a structured training program on the performance of young adults. The participants were divided into two groups: an experimental group and a control group. The experimental group received a structured training program, while the control group did not. The results showed that the experimental group significantly outperformed the control group in all measures of performance.

5. Data analysis

The data were analyzed using a two-way analysis of variance (ANOVA) with training condition (experimental vs. control) and time point (pre-test vs. post-test) as independent variables. The dependent variables were the various performance measures. The results showed a significant interaction effect between training condition and time point, indicating that the experimental group showed a significant improvement in performance over time, while the control group did not. The post-hoc analyses revealed that the experimental group significantly outperformed the control group at the post-test time point across all measures of performance.

5. Data analysis

We have accumulated 1557 days of data from January 1987 to February 1993. There are four types of data related to the gain doubling of the PMTs, attachment of the light reflectors and efforts to eliminate the radon background. The four data sets are hereafter called "Kam-2 gain \times 1", "Kam-2 gain \times 2", "Kam-3 7.5 MeV" and "Kam-3 7.0 MeV", respectively. The data taking period of "Kam-2 gain \times 1" was from January 1987 to May 1988 and the average gain of the PMTs was set at 3×10^6 . The energy threshold for the analysis was 9.3 MeV. In "Kam-2 gain \times 2", lasting from June 1988 to April 1990, the average gain of PMTs was 6×10^6 , which increased the detection efficiency of a one photo-electron signal. Due to the high gain, the effective number of hit PMTs for a 10 MeV electron increased from 25.9 to 29.9, and the energy resolution improved. Some improvements were performed for air-tightening and for an air-cleaning system in order to prevent radon gas from dissolving in the detector water. As a result, we were able to lower the analysis threshold to 7.5 MeV. After some improvements from Kamiokande-2, solar neutrino observation entered new phase: Kamiokande-3 in December 1990. While the gain of PMTs remained 6×10^6 , the effective number of hit PMTs for a 10 MeV electron increased to 40.0 due to increased light coverage. A larger number of hit PMTs per unit energy had not caused a drastic decrease in radon background and the analysis threshold was still set at 7.5 MeV at the beginning of Kamiokande-3. Due to the improvement of the radon-free-air system, the concentration of radon in the detector water is now 10 times less than that at the beginning of Kamiokande-3. This made it possible to lower the analysis threshold to 7.0 MeV after November 1991.

We first explain the event reconstruction methods (section 5.1) and then describe M.C. simulation (section 5.2). Event reduction and the consideration of background is given in section 5.3.

5.1. Event reconstruction

The reconstruction of the event vertex, direction and energy is conducted using the time, pulse height and pattern information. The vertex is principally reconstructed from the relative timing of each hit PMT for fast vertex reconstruction, but the pattern information is additionally used for precise vertex reconstruction. The direction is reconstructed by considering the Cherenkov ring pattern. Energy reconstruction for low energy events are separately developed. Muon track reconstruction is used to identify subsequent spallation events.

5.1.1. Fast vertex reconstruction

We needed a fast vertex reconstruction program for a pre-reduction because the precise vertex reconstruction program (subsection 5.1.2) spends much CPU time and there was a huge amount of data to be analyzed (1~3 Hz). The result of the fast reconstruction is used to reduce the number of events and only the resultant events were subjected to the precise vertex reconstruction described.

The path length of an electron or a positron resulting from a solar neutrino interaction is less than 10 cm. The spread of the region where Cherenkov photons are emitted is negligible in comparison with the vertex resolution of about 1 m. Therefore, we treated the vertex as a point in our vertex reconstruction program.

Supposing we find the true vertex,

$$T^2 = \sum_{i=1}^{N_{\text{hit}}} t_{\text{res},i}^2 \quad (\text{eq 5-1})$$

becomes the minimum under the assumptions that the effects of timing resolution and diffuse photons from scattering and reflection do not have a large effect, where N_{hit} is number of hit PMTs and $t_{\text{res},i}$ is the residual time for i -th hit PMT defined by

$$t_{\text{res},i} = t_i - \frac{n}{c} \times |\mathbf{r} - \mathbf{r}_i| - \langle t \rangle, \quad (\text{eq 5-2})$$

where t_i is the relative time of the hit-signal on i -th PMT corrected for its pulse height, n the refractive index of water, c the speed of light, \mathbf{r} the vertex position, \mathbf{r}_i the position of i -th PMT, and $\langle t \rangle$ the average time defined by

$$\langle t \rangle = \frac{1}{N_{\text{hit}}} \sum_{i=1}^{N_{\text{hit}}} \left(t_i - \frac{n}{c} \times |\mathbf{r} - \mathbf{r}_i| \right). \quad (\text{eq 5-3})$$

The principle of the vertex reconstruction is to minimize the equation (eq 5-1) by varying a vertex point.

We used the following measure of fitness (goodness) for the vertex search,

$$\text{goodness} = \frac{1}{\sum_i \alpha_i^2} \times \sum_i \frac{1}{\alpha_i^2} \exp \left[-\frac{t_{\text{res},i}^2}{2(\langle \alpha \rangle C)^2} \right], \quad (\text{eq 5-4})$$

where α_i is the timing resolution of i -th PMT as a function of its pulse height, $\langle \alpha \rangle$ the average of α_i , $C = 1.5$ the cut off parameter (which means that we used a $\sqrt{2} \langle \alpha \rangle C = 2\sigma$ region of the spread of hit times for the vertex reconstruction) which was chosen to increase the contribution of hit signals but to diminish the effect of dark current and scattered light. The "goodness" ranges 0 to 1 and the maximum value is obtained when T^2 became 0.

We used a grid search technique to search for the point where goodness becomes maximum. The grid size was chosen to be $2/2.2^n$ meter ($n=0$ to 3), and the minimum size was set to 19 cm. The calculation speed for the fast reconstruction method was about 0.03 sec / event by FACOM M780. The vertex resolution obtained by the fast reconstruction method is about 1.5 m for a 10 MeV electron.

5.1.2. Precise vertex reconstruction

Since the vertex resolution of the fast method was not satisfactory for the physics analysis, a precise vertex reconstruction method utilizing Cherenkov pattern information was invented. Now, the "goodness" is a sum of 2 terms;

$$\text{goodness} = G_{\text{timing}} + G_{\text{pattern}}, \quad (\text{eq 5-5})$$

where G_{timing} is a measure for the timing fit, and G_{pattern} for the pattern fit.

The measure G_{pattern} is determined by the following considerations:

First, the crude direction of the charged particle \mathbf{n} can be obtained simply by the pulse height weighted vector sum,

$$\mathbf{n} = \sum_i Q_i \mathbf{n}_i, \quad (\text{eq 5-6})$$

where Q_i is the pulse height of the i -th hit PMT, and \mathbf{n}_i the direction of the PMT from the vertex. For the ideal Cherenkov pattern in the water, we can expect the following relation;

$$(\mathbf{n}, \mathbf{n}_i) = \cos 42^\circ = 0.74. \quad (\text{eq 5-7})$$

This is the basis for the utilization of the Cherenkov pattern information. A Monte Carlo simulation of 10 MeV electrons was used to estimate an effect from multiple scattering, light attenuation, acceptance of the photo-cathode and so on, yielding the value of 0.62. This number was adopted in G_{pattern} as the following expression,

$$G_{\text{pattern}} = - \frac{\left(\frac{1}{N_{\text{hit}}} \sum_i (\mathbf{n}, \mathbf{n}_i) - 0.62 \right)^2}{\sigma_a^2} \times \text{weight} \times \frac{1}{N_{\text{hit}}}, \quad (\text{eq 5-8})$$

where σ_a is one standard deviation of $(\mathbf{n}, \mathbf{n}_i)$ which is also determined by the Monte Carlo simulation and is asymmetric around the mean value,

$$\begin{aligned} \sigma_a &= 0.12 && \text{for } (\mathbf{n}, \mathbf{n}_i) \geq 0.62 \\ &= 0.15 && \text{for } (\mathbf{n}, \mathbf{n}_i) < 0.62. \end{aligned}$$

The parameter "weight" determines the relative contribution of G_{pattern} to the "goodness" being optimized to obtain the best vertex resolution,

$$\text{weight} = 0.9.$$

The measure G_{timing} is modified for the precise reconstruction by considering the diffuse light (scattered or reflected). The hit PMTs in the forward hemisphere with respect to \mathbf{n} (eq 5-6) will be dominated by hits of direct Cherenkov light from the particles, but the PMTs in the backward hemisphere have a contribution of hits by the diffuse light. Hence, a different measure was adopted. The measure (eq 5-4) is for the PMTs in the forward hemisphere (and for the PMTs for which $t_{\text{res},i} < 0$), but, for the backward PMTs (for which $t_{\text{res},i} \geq 0$), we used the measure,

$$\max \left\{ \exp \left[- \frac{t_{\text{res},i}^2}{2(\langle \sigma \rangle C)^2} \right], 0.8 \times \exp \left[- \frac{t_{\text{res},i}}{20 \text{ nsec}} \right] \right\}, \quad (\text{eq 5-9})$$

for the exponential part of (eq 5-4). The second term in (eq 5-9) is obtained from the Monte Carlo study for diffuse light, which resulted in a 20 nsec degrading time for the diffuse light and the factor 0.8 is chosen to obtain the optimum vertex resolution.

The minimum grid size for the vertex search in this precise reconstruction is 13 cm. This reconstruction works with the speed of 0.1 sec / event on FACOM M780. The vertex resolution obtained by precise reconstruction is 1.0 m for a 10 MeV electron (see Fig. 4.13). The difference of the vertex position between fast and precise vertex reconstruction is shown in Fig. 5.1. The difference does not show any systematic effect between the fast and the precise reconstruction programs (the difference does not exceed the vertex resolution).

5.1.3. Direction reconstruction

The directional measurement of solar neutrinos is a big advantage of the Kamiokande experiment. This measurement is based on the strong directionality of the recoil electron from νe^- elastic scattering and the nature of Cherenkov photon radiation as described in section 4.2. The crude direction obtained by (eq 5-6) was improved for the solar neutrino analysis.

A maximum likelihood method was adopted for the advanced directional reconstruction using the Cherenkov ring pattern. We obtained a distribution of the opening angle $f(\theta)$ as shown in Fig. 5.2 from a Monte Carlo study of 10 MeV electrons, where θ is the angle between the trajectory of the charged particle and the direction from the vertex to the hit PMT. The best direction \mathbf{d} was obtained by maximizing the likelihood function,

$$L(\mathbf{d}) = \prod_i f(\theta_i), \quad (\text{eq 5-10})$$

by the grid search technique with step sizes of 20° , 9° , 4° and 1.6° . The angular resolution for 10 MeV electrons is now 27° (see also Fig. 4.14) which is mostly limited by multiple scattering.

5.1.4. Energy reconstruction

As described in section 4.2, we used the number of hit PMTs (N_{hit}) for energy measurement instead of the total number of photo-electrons. A hit-PMT catches mostly one photon in the low energy event around 10 MeV: the number of hit PMTs and the total number of photo-electrons are almost same.

The number of hit PMTs, N_{hit} , was obtained by following procedure:

- The vertex position was determined as described in subsection 5.1.1 and 5.1.2.
- A time of flight (propagation time of Cherenkov photon from the vertex to a hit PMT) is subtracted from all timing information.
- A maximum number of hit PMTs (N_{hit}) is searched within a 40 nsec time window.

When we count the number of hit PMTs, we used ones with more than $-0.25(\text{Kam-2})$ or $-4.0(\text{Kam-3})$ photo-electrons; one photo-electron is sometimes measured as a negative pulse because of finite pulse height resolution. The width of 40 nsec was chosen to reduce dark current or accidental noise. As mentioned in section 4.6, this gate width suppresses the dark current to about 0.1 counts per event in the Kam-3 case.

We made several corrections to N_{hit} in order to get an effective energy scale (number of effective hit PMTs or N_{eff}). The following corrections are made in the Kamiokande-II analysis:

- (1) water transparency,
- (2) PMT gain,
- (3) PMT density,
- (4) acceptance of the photo-cathode,
- (5) number of dead PMTs.

The formula of the N_{eff} is defined by

$$N_{\text{eff}} = \frac{948 - N_0}{948 - N_{\text{dead}}} \frac{1}{\text{gain}} \sum_i \exp\left(\frac{r_i}{l_m}\right) \exp\left(-\frac{R}{L_{\text{abs}}}\right) \frac{\cos \theta_i}{f(\theta_i)} \frac{1.06}{\rho_{\text{wall}}}, \quad (\text{eq 5-11})$$

where N_0 is the number of dead PMTs at a fixed time, N_{dead} the number of dead PMTs at the observation time, "gain" the relative PMT gain, r_i the distance from the vertex to the PMT, l_m the measured light attenuation length in the water, R and L_{abs} the constants 7.22 m and 35.0 m (they are meaningless and historical in nature.), θ_i the opening angle between the direction of the photon and the direction PMT $_i$ is facing, $f(\theta)$ the acceptance of the photo-cathode viewed from the direction θ_i (see Fig. 5.3), ρ_{wall} the relative density of PMTs, $\rho_{\text{wall}} = 1 \text{ PMT} / 0.945 \text{ m}^2 = 1.06$ for the barrel PMTs, and $\rho_{\text{wall}} = 1 \text{ PMT} / 1 \text{ m}^2 = 1$ for the top and bottom PMTs.

In the Kamiokande-III analysis, corrections are much more simple. We adopted only (3), (4) and (5) for the correction. The reasons are the following:

- The water transparency is good and stable (about 60 m) in Kam-3. Therefore, correction (1) is not essential.
- Correction (1) increases the effective hit when the vertex is far from the hit PMT. But, this correction has a reverse effect in Kam-3 because the improved photo-coverage by the light reflectors increased the probability that the PMT catches more than one photo-electron. As the vertex gets closer to a PMT, this probability increases noticeably. We then should not decrease the effective hit for the PMT close to the vertex by correction (1).
- The gain is so stable in Kam-3 that correction (2) is not necessary now.

The N_{eff} for Kam-3 is defined by

$$N_{\text{eff}} = \frac{948 - N_0}{948 - N_{\text{dead}}} \sum_i \frac{\cos \theta_i}{f(\theta_i)} \frac{1.06}{\rho_{\text{wall}}}, \quad (\text{eq 5-12})$$

where $f(\theta)$ is modified to include the effect of the light reflector as shown in Fig. 5.3.

The coefficients for converting N_{eff} to energy (MeV) were obtained by the detector simulator (see subsection 5.2.3), in which electrons with total energy 10 MeV are generated. These factors are,

$$E_e = \frac{1}{2.59} N_{\text{eff}} \quad (\text{Kam-2 gain} \times 1), \quad (\text{eq 5-13})$$

$$E_e = \frac{1}{2.99} N_{\text{eff}} \quad (\text{Kam-2 gain} \times 2), \text{ and} \quad (\text{eq 5-14})$$

$$E_c = \frac{1}{4.00} N_{\text{eff}} \quad (\text{Kam-3}) \quad (\text{eq 5-15})$$

This linear relation is guaranteed in an energy region above around 5 MeV up to about 20 MeV. The linearity does not remain for high energy events because the number of hit PMTs is not same as the number of photo-electrons; one PMT catches more than one photon. Kam-3 has a larger photo-coverage, and the effect of multi-photons appears at a relatively lower energy than Kam-2. The linear relation is valid up to about 15 MeV in Kam-3. The relation between energy and N_{eff} is shown in Fig. 5.4. The small non-linearity is a well-understood property and is well taken care of in the Monte Carlo simulation. Therefore, the physics result is not affected when we obtain the result by comparison between the observed data and the detector simulation.

5.1.5. Muon track reconstruction

Muon track information is used to reject spallation products as described in subsection 5.3.3. Penetrating muons and stopping muons are reconstructed by different algorithms.

(1) For penetrating muons

(a) The entry point is crudely determined by the fast vertex reconstruction method described in subsection 5.1.1 under the assumption that the point must be on the PMT plane, and its direction is obtained by (eq 5-6).

(b) The entry point is then precisely tuned from the timing information of the selected PMTs which are thought to be hit by the photons emitted from the first one third of the muon track (see Fig. 5.5). The time of flight (TOF) is modified due to the finite muon path length;

$$\text{TOF} = \frac{nL}{c} \cos(\theta - \theta_c), \quad (\text{eq 5-16})$$

where n is the refractive index of water, c the speed of light, L the distance from the entry point to the hit PMT, θ the angle between the muon track and the

direction from the entry point to the hit PMT and θ_c the Cherenkov angle given by (eq 4-2).

(c) The exit point of the muon is determined from the timing information of the part of the hit-PMTs which are expected to be hit by the photons emitted from the last half of the muon track (see Fig. 5.5). The modified TOF is also considered.

(d) The steps (b) and (c) are repeated three times because the reconstruction (b) and (c) influence each other through their initial values of entry point and direction.

(2) For stopping muons

(a) The entry point $\mathbf{r}_{\text{entry}}$ and the direction \mathbf{n} are determined the same way as for penetrating muons.

(b) The momentum is calculated using the number of total photo-electrons in a 70° cone.

(c) The stopping point \mathbf{r}_{stop} is determined by the range R which is calculated from the momentum;

$$\mathbf{r}_{\text{stop}} = R \times \mathbf{n} + \mathbf{r}_{\text{entry}}.$$

5.2 Detector simulation

When we derive the solar neutrino flux or the limit on the anti-neutrino flux from the experimental data, we must have complete knowledge of what kind of neutrino interactions take place in Kamiokande (section 4.3), how electrons or positrons behave in the detector (subsection 5.2.1), how Cherenkov photons propagate in the detector (section 4.2 and subsection 5.2.2), and how Kamiokande detects the Cherenkov photons (subsection 5.2.2). But these responses are too complicated to calculate analytically. Hence, a detailed detector simulation is needed. The "what" and "how" of this simulation are described in the denoted section or subsection. The tuning of the simulation parameters (energy response, timing response and so on) and the reliability of the simulation are described in subsection 5.2.3.

5.2.1. Particle transport

The electrons or positrons generated by neutrino interactions are traced through the detector water by the Electron-Gamma-Shower code version 4 (EGS4) [ref 5-1], which can simulate all important physics processes involving electrons and photons with energies above a few keV up to TeV. The physics processes treated in EGS4 are bremsstrahlung, pair annihilation, multiple Coulomb scattering, Møller (e^-e^-) and Bhabha (e^+e^-) scattering, continuous energy loss by particle tracks, pair production, Compton scattering, coherent Rayleigh scattering, and the photoelectric effect.

Fig. 5.6 shows twenty overlaid electron tracks in water with the kinetic energy of 10 MeV. We can see that the electrons do not make any hard electromagnetic showers. This is because the radiation length in water, 36.1 cm, is much longer than the track length of the electrons (about 4 cm). We can also see that these tracks are strongly bent by multiple Coulomb scattering which limits the angular resolution of electrons.

5.2.2. Cherenkov photon propagation

If the velocity of a charged particle exceeds the speed of light in matter, the particle emits Cherenkov photons as described in section 4.2. The Cherenkov photons are emitted in the direction given by formula (eq 2-2) from the tracks generated by the EGS4 code. The number of photons is determined by formula (eq 2-3). Then, these photons are traced until they are caught by a PMT or absorbed by something.

For Cherenkov photon propagation, we use the light attenuation curve as shown in Fig. C.11 for Kam-3. The curve corresponds to an attenuation length of 55m on the average. The measured attenuation length is long and stable between 50 m and 60 m. At the beginning of Kam-2, the measured attenuation length was about 30 m and not stable in time. Therefore a different curve was used for Kam-2.

Once the Cherenkov photon reaches the PMT plane, the reflection at the detector wall, 10% (measured), the reflection of the light reflector, 80%, and photon absorption by the magnetic mesh shield covering the PMT cathode, 13% (measured),

are considered. The quantum efficiency of the photo-cathode was taken into account with the wave length dependence shown in Fig. A.2.

Then, if the conversion occurred, the pulse height and timing resolution are simulated as a function of the number of photons converted. The data from the Ni-Cf calibration was used to get the pulse height distribution for one photo-electron, since the number of Cherenkov photons emitted in the calibration is so small that a hit PMT is guaranteed to have only one photo-electron. The measured pulse height distribution is shown in Fig. 5.7. The timing resolution is measured by laser calibration as described in appendix C.2. We parametrized the measured distribution by using the gaussian distribution. These parameters are corrected by a small amount to reproduce the vertex resolution precisely as described in section 5.2.3. In Kam-3, we further considered the dark current of a PMT which increases the number of hit PMTs by about 4 hits in the TDC full range of 1 μ sec and results in a small distortion of a Cherenkov pattern. The effect appears as a 0.5 % shift of the energy at 10 MeV with the energy measured as described in subsection 5.1.4. This small change is considered in the absolute energy scale determination described in appendix C.1. The systematic error of $\pm 2.3\%$ is larger than this effect of 0.5%.

5.2.3. Tuning of the detector simulation

It is difficult to follow completely all the detailed processes without missing any and to put them into the simulation. We have made a detailed comparison of the essential quantities, such as the energy and the vertex resolution with real data to see if the M.C. reproduces those physics properties. The calibration by Ni-Cf source is essential for low energy phenomena in Kamiokande, since its energy range is near that of solar neutrinos. This calibration gives not only the standard of the absolute energy but also the basis for studying the vertex resolutions. Therefore the Monte Carlo simulation was compared and tuned in detail with the data of this calibration.

As described in subsection 5.1.4, the number of hit PMTs is an estimator of the energy. The number of hit PMTs depends on the trigger threshold of each channel (i.e. ~ 0.2 p.e. mentioned in section 4.6), but this is not exactly known. The quantum

efficiency of the photo-cathode is also not known in detail. Hence, we introduced a sort of gain parameter which reflects both the trigger efficiency of each channel for a one photon signal and the quantum efficiency. This parameter was determined to reproduce the peak number of hits of the $Ni(n,\gamma)Ni'$ calibration. The simulated and the observed spectra of gamma rays from the $Ni(n,\gamma)Ni'$ reaction are shown in Fig. C.5. The width of the distribution is well reproduced while we only adjusted the peak value (this is not trivial because the width is not determined only by the statistics from the number of hit PMTs). We have also checked the consistency of the detector simulation by using the same calibration but taken at different locations such as at the edge of the fiducial volume. The "thus adjusted" detector simulator at the center can reproduce the energy spectrum of the calibration at the edge of the fiducial volume within a 1% accuracy.

The vertex resolution is essential in obtaining the efficiency of the fiducial volume cut (subsection 5.3.2). The vertex resolution is mainly influenced by the timing resolution of the PMTs. The tuning of the vertex distribution was done in the following way. The timing resolution measured with the laser calibration (appendix C.2) is parametrized by a gaussian distribution as a function of pulse height as shown in Fig. 4.11. If we use this distribution the vertex resolution of the simulation should reproduce real data. However, the real data sometimes contains anomalous data due to a noisy PMT or a fake signal of the electronics module, which makes the vertex resolution worse. If we use the anomalous data which has abnormally large light output, the vertex point tends to be reconstructed close to the PMT. The implementation of these noises would make the detector simulator unreliable because a perfect simulation is not easy. Therefore, we modified the vertex reconstruction program described in subsection 5.1.1 and 5.1.2 not to be affected by the fake signal and further tuned the M.C. program. We have rejected any large output signal greater than 10 photo-electrons in the fitting. The timing resolution of higher p.e. hits used in the M.C. simulation were made slightly worse, therefore decreasing the weight of these fake signals; the timing resolution is used for the weight of the signal as seen in

(eq 5-4). Such tuning improved the vertex resolution of the real data and degraded that of the simulation. The agreement between them is now satisfactory as shown in Fig. 5.8. The vertex distribution for the Ni+Cf data as a consequence are well reproduced both at the center of the detector and at the edge of the fiducial volume as shown in Fig. 5.9.

5.3. Data reduction and Background

The trigger rate varied during the experiments: it ranged from 0.5 Hz to 4 Hz depending on the trigger condition, the background and so on. We know the following background sources:

- Cosmic ray muons penetrating 1 km of rock,
- Radioactive impurities in the water, especially ^{214}Bi beta decay with end point energy of 3.26 MeV originating from ^{222}Rn ,
- Cosmic ray induced spallation products,
- Gamma rays from the rock surrounding the detector,
- Electronics noise or flash tubes, and
- Neutrinos from reactors, the atmosphere, supernova ... and so on.

Those backgrounds were reduced by the following steps.

- (1) Muon reduction (subsection 5.3.1): muons, electric noise events, radon events
- (2) Fiducial cut (subsection 5.3.2): flash tubes, noise, gamma rays from the rock
- (3) Spallation cut (subsection 5.3.3): spallation products
- (4) Gamma ray cut (subsection 5.3.4): gamma rays from the rock

We will describe these reduction steps adopted in the Kamiokande-III analysis in the following subsections. They were basically same for the Kamiokande-II analysis. The difference, if they exist, are mentioned where appropriate.

SSM_{BP92} was used as the standard solar model in calculating the expected rate. The detection efficiencies of each cut and the systematic errors are detailed in section 6.2.

First of all, the interaction rate of ^8B solar neutrinos ($5.69 \times 10^6 / \text{cm}^2 / \text{sec}$) in the 2142 tons of photo-sensitive region is 21.4 events / day; the expected rate of events which exceed the trigger threshold (~ 5 MeV) is about 7 events / day / 2142 tons. The event rate in the raw data is 0.5 Hz to 4 Hz (~ 70000 events / day in average), therefore, the signal to noise ratio is roughly 10^{-4} in the raw data.

5.3.1. Muon reduction

In this step, we mainly reject cosmic ray muons and noise events.

The Kamiokande detector is covered by thick rock (about 1 km), and therefore the cosmic ray muon flux is reduced by $\sim 10^{-5}$. However, the muon still remains as a major background in the Kamiokande experiment. The trigger rate is kept around 1 Hz throughout the experiment, out of which muons occupy 0.37 Hz. The rest is estimated to be shared by radon background and gamma rays from the surrounding rock. The pulse height distributions of the muons for inner and anti counters are shown in Fig. 5.10. It is easy to reject those muons by requiring no hits in the anti-PMTs because they must penetrate the anti counter. The applied cut was

$$\begin{array}{ll} \text{Anti total p.e.} < 30 \text{ p.e.} & (\text{Kam-2}), \\ < 50 \text{ p.e.} & (\text{Kam-3}). \end{array}$$

We also applied a total pulse height cut to the inner detector,

$$\begin{array}{ll} \text{Inner total p.e.} < 100 \text{ p.e.} & (\text{Kam-2}), \\ < 500 \text{ p.e.} & (\text{Kam-3}). \end{array}$$

The total photo-electron cut has a risk that interesting events may be rejected by the cut because noisy PMTs or electronics sometimes adds a large pulse height to an event. Hence, we loosened this cut in the Kam-3 analysis. Such fake hits, however, do not affect the subsequent analysis based on the number of hit PMTs instead of pulse height.

A cut on the time difference to the previous event,

$$\begin{array}{ll} \Delta T \geq 100 \mu\text{sec} & (\text{Kam-2}), \\ \geq 20 \mu\text{sec} & (\text{Kam-3}), \end{array}$$

was used to reject the time correlated backgrounds: electrons from μ -e decay and the ringing which is often caused by large pulse height muons. In Kam-3, the ringing noise sometimes lasts up to about 15 μsec . Hence, 20 μsec cut is needed to reject the ringing and is also sufficient to reject a μ -e decay (~ 9 times the muon life time of 2.2 μsec). The spallation cut described in subsection 5.3.3 will further eliminate decay electrons that escaped the time-difference cut.

The number of noisy PMTs and the dead PMTs vary in time, so the trigger threshold is not stable at the few % level. Hence, we set the trigger threshold sufficiently lower than the analysis threshold of the solar neutrino events. The trigger threshold of 7.6 (Kam-2 gain \times 1), 6.7 or 6.1 (Kam-2 gain \times 2), and 5 MeV (Kam-3) as described in subsection 4.6.2 can be compared to the analysis threshold of 9.3 (Kam-2 gain \times 1), 7.5 (Kam-2 gain \times 2), and 7.5 or 7.0 MeV (Kam-3). Therefore, the variation does not affect the physics analysis. The minimum energy-like cut of

$$C_{\text{dead}} \times N_{250} \geq 23,$$

which corresponds to about 6 MeV was applied at this step (C_{dead} is the correction factor for the number of hit PMTs described in appendix C.5 and N_{250} is the number of hit PMTs in a 250 nsec window). N_{250} was used because N_{hit} and N_{eff} (see subsection 5.1.4) can only be determined after the event reconstruction. The full range of the TDC was 1.1 μsec in Kam-3, while it was 400 nsec in Kam-2. Such a wide gate contains dark current signal (about 4 hits per event) and the crude requirement of a 250 nsec gate is very useful in making N_{250} a good measure of the energy even before the correction for the time of flight (the maximum correction of the time of flight is 87 nsec). This cut reduces the number of events to be analyzed by a factor of three.

After this reduction step, the expected signal is about 5 events / day, and the real event rate is ~ 15000 events / day. The signal to noise ratio is now $\sim 3 \times 10^{-4}$.

5.3.2. Event reconstruction and Fiducial volume cut

The events passing the above reduction step were reconstructed by the fast vertex reconstruction method described in subsection 5.1.1. A typical vertex distribution obtained is shown in Fig. 5.11. Those events which have a vertex closer than 50cm to the wall are removed. Further reduction was made using the quality of the event.

The "goodness" described in subsection 5.1.1 is also useful for rejecting electric noise events with the following characteristics:

- (i) the ratio of the number of hit PMTs to the total number of photo-electrons is larger than that of a normal event,
- (ii) the pulse height of the PMTs often becomes negative,
- (iii) since it does not have a vertex point the "goodness" becomes worse as shown in Fig. 5.12.

We then applied the following cuts to reject these noise events:

$$\text{"goodness"} \geq 0.4,$$

$$N_{\text{hit}} / N_{\text{dsc}} \geq 0.6,$$

$$N_{\text{neg}} / N_{\text{dsc}} < 0.4,$$

where N_{hit} is number of hit PMTs within a 40 nsec time window (TOF is subtracted), N_{neg} the number of hit PMTs with negative pulse height, N_{dsc} the number of hit PMTs within a 1.1 μ sec gate window. Typical distributions of $N_{\text{hit}} / N_{\text{dsc}}$ and $N_{\text{neg}} / N_{\text{dsc}}$ for noisy events are shown in Fig. 5.13. The fraction of noise events was only a few %.

The precise vertex reconstruction described in subsection 5.1.2 was applied to the remaining events. A typical vertex distribution at this step for the events with energy greater than 6 MeV is shown in Fig. 5.14.

The fiducial volume for the final data was set to 680 tons (a cylindrical volume 7.94 m in height and 10.44 m in diameter) both in Kam-2 and in Kam-3, but the volume is 57 cm shifted upward for Kam-3 in order to erase an up down asymmetry in the distance to the PMT. The effect of the slight asymmetry was enhanced in Kam-3 due to the reflective mirrors. The distance from the edge of the fiducial volume to the wall is 2.57 m at the top and the bottom, and 2.00 m at the barrel (Kam-3);

$$\begin{aligned} -3.94 \text{ m} \leq z \leq 4.00 \text{ m}, r \leq 5.22 \text{ m}, & \quad (\text{Kam-2}) \\ -3.37 \text{ m} \leq z \leq 4.57 \text{ m}, r \leq 5.22 \text{ m}, & \quad (\text{Kam-3}) \end{aligned} \quad (\text{eq 5-17})$$

where $r = \sqrt{x^2 + y^2}$ and coordinate axes are defined in Fig. 5.15.

This fiducial volume cut is effective in reducing the events originating from a flash tube which tend to have a vertex close to the PMT, and gamma rays from the rock surrounding the detector. These gamma rays are attenuated (attenuation length in water is ~ 40 cm) by the water in the anti-counter (0.7 m for the top, ~ 1.5 m for the barrel, 1.2 m for the bottom counter), behind the inner-PMTs plane (~ 60 cm), and in the inner detector to the edge of the fiducial volume (2.57 m for the top and the bottom, 2 m for the barrel).

The differential spectrum of the low energy events before and after the fiducial cut is shown in Fig. 5.16. The fiducial cut reduces the events above 7.5 MeV by a factor of 30 while the fiducial mass is reduced only by a factor of $2142 / 680 \sim 3$.

The expected signal rate after the fiducial cut is 0.93 events / day / 680 tons above 7.5 MeV and the observed event rate is 23.3 events / day, so the expected signal to noise ratio is now 0.04.

5.3.3. Spallation cut

There are very energetic muons accompanying cascade showers. These showers and muons break oxygen nuclei in the water and occasionally create "spallation products." There are long life beta emitters in these spallation products. The beta decays from the spallation products are the main background in the 10 MeV region, and they can be rejected by the time difference and vertex distance to the parent muons. We considered two types of parent muons: one is an energetic muon accompanying a cascade shower which will make beta nuclei along the muon track, and the other one is a stopping μ^- sometimes captured by an oxygen nucleus which forms the radioactive ^{16}N nucleus.

- (1) Energetic muons accompanying cascade shower

A list of the candidates of the spallation products with atomic number less than or equal to 16 emitting beta and/or gamma rays of energy greater than 7 MeV is shown in table 5.1. Most of these nuclei have short lives of several milliseconds to several seconds.

Since $Q_{\text{eff}} = 10,000$ p.e. (Q_{eff} is scaled by the factor 1.27 which corresponds to the increased photo-coverage of Kam-3 due to the light reflectors, then the cut on Q_{eff} is effectively the same for Kam-2 and Kam-3) corresponds to about 10 m of track length, a typical penetrating (from the top to the bottom of the detector) muon has 10,000 p.e. A condition such as $Q_{\text{eff}} \geq 20,000$ p.e. selects events with shower association. The distribution of the time difference between the muon (more than 20,000 effective p.e.) and the low energy event (more than 7 MeV) in this step is shown in Fig. 5.17. It clearly shows the creation of short life nuclei in correlation with muon penetration.

We considered a muon with $Q_{\text{eff}} \geq 10,000$ p.e. and $\Delta T \leq 50$ sec between it and the low energy event. Then, we reconstructed these muon tracks (subsection 5.1.5). The light output Q_{eff} , time difference ΔT , and the distance between the low energy events and the muon track ΔL were examined, and the events in the region shown in the Fig. 5.18 were rejected. The region denoted by "1" does not require any vertex correlation, and the region denoted by "2" and "3" requires $\Delta L \leq 3$ m and $\Delta L \leq 2$ m. The distribution of ΔL for the combinations of muons ($Q_{\text{eff}} \geq 20,000$ p.e.) and low energy events (≥ 9 MeV) which occurred within 1 sec of each other is shown in Fig. 5.19. The solid line in Fig. 5.19 shows the distribution for the accidentally coincident events, and hence it is proportional to the random distribution. It shows an apparent clustering of the low energy events along the muon track with respect to the random distribution.

We applied the spallation cuts to the events with an energy greater than 6.5 MeV in a volume of 970 tons including the fiducial volume. The number of rejected events is 29 events / day / 970 tons above 6.5 MeV (20 events / day / 680 tons above 7.5 MeV). If we found a spallation event, we made a veto of 50 sec

duration from the incident muon to reject multiple spallation production effectively (the probability of causing multiple spallation by a single muon is ~14% relative to single spallation production [ref 1-8]).

(2) Stopping muons

In the Kamiokande detector, ~1/100 of muons stop in the detector. The stopping muon rate in the fiducial volume is about 100 ± 7 events / day. Negatively charged muons may be captured by oxygen. The μ^+/μ^- ratio observed in Kamiokande is $1.37 \pm 0.06 \pm 0.01$ [ref 5-2] ($\mu^- / (\mu^- + \mu^+) = 0.42$). The capture rate of μ^- in water is derived from its life time [ref 2-3, 5-3],

$$1 - \frac{\tau_{\text{water}}}{\tau_{\text{vacuum}}} = 1 - \frac{1.7954 \pm 0.0020 \mu\text{sec}}{2.19703 \pm 0.00004 \mu\text{sec}} = 0.183.$$

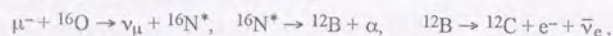
μ^- capture in the fiducial volume, therefore, is $100 \times 0.42 \times 0.183 = 7.7$ events / day, out of which $(11 \pm 1)\%$ form radioactive ^{16}N [ref 5-4] and 70% go to ^{15}N [ref 5-5], being stable. The remaining 19% of the captures are unknown. The rate of ^{16}N formation in the fiducial volume (680 tons), therefore, is 0.8 events / day (or 0.3 events / day above 7.5 MeV) which is a factor of 3 smaller than the expected ^8B solar neutrino signal.

This background can be rejected by looking at the correlation to a stopping muon both in time and in space. To see the correlation, we first selected events which contain a majority of the ^{16}N background by the following algorithm:

- $\Delta T < 30$ sec, (the half life of ^{16}N nuclei is 7.134 sec);
- 110 p.e. < total pulse height < 13,000 p.e. (10 cm < track length < 13 m);
- maximum pulse height in all hit PMTs < 330 p.e. (no exit point);
- time difference from the previous event $\geq 100 \mu\text{sec}$ (ringing event);
- only one penetration (more than 10 p.e. and more than 3 hits) either in the top, bottom and barrel anti-counter;
- (maximum p.e.) / (total p.e.) < 0.3, or (total p.e.) > 400 p.e. (edge clipping muon);

- (anti maximum p.e.) / (barrel anti total p.e.) > 0.5, or (barrel anti total p.e.) < 500 p.e. (barrel to barrel penetrating muon),
- "goodness" for stopping muon reconstruction is greater equal 0.5;
- not accompanied by an event within 20 μ sec with a "goodness" of fast vertex reconstruction greater than 0.4 which could be a decay electron, (decayed muon: no ^{16}N formation)

Then, the correlation in time and in space are examined. Fig. 5.20 shows distributions of the distance from the stopping point of the muon to the vertex of the low energy event ΔL , and the time difference of the muon and the low energy event ΔT . It shows a clear space correlation, and the long component of the decay curve is well described by the half life of ^{16}N , 7.134 sec. The short component seen in Fig. 5.20 is thought to be caused by



where the half life of ^{12}B is 20.4 msec.

We rejected the events with

$$\Delta L < 3 \text{ m, and } \Delta T < 30 \text{ sec.}$$

The dead time caused by the spallation cuts is 13.1% for energetic muons, 0.2% for stopping muons and 1.7% for the 50 sec veto. Total dead time due to the spallation cuts is 15.0%.

Now, the remaining event rate is 7.9 events / day / 680 tons above 7.5 MeV and the expected signal rate is 0.79 events / day. The signal to noise ratio is 0.1.

5.3.4. Gamma ray cut

The event rate close to the wall is apparently larger than that at the center of the detector as shown in Fig. 5.21. The directional distribution of the events close to the wall (a 1 m layer from the edge of the fiducial volume) has an excess in the inward direction as shown in Fig. 5.22, where θ is the angle between the particle trajectory and the direction to the nearest wall. This excess is thought to be caused by gamma

rays from the surrounding rocks. We selectively reject the background in this particular volume by applying,

$$\frac{D_{\text{eff}}}{D_{\text{wall}}} \geq 1.5,$$

where D_{wall} is the distance to the nearest wall and D_{eff} the distance to the wall pointing backward along the event direction.

The loss of detection efficiency due to this cut is 13% from the Monte Carlo study. The differential spectrum before and after this gamma ray cut is shown in Fig. 5.16.

The resulting events make the final sample for the solar neutrino analysis and the event rate is 4.9 events / day. The expected signal rate is 0.685 events / day / 680 tons above 7.5 MeV, and the signal to noise ratio becomes about 0.14.

To summarize, the expected solar neutrino event rate from the SSM_{BP92} and the observed event rate in every reduction step are as follows:

| | observed event rate (events / day) | expected event rate from the SSM (events / day) | estimated signal to noise ratio |
|---------------------|---------------------------------------|---|---------------------------------------|
| Raw data | ~70,000 | 7 | ~10 ⁻⁴ |
| Muon cut | ~15,000 | 5 | ~3×10 ⁻⁴ |
| (7.5 MeV threshold) | 700 | 2.8 | 4×10 ⁻³ |
| Fiducial cut | 23.3 | 0.93 | 0.04 |
| Spallation cut | 7.9 | 0.79 | 0.1 |
| Gamma ray Cut | 4.9 | 0.69 | 0.14 |

5.3.5. Consideration of the remaining background

The remaining background in the final sample is investigated in this subsection. We consider radioactive impurities originating from ^{222}Rn , spallation products, gamma rays from the rock, atmospheric neutrinos and reactor neutrinos.

(1) Radioactive impurities originating from ^{222}Rn

The contribution of ^{222}Rn is estimated using the changes in the event rate and the ^{222}Rn concentration measured by the technique shown in subsection 4.7.4. A decrease of radon gas in the water by a factor of three (from 0.1 pCi/l to 0.03

pCi/l) caused a decrease of the event rate by a factor of two above 7 MeV. We can conclude that a half of the remaining background above 7 MeV is still due to the ^{222}Rn background at the level of 0.03 pCi/l. Recent radon concentration in the water is measured to be 0.014 pCi/l as described in subsection 4.7.4., therefore about 30% of the events above 7 MeV still come from the ^{222}Rn background.

We can see two components in the energy spectrum of the final sample. If we divide the data into 5 time periods as shown in Fig. 5.23, we can see only the soft component below 8 MeV is decreasing in correlation with the radon decrease, and the estimated ratio of radon contribution, 30%, is consistent with the ratio of the soft component.

(2) Spallation products

The reduction efficiency for spallation events was estimated from the time correlation between muons and low energy events with energy of higher than 7 MeV before the spallation cut in the final sample. The decay component (if it exists) in the time difference histogram (Fig. 5.24: time differences for all combinations of low energy events and muons before and after the spallation cut) shows the existence of spallation events. We considered five life times: long 7.13 sec (^{16}N), medium 0.84 sec (^8B) and 0.77 sec (^8Li), and short 11 msec (^{12}B) and 20 msec (^{12}N) half lives. The histograms are made for the different Q_{eff} of the parent muons: $10,000 \leq Q_{\text{eff}} < 20,000$ (12,000 events / day); $20,000 \leq Q_{\text{eff}} < 40,000$ (1,800 events / day); and $40,000 \leq Q_{\text{eff}}$ (270 events / day). The followings are the obtained event rates (events / day) for each spallation product:

| $Q_{\text{eff}} / 10,000$ | ^{12}N | ^{12}B | $^8\text{Li}, ^8\text{B}$ | ^{16}N |
|-----------------------------|-----------------|-----------------|---------------------------|-----------------|
| $1 \leq Q_{\text{eff}} < 2$ | 0.52 ± 0.04 | 0.52 ± 0.04 | 0.66 ± 0.04 | > 0.1 |
| $2 \leq Q_{\text{eff}} < 4$ | 0.68 ± 0.04 | 0.96 ± 0.05 | 1.03 ± 0.05 | 3.24 ± 0.09 |
| $4 \leq Q_{\text{eff}}$ | 1.23 ± 0.06 | 1.87 ± 0.07 | 1.92 ± 0.07 | 4.58 ± 0.11 |

The total event rate from these spallation products is greater than 17.3 events / day / 680 tons above 7 MeV.

The event rate of ^{16}N originating from muons with low p.e. (10,000–20,000) is difficult to extract from the timing correlation, because the average time interval from such muons is not long (~7.2 sec) relative to the long half life (7.13 sec).

Spallation events were reduced by the spallation cuts described in subsection 5.3.3. The total event rate of the remaining spallation events which have timing correlations to muons after the spallation cuts is more than 1.5 events / day / 680 tons above 7 MeV (> 1.3 events / day in the final sample after the gamma cut). It consists of following components:

| $Q_{\text{eff}} / 10,000$ | $^{12}\text{N}, ^{12}\text{B}, ^8\text{Li}, ^8\text{B}$ | ^{16}N |
|-----------------------------|---|-----------------|
| $1 \leq Q_{\text{eff}} < 2$ | — | > 0.07 |
| $2 \leq Q_{\text{eff}} < 4$ | 0.11 ± 0.02 | 0.93 ± 0.05 |
| $4 \leq Q_{\text{eff}}$ | 0.11 ± 0.02 | 0.32 ± 0.03 |

The dead time during data transfer (1.5%) results in missing muons which causes inefficiency in the cuts, and an additional 0.2 events / day remain in the final sample.

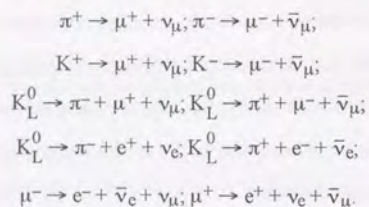
Therefore, we conclude that more than 1.5 events / day of spallation events remain above 7 MeV, and therefore more than 25% of the final sample (the recent rate is about 5.7 events / day above 7 MeV) consists of the spallation events.

(3) Gamma rays from the rock

The efficiency of the gamma cut (subsection 5.3.4) is estimated by using the Ni-Cf gamma ray source which was placed in the anti-counter. 30% of the data in the fiducial volume remained after the cut [ref 4-5]. The event rate of the real data before and after the cut was 9.5 events / day and 5.7 events / day above 7.0 MeV for the most recent 100 days. Considering the 13% dead volume of the cut, it means that 25% of the final data is originated from the gamma rays from the surrounding material.

(4) Atmospheric neutrinos

A primary cosmic ray such as a proton or helium collides with the atmosphere of the earth and initiates a hadronic shower, and the secondary mesons produce atmospheric neutrinos through the decays:



Although extensive study of the atmospheric neutrino has been done [ref 5-6], an estimate of the absolute flux especially in the low energy region less than 100 MeV, is uncertain to about a factor of 2. The contribution from atmospheric neutrinos below 50 MeV to the low energy final sample is estimated by a Monte Carlo calculation to be about 0.1 events / year / 680 tons [ref 5-7].

In the case that the muons which are produced by a charged current interaction of an atmospheric neutrino have low momentum and are not observed (invisible muon), the subsequent decay electrons are another background. The background rate from such invisible muons is estimated to be less than 1 events / year / 680 tons [ref 5-7].

Therefore, the background from atmospheric neutrinos are negligible for solar neutrino and anti neutrino observation.

(5) Reactor neutrinos

A power reactor is maintained by fission of ^{235}U , ^{239}Pu , ^{238}U and ^{241}Pu . The fission products emit $\bar{\nu}_e$ in their β^+ decays. The total reactor power in the world in 1990 was 341 GW (USA: 106 GW, France: 56 GW, USSR: 35 GW, Japan: 32 GW) [ref 5-8]. The contribution of the reactor neutrinos to the Kamiokande detector may be considerable. We estimated the background rate as follows:

- The total power is equivalent to a 6.7×10^{-1} MW reactor at the distance of 1 km from the Kamiokande detector. The contributions are (all translated to the effective power at 1 km):

Kashiwazaki Japan: 12.89×10^{-2} MW; Takahama Japan: 10.47×10^{-2} ; Tsuruga Japan: 9.95×10^{-2} ; Mihama Japan 7.40×10^{-2} ; the rest in Japan: 24.29×10^{-2} ; South Korea: 1.40×10^{-2} ; Taiwan: 1.30×10^{-3} ; USA: 1.22×10^{-3} and so on [ref 5-8].

- The energies released per fission are 201.7 MeV (^{235}U), 205.0 MeV (^{239}Pu), 210.0 MeV (^{238}U) and 212.4 MeV (^{241}Pu) [ref 5-9].
- The mean contributions to the reactor power are approximated by 0.55 (^{235}U), 0.32 (^{239}Pu), 0.07 (^{238}U), 0.06 (^{241}Pu).
- The differential energy spectra of $\bar{\nu}_e$ produced in units of /fission/MeV are shown in Fig. 5.25 [ref 5-10].
- The energy spectrum of $\bar{\nu}_e$ at Kamiokande is then derived (in Fig. 5.26). The positron energy spectrum considering the detector response of Kamiokande-III is shown in Fig. 5.27. It corresponds to 0.003 events / day / 680 tons above 7.5 MeV and 0.005 events / day / 680 tons above 7.0 MeV.

Hence, the contribution of the reactor $\bar{\nu}_e$ is negligible for the solar (anti-)neutrino observation which is expected (SSM-prediction) to be 0.685 events / day / 680 tons above 7.5 MeV and 0.816 events / day / 680 tons above 7.0 MeV.

In summary, the remaining background is examined and found to come mainly from ^{222}Rn (~30%) which appears as the soft component of the energy spectrum, spallation events (>25%), and gamma rays from the rock (~25%) as the hard component. It is still possible to decrease the low energy background by eliminating ^{222}Rn in the water. The high energy background will be reduced by a thicker anti-layer and shield, and by the improvement of the vertex resolution which will increase the rejection efficiency of the spallation cut. These tasks should be accomplished by the forthcoming experiment: Super-Kamiokande.

References

Chapter 5. Data analysis

- [5-1] W.R.Nelson, H.Hirayama and D.W.O.Rogers, "The EGS4 Code System" SLAC-report-265 (1985).
- [5-2] M.Yamada et al., Phys.Rev. **D44**(1991)617.
- [5-3] T.Suzuki, D.F.Measday and J.P.Roalsvig, Phys.Rev. **C35**(1987)2212.
- [5-4] M.Morita, Beta decay and Muon Capture, (W.A.Benjamin Company, 1973), p276.
- [5-5] H.Überall, Study of Nuclear Structure by Muon Capture, Springer Tracts **71**(1974)1.
- [5-6] G.Barr, T.K.Gaisser and T.Stanev, Phys.Rev. **D39**(1989)3532; M.Honda, K.Kasahara, K.Hidaka and S.Midorikawa, Phys.Lett **B248**(1990)193; H.Lee and Y.S.Koh, Nuovo Cimento, **105B**(1990)883.
- [5-7] K.S.Hirata, Ph.D.thesis, Univ.of Tokyo (1991), ICRR-Report-239-91-8.
- [5-8] Japan Atomic-power Industrial Federation, Report on the trend of Nuclear Reactor Development in the World 1990, in japanese.
- [5-9] F.Boehm and P.Vogel, Physics of Massive Neutrinos, (Cambridge University Press)
- [5-10] K.Schreckenbach et al., Phys.Lett. **B160**(1985)325; H.V.Klapdor et al., Phys.Rev.Lett. **48**(1982)127; P.Vogel et al., Phys.Rev. **C24**(1981)1543.

6. Results

6. Results

6.1. Solar neutrino flux

This thesis includes the data from January 1987 to February 1993. Total live time is 1557 days and it is subdivided into "Kam-2 gain×1", "Kam-2 gain×2", "Kam-3 7.5 MeV" and "Kam-3 7.0 MeV" with 450, 594, 200 and 314 days, respectively. Fiducial volume for solar neutrino analysis is 680 tons for all phases (Fiducial volume for Kam-3 is shifted 57 cm upward to obtain a symmetric geometry). The number of events in the final sample for the four different terms are 669, 3113, 946 and 2023 events, respectively. We tested the directional correlation between the observed events and the sun, then obtained the number of solar neutrino events by counting the excess toward the sun above the flat backgrounds. We compare the number of excess events with the expected number from a standard solar model and the standard electro-weak theory. The result from the Kamiokande-2 experiment was $\frac{\text{data}}{\text{SSM}_{\text{BP92}}} = 0.47 \pm 0.05 \pm 0.06$, and we will give results from 514 days of Kam-3 data and the combined results.

6.1.1. Signal extraction

The SSM_{BP92} predicts 0.67 solar neutrino events per day in Kam-3 for $E_e \geq 7.5$ MeV and 0.80 events / day for $E_e \geq 7.0$ MeV, and the final data consist of 4.7 events / day and 6.4 events / day, respectively. We can make use of the strong directional correlation of the solar neutrino events as seen in equation (eq 4-18) to enhance the signal to noise ratio. The different angular distribution of the solar neutrino events (toward the sun) from the backgrounds (flat) enabled us to extract the number of solar neutrino events.

A maximum likelihood method was used to extract the solar neutrino signal. We prepared two likelihood functions: one for background and the other for the signal distribution.

We have estimated that the remaining backgrounds in the final sample consisted of radon products, spallation products and gamma rays from the environment. The background from the radon and the spallation products is expected to distribute isotropically. One may think that the gamma rays from outside have directionality. These effect turns out to be small (see section 6.2). It is further reduced by the following reason, especially for the total flux measurement. The background comes from a 4π solid angle and the fact that the direction to the sun changes greatly in the detector coordinate completely smears out this small directionality. Therefore, we can expect that the gamma rays do not cause any systematic effect, and we can assume that the angular distribution of background is flat. Hence, we took the likelihood function for the background as,

$$L_{B.G.}(E, \cos\theta) = f(\cos\theta) = 0.5, \quad \left(\int f(\cos\theta) d(\cos\theta) = 1 \right). \quad (\text{eq 6-1})$$

We must consider the angular distribution of the solar neutrino events very carefully, because the fit depends on the shape of the distribution. The response of each detector segment may not be isotropic, since the dead PMTs influence the effective photo-coverage around their position. In order to take into account the change in the spatial distribution and the time variation of the number of dead PMTs, we needed to consider the run-time distribution which influences the directional distribution toward the sun in the detector system. Time variation of dead PMTs was corrected for in the definition of the effective energy as shown in subsection 5.1.4, but a uniform distribution of dead PMTs was assumed in this correction. To consider its spatial distribution and to follow the time variation of the number of dead PMTs, we dynamically generated the Monte Carlo events of solar neutrinos with two events for every real-time-minute, considering the distribution of dead PMTs and the direction of the sun. We applied the same reduction processes to the Monte Carlo events, except for the reduction of spallation products which is difficult to simulate and does not distort the angular distribution. We defined the likelihood function for the signal $L_{\text{signal}} = s(E, \cos\theta)$ as a function of

electron energy and opening angle from the sun (see Fig. 6.1), where the function is normalized by

$$\int s(E, \cos\theta) d(\cos\theta) = 1. \quad (\text{eq 6-2})$$

Finally, we derived the likelihood function for the final data sample as

$$\begin{aligned} L(E, \cos\theta, x) &= (1-x) \times L_{B.G.}(E, \cos\theta) + x \times L_{\text{signal}}(E, \cos\theta) \\ &= \frac{1-x}{2} + x \times s(E, \cos\theta). \end{aligned} \quad (\text{eq 6-3})$$

Where, x is the parameter that expresses the fraction of events coming from the sun in the final sample.

The signal to noise ratio becomes better in the high energy region, for example, $S/N \simeq 2$ in the region $E_e \geq 10$ MeV, $\cos\theta \geq 0.8$ and $S/N \simeq 1.3$ for $E_e \geq 7.5$ MeV, $\cos\theta \geq 0.8$. Therefore, we can make the statistical error smaller, by dividing the data into energy bins in the fitting procedure. Hence, we take the likelihood function as follows,

$$L(x) = \prod_i \left\{ \prod \left(\frac{1 - x_i(x)}{2} + x_i(x) \times s(E, \cos\theta) \right) \right\}, \quad (\text{eq 6-4})$$

or

$$\log(L(x)) = \sum_i \left\{ \sum \log \left(\frac{1 - x_i(x)}{2} + x_i(x) \times s(E, \cos\theta) \right) \right\}, \quad (\text{eq 6-5})$$

with the condition,

$$x_i(x) = \frac{N}{N^{MC}} \times \frac{N^{MC}_i}{N_i} \times x \quad (0 < x < 1), \quad (\text{eq 6-6})$$

where i runs from 1 to the number of energy bins and N , N^{MC} , N_i and N^{MC}_i are the total number of events in the final sample, total number of expected events, number of observed events in the i -th energy bin and number of expected events in the i -th energy bin, respectively. Equation (eq 6-6) is the binding condition for reproducing the expected energy spectrum of the solar neutrino events. Note that this method assumes that the ^8B neutrino spectrum has no spectrum distortion, hence the flux obtained here should be carefully treated in discussing such as neutrino oscillations. We used each energy bin independently to obtain the energy spectrum. This spectrum can be used for the proper test of neutrino oscillation solutions. When we want to treat data for Kam-2

and Kam-3, together, we must prepare the likelihood function individually for each data set and combine energy bins in all data sets as if we only increased the number of energy bins. We obtained the number of neutrino events from

$$N_{\nu} = x_{\max} N = \sum x_i(x_{\max}) N_i, \quad (\text{eq 6-7})$$

where x_{\max} is selected to maximize the likelihood function $L(x_{\max}) = L_{\max}$. Statistical error is derived to find the value x_{error} which satisfies,

$$L(x_{\text{error}}) = \exp(-0.5) \times L_{\max}. \quad (\text{eq 6-8})$$

6.1.2. ^8B solar neutrino flux

As a result, we obtained the number of solar neutrino events,

$$N = 74.5^{+14.3}_{-13.1} \text{ events} \quad (\text{Kam-3 } E_e \geq 7.5 \text{ MeV, 200.3 days}),$$

$$N = 151.5^{+21.0}_{-19.6} \text{ events} \quad (\text{Kam-3 } E_e \geq 7.0 \text{ MeV, 314.2 days}),$$

and the event rate,

$$R = 0.372^{+0.071}_{-0.065} \text{ events / day} \quad (\text{Kam-3 } E_e \geq 7.5 \text{ MeV}),$$

$$R = 0.482^{+0.067}_{-0.062} \text{ events / day} \quad (\text{Kam-3 } E_e \geq 7.0 \text{ MeV}).$$

The expected event rates for the SSM corresponding to the above measurements are

$$R_{\text{SSM}} = 0.685 \text{ events / day (Kam-3 } E_e \geq 7.5 \text{ MeV) and,}$$

$$R_{\text{SSM}} = 0.816 \text{ events / day (Kam-3 } E_e \geq 7.0 \text{ MeV).}$$

These predictions were obtained by considering the following facts.

(1) The interaction rate of solar neutrinos in the total volume (2142 tons of water, the number of electrons is $N_e = 7.16 \times 10^{32}$) is

$$N_e \times \int_0^{\infty} \sigma_{\nu e}(E_{\nu}) \times \phi_{8\text{B}}(E_{\nu}) dE_{\nu} = 21.4 \text{ events / day.}$$

where the neutrino flux is normalized to

$$\int_0^{\infty} \phi_{8\text{B}}(E_{\nu}) dE_{\nu} = 5.69 \times 10^6 \text{ cm}^{-2}\text{sec}^{-1},$$

(2) The fractions of the events observable are limited at 3.69% ($E_e \geq 7.5 \text{ MeV}$) and 4.43% ($E_e \geq 7.0 \text{ MeV}$): the spallation cut was treated separately, by the small fiducial volume (680 tons) and the y-distribution of the recoil electron (eq 4-8).

(3) The dead time fraction from the spallation cut is 0.15.

Taking the ratio of R and R_{SSM} , the solar neutrino flux relative to the SSM_{BP92} becomes

$$\frac{\text{data}}{\text{SSM}} = 0.543^{+0.104}_{-0.095} \quad (\text{Kam-3, } E_e \geq 7.5 \text{ MeV, 200.3 days}),$$

and

$$\frac{\text{data}}{\text{SSM}} = 0.591^{+0.082}_{-0.076} \quad (\text{Kam-3, } E_e \geq 7.0 \text{ MeV, 314.2 days}).$$

Combining two data sets, the total live time becomes 514.5 days and the result from Kamiokande-3 solar neutrino observation ends up as

$$\frac{\text{data}}{\text{SSM}} = 0.574^{+0.064}_{-0.059} \text{ (statistical error)} \pm 0.061 \text{ (systematic error).}$$

If we combine the results with Kamiokande-2 data, this yields

$$\frac{\text{data}}{\text{SSM}} = 0.514^{+0.043}_{-0.037} \pm 0.061 \quad (\text{Kamiokande-2\&3, 1557 days}),$$

for 1557 days' data.

The magnitude of the systematic errors in Kamiokande-3 is almost same as that of Kamiokande-2 and it will be described in the next section. Fig. 6.2 shows the angular distributions of the final sample superimposed with the best fit (dashed histogram) and an expectation from the SSM (solid histogram) for Kam-3 data and the complete 1557 days Kamiokande data (Kam-3 data with different thresholds are also shown). The distribution of the likelihood values for all combined data is shown in Fig. 6.3. The total number of solar neutrino events observed in 1557 days of data thus becomes $439^{+36.6}_{-31.4}$.

The energy spectrum of the recoil electrons is obtained by applying the same likelihood method (eq 6-4) to each energy bin. Fig. 6.4 shows the energy spectrum for 1557 days of data. Low energy data points have less data-taking time because of the chronological change of the energy thresholds. The energy spectrum with respect to the

prediction of the SSM is also shown in Fig. 6.5, which shows no strong deviation (flat in the ratio) except for the fact that the average value is only a half of the prediction. This spectrum information is very useful in studying the parameter region in which the neutrino spectrum is strongly distorted, such as the adiabatic region and the just-so region of neutrino oscillation models.

6.2. Systematic errors for the solar neutrino flux calculation

The systematic errors in the data analysis have been estimated. We compared the data with the Monte Carlo simulation in the various steps of the analysis. We sometimes used the comparison between the Monte Carlo simulation and the data to evaluate systematic errors.

As written in chapter 5, events were passed through many steps to reduce the background. We estimated the systematic errors in every reduction step.

(1) trigger efficiency (0.5%)

The trigger threshold has been set at a sufficiently low level in comparison with the analysis threshold. When we set the analysis threshold at $E_e = 7.5$ MeV, the trigger threshold was $\epsilon_{50\%} \sim 6.2$ MeV (Kam-2 gain $\times 2$); when the analysis threshold was changed to $E_e \geq 7.0$ MeV, the trigger threshold had been lowered to $\epsilon_{50\%} \sim 5.0$ MeV (see Fig. 4.22 for the chronological change of the trigger and analysis threshold). We estimate that the event loss due to miss-triggering is much less than 0.5% from the evaluation of the trigger efficiency (see Fig. 4.21). We take 0.5% for the uncertainty of the trigger efficiency.

(2) muon reduction (0.02%)

The muon rejection criteria,

inner total photo-electron ≥ 500 , and anti total photo-electron ≥ 50 ,

may cause a loss of the solar neutrino events if the events accidentally had high pulse heights from noise. We checked the Cf+Ni calibration data to investigate the occasional association of high pulse height PMTs, and found that this process affects

no more than 0.02%. We took this value as the systematic error for the muon reduction step.

(3) noise reduction (0.1%)

The noise rejection criteria,

$$\text{"goodness"} \geq 0.4, N_{\text{hit}} / N_{250} \geq 0.6, \text{ and } N_{\text{neg}} / N_{\text{dsc}} < 0.4,$$

have an efficiency for the signal of 99.7%, which is well reproduced by the Monte Carlo simulation and corrected for. Some of the quantities used in this reduction step are defined in the reconstruction process. We revised the vertex reconstruction program for Kamiokande-3. When we used the program used for Kamiokande-2, the efficiency was 99.8%. Therefore, we took the difference of 0.1% for the systematic error at this step.

(4) Fiducial volume cut (3.2%)

Solar neutrino analysis was done for the events in the 680 tons of fiducial volume. We compared the reduction efficiencies for the two different vertex reconstruction programs (for Kamiokande-3, ϵ_3 , and that for Kamiokande-2, ϵ_2):

$$\frac{\epsilon_3 - \epsilon_2}{\epsilon_3} = -1.3\% \text{ (Monte Carlo), } +1.9\% \text{ (Real data).}$$

We took the value $\pm 3.2\%$ for the systematic error of the fiducial cut.

(5) energy cut or absolute energy scale (6.9%)

Energy cuts cause a systematic effect through the uncertainty of the energy scale. As mentioned in appendix 5.1, absolute energy calibration has an ambiguity of $\pm 2.3\%$. A little shift of an energy cut makes a large change in the reduction efficiency because the solar neutrino signal has a steep energy spectrum. This effect is serious when the energy threshold is high. For example, the change of reduction efficiency for a 9.3 MeV threshold was 5% for a 1% shift of the energy scale; the changes for 7.5 MeV and 7.0 MeV thresholds were only 3% and 2% for 1% change of the scale, respectively. We have 200.3 days of data with a 7.5 MeV threshold and 314.2 days of data with a 7.0 MeV threshold. We took a conservative value of $2.3\% \times 3 = 6.9\%$ as the systematic error for this effect.

(6) spallation cut (1%)

The dead time of the spallation cut, 15%, was derived from 80 thousand randomly selected muon events and solar neutrino events made by Monte Carlo simulation with high enough statistics. We applied the spallation cut to random combinations of muon events and the simulated solar neutrino events. The statistical error $1 / \sqrt{80000} \times 15\% = 0.05\%$ is a satisfactorily small value. But, the most uncertainty comes from the muon event rate selected by $Q_{\text{eff}} > 10,000$ p.e. We controlled the detector stability within 3% (for the pulse height of the muons: effectively 10,000 photo-electrons). This leads that the muon rate with $Q_{\text{eff}} > 20,000$ p.e. (relevant region for the spallation cut) may change by 6% using the measured muon spectrum. Therefore, we took $15\% \times 6\% = 1\%$ for the systematic error for the spallation cut due to the uncertainty of the dead time estimate.

(7) gamma ray cut (0.5%)

The reduction efficiency for solar neutrino events (Monte Carlo) by the vertex reconstruction program for Kam-3 and Kam-2 are 87.0% and 86.5%, respectively. We took 0.5% systematic error for this reduction.

(8) uncertainty of the angular resolution (7%)

We experimentally estimated the angular resolution and its uncertainty with a collimated Cf+Ni (9 MeV) gamma ray source, and the obtained value (the mean opening angle) of $35.4^{\circ} {}^{+1.5^{\circ}}_{-2.3^{\circ}}$ was well reproduced by the detector simulation (38.0° [ref 4-3]). We conservatively took 5° uncertainty for the angular resolution. To estimate the effect of this uncertainty on the solar neutrino flux, we used a likelihood function distorted by 5° for the signal extraction and compared obtained fluxes with that obtained by the normal likelihood function. Their difference of 7% was taken as the systematic error from the uncertainty of the angular resolution.

(9) live time calculation (0.5%)

(10) assumption of a flat background (5%)

We assumed an isotropic background distribution to extract the solar neutrino signal. This assumption must be verified because a possible anisotropy of the

background in the detector system (for example gamma rays from the surroundings, or a not-uniform detector response) might make the angular distribution not flat. If we assign arbitrary times to the solar neutrino events, the angular distribution of these events becomes flat, but the same assignment will not change the angular distribution of background events because their directional distribution does not change in time (the anisotropy we are considering here is a function of detector coordinates). This difference is the basis for the strategy used in evaluating the angular distribution of background events. We have tested the systematic effect of the flat background assumption by the following procedure:

- a. We selected excess events from the direction of the sun with the assumption of flat background as a first approximation. These events were selected randomly in time from the final sample. The remaining events should be almost all background events.
- b. We reassigned randomly selected times to the remaining events so that the contribution of solar neutrino events to the angular distribution is smeared. Then we can consider the angular distribution of the redefined samples as just a background distribution. And the distributions were quite flat.
- c. We counted excess events for the combined data of the events removed in step (a) and the redefined events from step (b).
- d. We compared the values obtained in step (c) with our original result and we obtained the systematic error from the flat background assumption to be 5%.

(11) calculation of $\nu_e e^-$ cross section (1%)

A recent accurate measurement [ref 2-1] reduced the ambiguity in the weak parameters. The error in $\sin^2 \theta_W = 0.2259 \pm 0.0029$ now mostly comes from the unknown top mass and radiative corrections. We have estimated that the systematic error in the theoretical calculation of the cross section is about 1% considering two effects: (i) radiative corrections [ref 2-3,4-10,6-1] and (ii) atomic binding of the electrons of order $(\alpha Z / n)^2$ where α is the fine structure constant, Z the effective

charge on the nucleus seen by the electron and n the principal quantum number of a hydrogenic-like orbit [ref 6-2].

We assumed that these systematic errors are not correlated, and derived the total systematic error by summing up these values in quadrature. The total systematic error for the solar neutrino flux in Kamiokande-3, thus, is 11.6%.

6.3. Neutrino flux in correlation with the sun-spot number

6.3.1. Anti-correlation in the ^{37}Cl experiment

Before we present our results on the correlation with sun-spot numbers, we evaluate the results from the ^{37}Cl experiment. The solar neutrino flux observed by the ^{37}Cl experiment for more than 20 years is shown in Fig. 6.6 [ref 6-3] as a function of sun-spot number [ref 6-4]. We simply used a linear function to express the anti-correlation, (it has been suggested [ref 6-5] that the function $R_{\text{Ar}} = A \cos^2(\sqrt{N_{\text{SS}}})$ may be more plausible). The anti-correlation is then described by

$$R_{\text{Ar}} = (-1.36 \times 10^{-3} \pm 0.51 \times 10^{-3}) \times N_{\text{SS}} + (0.524 \pm 0.055), \quad (\text{eq 6-9})$$

and the significance level of the correlation is 2.7σ . (It has been reported [ref 1-29] that the significance level depends on the treatment of the statistical error of each data point. We have taken average errors [ref 6-3] instead of up-down asymmetric errors for the calculation.) There is a slight inconsistency in the ^{37}Cl data. We were required to correct the absolute value of the fitted result in order for the average flux values obtained both from Davis's paper and from the simple average in Fig. 6.6 to agree. The central value of the ^{37}Ar production rate was 0.398 events / day with our statistical treatment, but the value derived by Davis et al [ref 1-2] was 0.509 ± 0.031 events / day. Hence, we shifted the result for the averaged value to be the same. 0.08 ± 0.03 out of the 0.509 is background, therefore it is subtracted. Then, the net ^{37}Ar production rate 0.429 ± 0.043 is translated to 2.28 ± 0.23 SNU [ref 1-2]. As a result, the expression (eq 6-9) is now

$$\frac{\text{data}}{\text{SSM}} = (-0.90 \times 10^{-3} \pm 0.34 \times 10^{-3}) N_{\text{SS}} + (0.369 \pm 0.045). \quad (\text{eq 6-10})$$

If we take this correlation positively, the most probable explanation may be a neutrino magnetic moment as large as $\mu_\nu \geq 10^{-11} \mu_B$. If the neutrino had such a large magnetic moment, a solar neutrino could transform a sterile state by magnetic interaction with the solar magnetic field. The magnetic strength in the convection zone ($R_{\text{sun}} \geq 0.7$) is expected to change largely in correlation with the solar activity (as a result, in correlation with sun-spot numbers). Hence, the sun-spot numbers could anti-correlate with the solar neutrino flux as was observed in the ^{37}Cl experiment. Now the Kamiokande solar neutrino observation has covered an entire solar maximum period, therefore, the information on time variation from the Kamiokande result will be very important in examining these hypothesis. In the following subsections, we study the solar neutrino flux observed in Kamiokande as a function of time. Then, we evaluate a possible time variation of the neutrino flux in correlation with sun-spot numbers.

6.3.2. 200 days plot

The total data taking time of solar neutrino observation is 1557 days from January 1987 to February 1993. This observation includes the entire solar maximum period of solar cycle 22. The sun-spot numbers during this period have changed greatly from 0 to 200 (see Fig. 6.7). Hence, the data will suited for testing a possible anti-correlation of the solar neutrino flux with the sun-spot numbers. We divided the data into seven periods in order that every period contains about 200 days of data taking time (the last period has about 300 days of data):

| | | |
|------------|--------------------------------|------------|
| (period-1) | January 1987 to August 1987 | 207.3 days |
| (period-2) | September 1987 to May 1988 | 241.5 days |
| (period-3) | June 1988 to December 1988 | 193.9 days |
| (period-4) | January 1989 to July 1989 | 190.9 days |
| (period-5) | August 1989 to April 1990 | 209.0 days |
| (period-6) | December 1990 to November 1991 | 200.3 days |
| (period-7) | November 1991 to February 1993 | 314.2 days |

Period-1 and period-2 are the data from Kam-2 gain \times 1 in which the energy threshold for the recoil electron is 9.3 MeV. The data of period-3 to period-5 have come from Kam-2 gain \times 2 and have been analyzed with a 7.5 MeV threshold. Period-6 and period-7 belong to Kam-3, and the threshold energies are 7.5 MeV for period-6 and 7.0 MeV for period-7. The average sun-spot numbers during these periods are 23.6, 53.9, 125.2, 150.1, 159.1, 149.7 and 96.6, respectively [ref 6-4]. The solar neutrino flux relative to the SSM_{BP92} for these periods are

| | | |
|------------|--------------------------------------|-----------------------|
| (period-1) | data/SSM = $0.42^{+0.14}_{-0.13}$ | ($E_{th} = 9.3$ MeV) |
| (period-2) | data/SSM = $0.55^{+0.14}_{-0.13}$ | ($E_{th} = 9.3$ MeV) |
| (period-3) | data/SSM = $0.52^{+0.11}_{-0.10}$ | ($E_{th} = 7.5$ MeV) |
| (period-4) | data/SSM = $0.42^{+0.11}_{-0.10}$ | ($E_{th} = 7.5$ MeV) |
| (period-5) | data/SSM = 0.45 ± 0.12 | ($E_{th} = 7.5$ MeV) |
| (period-6) | data/SSM = $0.543^{+0.104}_{-0.095}$ | ($E_{th} = 7.5$ MeV) |
| (period-7) | data/SSM = $0.591^{+0.082}_{-0.076}$ | ($E_{th} = 7.0$ MeV) |

respectively. These results are shown in Fig. 6.8 together with an inverse plot of the sun-spot numbers. If we set the energy threshold at 9.3 MeV (period-1 and 2 are taken with this high threshold), the ratios of period-3 to period-7 become:

| | | |
|------------|--------------------------------------|-----------------------|
| (period-3) | data/SSM = $0.48^{+0.14}_{-0.12}$ | ($E_{th} = 9.3$ MeV) |
| (period-4) | data/SSM = $0.35^{+0.13}_{-0.12}$ | ($E_{th} = 9.3$ MeV) |
| (period-5) | data/SSM = $0.37^{+0.13}_{-0.12}$ | ($E_{th} = 9.3$ MeV) |
| (period-6) | data/SSM = $0.535^{+0.131}_{-0.121}$ | ($E_{th} = 9.3$ MeV) |
| (period-7) | data/SSM = $0.556^{+0.114}_{-0.107}$ | ($E_{th} = 9.3$ MeV) |

The systematic error for the absolute flux is 0.06 as described in section 6.2. But this is an overestimate for the relative flux. The uncertainty in the relative flux mainly comes from a small change in the energy scale described in appendix 5.1 which

corresponds to about 8% of the flux value. Then systematic errors for the relative flux are small.

6.3.3. Correlation of the ^8B neutrino flux with the sun-spot numbers

If we assume a linear function for representing the correlation between the solar neutrino flux and the sun-spot numbers as was discussed in subsection 6.3.1 for the ^{37}Cl experiment, the results from the seven periods (different thresholds) of the Kamiokande data are

$$\frac{\text{data}}{\text{SSM}} = (-0.21^{+1.02}_{-1.05}) \times 10^{-3} N_{ss} + (0.536^{+0.140}_{-0.128}), \quad (\text{eq 6-11})$$

where N_{ss} are the sun-spot numbers averaged over one month shown in subsection 6.3.1. χ^2 for the fit is defined by

$$\chi^2 = \sum \frac{(x_i - \alpha y_i)^2}{\sigma_i^2 + (0.08x_i)^2} + \left\{ \frac{(\alpha - 1)^2}{(\sigma_{\text{sys}}/x_{\text{center}})^2 - 0.08^2} \right\}, \quad (\text{eq 6-12})$$

where x_i is the ratio of the observed event rate to the SSM at the i -th energy bin, y_i the expected ratio derived by the neutrino oscillation calculation, σ_i the statistical error of x_i , $\sigma_{\text{sys}}/x_{\text{center}} = 0.061/0.514$ the ratio of the systematic error to the central value, α is a normalization factor to minimize the χ^2 so that the systematic error of overall normalization is included, and the uncertainty in the relative flux of 8% is added to each data point. Fig. 6.9 shows a contour map of the χ^2 distribution. χ^2_{min} was 2.2 for the 7 data point fit. The obtained coefficient in the linear function, $(-0.21^{+1.02}_{-1.05}) \times 10^{-3}$, is consistent with zero, and thus no significant correlation was found in the Kamiokande results. The same conclusion can be also obtained for the data with the common threshold of $E_{th} = 9.3$ MeV:

$$\frac{\text{data}}{\text{SSM}} = (-0.57^{+1.07}_{-1.08}) \times 10^{-3} N_{ss} + (0.534^{+0.141}_{-0.133}), \quad (\text{eq 6-13})$$

with $\chi^2_{\text{min}} = 2.37$. A contour map of the χ^2 distribution is also shown in Fig. 6.9.

90% C.L. intervals for the parameter are

$$-1.91 \times 10^{-3} < \alpha < 1.49 \times 10^{-3} \quad \text{for the different threshold data, and} \quad (\text{eq 6-14})$$

$$-2.36 \times 10^{-3} < \alpha < 1.19 \times 10^{-3} \quad \text{for the common threshold data.} \quad (\text{eq 6-15})$$

This conclusion (consistent with no correlation) must be satisfied when deriving the parameters for the hybrid model which must explain, at the same time, the anti-correlation in the chlorine data.

6.4. Anti-neutrino flux

We have succeeded in observing the finite solar neutrino flux. We should note that the Kamiokande detector also has the capability of detecting $\bar{\nu}_e$ because of the large number of free proton targets in the water and the large cross section for $\bar{\nu}_e p$ interaction (20 times the $\nu_e e$ scattering in water). We, therefore, searched for the $\bar{\nu}_e$ events in the solar neutrino sample.

There is a particular interest in $\bar{\nu}_e$ detection. One reason for this interest is a solar $\bar{\nu}_e$ creation by the hybrid-mechanism of resonant spin flavor precession and matter oscillation, which may be the answer to the solar neutrino problem and which may also explain the cause of the anti-correlation between the flux and the sun-spot number in the ^{37}Cl experiment and the lack of correlation in the Kamiokande experiment. In the hybrid model, we can expect $\bar{\nu}_e$ creation through the following mechanism,

- Assuming that neutrinos are Majorana and they have large transition magnetic moment (about $10^{-11} \mu_B$), ν_e produced in the fusion reaction chain at the center of the sun convert to $\bar{\nu}_\mu$ or $\bar{\nu}_\tau$ through interactions with the solar magnetic field ($\gtrsim 1$ kG).
- If neutrinos have mass and mixing between flavor eigen-states and mass eigen-states, $\bar{\nu}_{\mu(\tau)}$ can oscillate into $\bar{\nu}_e$ by the neutrino oscillations in vacuum.

If such a mechanism really took place, Kamiokande might be able to observe the resultant $\bar{\nu}_e$ due to the large acceptance for $\bar{\nu}_e p$ interactions.

6.4.1. Spectrum independent $\bar{\nu}_e$ flux limit

The solar neutrino events have strong directionality toward the sun and appear as excess events in the region "S" in Fig. 6.10, while the angular distribution of $\bar{\nu}_e p$ is almost flat and belongs to region "B". That is, the $\bar{\nu}_e$ signal is hidden in the

"background" region. The backgrounds for a $\bar{\nu}_e$ signal, therefore, consist of radon, spallation products, gamma rays and finally solar neutrinos. We can possibly subtract the solar neutrino events (about 440 events for 1557 days of data). But the other backgrounds cannot be subtracted, although we know that 30% of the remaining background comes from radon, 25% from spallation and 25% from gamma rays, because our knowledge is not precise. Hence, we must take a conservative approach for the evaluation of the $\bar{\nu}_e$ flux. We did not subtract these backgrounds in this analysis to obtain an upper limit for the $\bar{\nu}_e$ flux. We used the events in region "A",

$$\cos\theta_{sun} < 0.8,$$

instead of subtracting the solar neutrino signal. We assumed all remaining events in region "A" are produced by the $\bar{\nu}_e p$ interaction and set an upper limit of the flux. We did not use the small directional correlation of $\bar{\nu}_e$ events. The resulting flux upper limit can be applied to any possible $\bar{\nu}_e$ source.

We cannot estimate the energy spectrum of $\bar{\nu}_e$ without knowing the exact mechanism of the $\bar{\nu}_e$ creation. Even if the hybrid hypothesis took place, the energy spectrum of $\bar{\nu}_e$ would vary depending on its parameters: $\mu_B \times B_{sun}$, δm^2 and $\sin^2 2\theta$. Hence, we intended to obtain the spectrum independent but conservative $\bar{\nu}_e$ flux limit with the following procedure,

- (1) M.C. simulation was used to evaluate the detection efficiency. To represent monochromatic $\bar{\nu}_e$, positron events were generated at every energy,

$$E_e = E_\nu + m_p - m_n = E_\nu - 1.293 \text{ MeV}.$$

- (2) We took into account the detector response for the positron (i.e. energy resolution).
- (3) These events were passed through the same event reduction programs used for processing real data, and an additional cut of $\cos\theta_{sun} < 0.8$ was applied.
- (4) We then obtained the visible energy distribution of the $\bar{\nu}_e$ events at each energy point.
- (5) An energy cut was determined at each point in order to maximize the detection efficiency and minimize the background contamination.

(6) Finally, we could obtain the $\bar{\nu}_e$ flux upper limit by comparing the efficiency with the observed number of events within the cut.

Fig. 6.11 shows the observed energy spectrum of the final data sample with $\cos\theta_{\text{sun}} < 0.8$. The anti-neutrino flux upper limit was obtained by requiring that this not exceed the observed event rate. Fig. 6.12 shows the 90% C.L. $\bar{\nu}_e$ flux upper limit obtained through the above procedure for each neutrino energy. We used the data taken for the periods 3, 4 and 5 defined in subsection 6.3.2 (the average sunspot numbers for these periods was 145). Comparison of this limit to the ^8B neutrino flux predicted by SSM_{BP92} was made simply by taking the ratio. Fig. 6.13 shows the flux limit relative to the ^8B solar neutrino flux. It must be noted that the ^8B neutrino has a continuous spectrum, although a monochromatic energy spectrum was assumed for $\bar{\nu}_e$ (/cm²/sec). Hence, the width of the $\bar{\nu}_e$ spectrum is needed to obtain their ratio. We treated the $\bar{\nu}_e$ flux limit as if it is derived with the energy spread of just 1 MeV. We could obtain the most strict limit for the ratio at $E_\nu = 12.5$ MeV:

$$\left. \frac{\phi_{\bar{\nu}_e}}{\phi_{\nu^8\text{B}}} \right|_{E_\nu=12.5\text{MeV}} < 4.5\% \times \text{MeV},$$

at 90% confidence level.

If we know the energy shape of $\bar{\nu}_e$, we can obtain a much more restrictive limit. This is discussed in the next chapter, especially for the case of the hybrid model.

6.4.2. Systematic errors for the $\bar{\nu}_e$ flux limit

Estimate of the systematic errors for the $\bar{\nu}_e$ flux limit is straight forward because most of them are the same as in the solar neutrino case: trigger efficiency (0.5%), muon reduction (0.002%), noise reduction (0.1%), fiducial volume cut (3.2%), spallation cut (1%) and gamma ray cut (0.5%). The uncertainty of the angular resolution of the recoil electron which was important in the solar neutrino analysis does not contribute to the $\bar{\nu}_e$ observation because we do not need to know the angular distribution. Additional systematic error comes from the absolute energy scale for the energy window determination at each $\bar{\nu}_e$ energy which was typically 10%. Further uncertainty from the

calculation of the $\bar{\nu}_e p$ cross section is estimated to be 10%. Then, the total systematic error for the $\bar{\nu}_e$ flux limit is 15%.

References

- [6-1] S.Sarantakos et al., Nucl.Phys. **B217**(1983)84.
- [6-2] J.N.Bahcall, Phys.Rev. **B135**(1964)137.
- [6-3] K.Lande et al., Proceedings of the 25th International Conference on High Energy Physics, August 1990, Singapore, p667, edited by K.K.Phua and Y.Yamaguchi (World Scientific Publishing, Singapore, 1991); recent data are taken from reference [1-2].
- [6-4] Solar-Geophysical Data prompt reports (National Geophysical Data Center, Boulder, Colorado 80303).
- [6-5] G.Fiorentini and G.Mezzorani, Phys.Lett. **B253**(1991)181.

...the results of the analysis ...

...the results of the analysis ...

...the results of the analysis ...

...the results of the analysis ...

...the results of the analysis ...

...the results of the analysis ...

...the results of the analysis ...

...the results of the analysis ...

...the results of the analysis ...

...the results of the analysis ...

...the results of the analysis ...

...the results of the analysis ...

2. Interpretation and Discussion

The results of the analysis ...

The results of the analysis ...

The results of the analysis ...

The results of the analysis ...

The results of the analysis ...

The results of the analysis ...

The results of the analysis ...

The results of the analysis ...

The results of the analysis ...

The results of the analysis ...

The results of the analysis ...

The results of the analysis ...

7. Interpretation and Discussions

The emphasis in this thesis is placed on how to reconcile all the experimental results, including different time variability. However we first interpret the solar neutrino deficit, observed by the three types of experiments, in the "standard" frame work of neutrino oscillation solutions (section 7.1). This interpretation does not include an explanation of the time variation suggested in the chlorine experiment. Then, extensive efforts are made to explain a possible solution of the solar neutrino problem together with consideration of time variations in all observations from the point of view of a neutrino (transition) magnetic moment (section 7.2). Finally, we examine the $\bar{\nu}_e$ flux limit with various conditions on the solar magnetic field and its profile, and obtain excluded regions in the parameter space of $(\sin^2 2\theta, \delta m^2, \mu_\nu B_{\text{sun}})$ (section 7.3) for the case of Majorana neutrinos.

7.1. The "standard" interpretation of the solar neutrino deficit

As mentioned in section 1.3.5, astrophysical explanations seem to be ruled out as a solution to the solar neutrino problem, but neutrino oscillations are a possible and favorable approach to the problem. Hence, we first interpret the result from the 1557 days of data,

$$\frac{\text{data}}{\text{SSM}_{\text{BP92}}} = 0.514^{+0.043}_{-0.037} \pm 0.061, \quad (\text{eq 7-1})$$

in the frame work of neutrino oscillations.

7.1.1. MSW solution

A region where the MSW effect takes place ($10^{-5} < \sin^2 2\theta < 1$, $10^{-9} < \delta m^2 < 10^{-3}$) was first explored. In this study, the suggested time variation was ignored. Details of the calculation procedure for obtaining a solution are found in subsection 7.2.1, though it is briefly described in this subsection, because neutrino propagation under the MSW

mechanism is a simplified version of the hybrid model described in subsection 7.2.1 (the propagation matrix size is reduced from 4 by 4 to 2 by 2). The result of the MSW effect is also useful for a validity test of the techniques we used in the much more complicated calculation.

Electron-neutrinos produced at production points near the center of the sun are traced numerically to the surface with the propagation matrix (eq 3-28) for the parameter region of $10^{-5} < \sin^2 2\theta < 1$ and $10^{-10.1} < \delta m^2/E < 10^{-2.1}$ where the MSW effect takes place effectively. The neutrinos are further traced through one vacuum oscillation length so that the transition probability can be averaged over the path. The earth effect, which regenerates ν_e effectively in the region $\sin^2 2\theta \geq 10^{-2}$ and $10^{-7} \leq \delta m^2/E \leq 10^{-6}$, is not included in this calculation. The calculation speed was about 10 parameter sets / sec on a Hewlett Packard Apollo 9000/730 workstation.

The probability for each parameter set was averaged over the production points of the neutrinos (the individual neutrino production reactions take place at different regions inside the sun). The reaction rate in the detector was obtained from the cross sections shown in Fig. 4.1 and the detector responses (i.e. energy resolutions) shown in Fig. 4.15, each corresponding to Kam-2 gain \times 1, gain \times 2 and Kam-3. The spectrum of the recoil electron used was the average of above three responses with the weight of the different data taking times.

In order to search for favorable regions for the MSW solution, the calculated event rate and the energy spectrum were compared with the corresponding experimental results, the event rate; (eq 7-1) and the spectrum; Fig. 6.5. Fig. 7.1 shows the 90% C.L. allowed region in ($\sin^2 2\theta$ vs. δm^2) plane derived only by using the total flux information (eq 7-1). Next, we defined the following χ^2 to make use of the information in the energy spectrum,

$$\chi^2 = \sum \frac{(x_i - ay_i)^2}{\sigma_i^2} + \left(\frac{a - 1}{\sigma_{\text{sys}}/x_{\text{center}}} \right)^2, \quad (\text{eq 7-2})$$

which is obtained by removing the 8% uncertainty in the relative flux from the formula (eq 6-12). Fig. 7.2 shows the 90% C.L. allowed region (contour map at $\chi^2 = \chi^2_{\text{min}} +$

4.605) of the $\sin^2 2\theta$ - δm^2 plane from the Kamiokande result (1557 days). $\chi^2_{\text{min}} = 7.1$ with 8 data points from the energy spectrum was obtained at $(\delta m^2, \sin^2 2\theta) = (7.5 \times 10^{-8}, 0.94)$. The adiabatic region is eliminated by electron spectrum considerations.

Allowed regions for the chlorine and the gallium experiments are also derived. The experimental results used in the calculations are

$$\text{Chlorine experiment} \quad : \quad \frac{\text{data}}{\text{SSM}_{\text{BP92}}} = 0.285 \pm 0.029, \quad (\text{eq 7-3})$$

$$\text{Gallium experiments all combined} \\ (\text{SAGE \& GALLEX}) \quad : \quad \frac{\text{data}}{\text{SSM}_{\text{BP92}}} = 0.59 \pm 0.10, \quad (\text{eq 7-4})$$

where the statistical and systematic errors are combined in quadrature. The 90% C.L. allowed regions for both experiments are shown in Fig. 7.3 and 7.4.

Combining the results from all three types of experiments, we can obtain a 90% C.L. allowed region as shown in Fig. 7.5. The shaded area is also allowed [ref 7.1] due to regeneration in the earth which is neglected in the calculation (see also Fig. 3.4 for the excluded region due to the non-observed earth effect in Kamiokande by the study of day/night variation). There remain two allowed regions for the MSW mechanism. χ^2 has a minimum value of 7.9 at $(\delta m^2, \sin^2 2\theta) = (6.0 \times 10^{-6}, 6.7 \times 10^{-3})$ for the 10 data points (8 data points from the energy spectrum observed in Kamiokande, 2 data points from the chlorine (eq 7-3) and gallium (eq 7-4) experiments). The expected energy spectrum in Kamiokande for the typical parameters in those two regions,

$$(\delta m^2, \sin^2 2\theta) = (10^{-5.2}, 10^{-2.2}) \text{ and } (10^{-5.4}, 10^{-0.2}),$$

is shown in Fig. 7.6 together with the observed spectrum. In these calculations, we took into account the earth effect by approximating the electron number density in the earth as $N_e = N_A \times \frac{\rho}{2}$, where N_e is the electron number density (/cm³), $N_A = 6.022 \times 10^{23}$ (Avogadro's number) and ρ the density of matter in the earth [ref 7-2] (g/cm³) as shown in Fig. 7.7.

7.1.2. Just-so oscillation solution

As mentioned in section 3.1, neutrino oscillation in vacuum is also a possible solution of the solar neutrino problem. The parameter region effective for this

mechanism is $0.5 < \sin^2 2\theta \leq 1$ and $10^{-11.5} < \delta m^2 < 10^{-9}$. The matter effect is not important in this parameter region. The probability was averaged over the revolution radius of the earth which varies by $\pm 1.67\%$ around the average radius of 1.496×10^{11} m.

Fig. 7.8 shows the 90% C.L. allowed region from the Kamiokande result (eq 7-1). Considering the energy spectrum as explained in the previous subsection, the allowed regions become those in Fig. 7.9. $\chi^2_{\min} = 7.0$ with 8 data points in the region $(\delta m^2, \sin^2 2\theta) = (8.9 \times 10^{-11}, 0.6)$. The small flux observed by the chlorine experiment limits these parameters to a much smaller region as shown in Fig. 7.10. The p-p neutrinos, the main neutrino source for the gallium experiments, undergo many oscillation cycles on their way to the earth, and the oscillation probability is averaged out and becomes $\frac{1}{2}$ (eq 3-12). Then, the value of almost half of the expected flux obtained by the gallium experiments does not influence vacuum oscillations for large mixing as shown in Fig. 7.11 (almost the entire region is allowed in the figure). The overlap region of these three results is very small. If all experimental results are combined, the minimum χ^2 with 10 data points in this region becomes 13.5 with the parameters $(\delta m^2, \sin^2 2\theta) = (6.3 \times 10^{-11}, 0.85)$, while the minimum χ^2 in the MSW region was 7.9. Therefore, any region for this just-so oscillation is rejected at 90% C.L.

7.2. Hybrid Solution

The hybrid model, which is the combination of the MSW effect and magnetic interaction of neutrinos with the solar magnetic field, is expected to be able to explain both the solar neutrino deficit and the time variation of the flux. We explored a hybrid solution which can reproduce the time variation in the ^{37}Cl experiment and the lack of significant time variation in Kamiokande as well as the observed flux (eq 7-1), (eq 7-3), (eq 7-4) in three types of experiments, ^{37}Cl , Kamiokande and ^{71}Ga , simultaneously. We first describe the numerical calculation technique in subsection 7.2.1. Then, we study possible solutions in subsection 7.2.2 with the assumption that the neutrinos are

Majorana type, for which the magnitude of the transition magnetic moment is less restricted by the limit from astrophysical observations (see section 2.2).

7.2.1. Numerical calculation of neutrino propagation

(i) Input parameters and magnetic fields in the sun

As seen in the propagation equation (eq 3-45), we need to know the electron number density N_e , the neutron number density N_n and furthermore, a profile of the magnetic field (B) in the sun. The mass square difference δm^2 , neutrino mixing angle $\sin^2 2\theta$ and neutrino transition magnetic moment μ are the parameters we are going to explore. N_e and N_n in Fig. 7.12 were obtained from the solar evolution model, SSM(BP92) [ref 1-5]. The effect of the transition magnetic moment μ always appears as the combination with the magnetic field: μB_{sun} . Hence, we fixed the transition magnetic moment at a plausible value of $10^{-11} \mu_B$ (see section 2.2), where $\mu_B = e\hbar / 2m_e c = 5.788 \times 10^{-15}$ MeV / Gauss is a Bohr magneton, and only the magnetic field B was taken as a changeable input for the following argument. Unfortunately, we have sparse knowledge of the magnetic field in the sun, but there are some limits for the magnitude:

- (1) Magnetic strength in the convection zone should be larger than 1 kGauss in order for the measured value of a few kGauss at the sunspots to be generated.
- (2) Magnetic strength in the sun is limited to less than $0.8 \sim 2.0 \times 10^7$ Gauss by the existing observations of the depth and latitude dependence of solar rotation [ref 7-3].

Hence, a reasonable range of the magnitude would be

$$10^3 \text{ Gauss} < B_{\text{sun}} < 10^7 \text{ Gauss}, \quad (\text{eq 7-5})$$

though there is a report of possible evidence for a 2 ± 1 MGauss quadrupole toroidal field centered at 0.7 of the solar radius [ref 7-4]. The profile of the magnetic field is not yet established despite the fact that one has succeeded in reproducing the solar magnetic cycle by a numerical calculation of the solar interior [ref 7-5]. We then considered the three different magnetic profiles:

- (a) A flat magnetic field in the sun

$$B(r) = B_0 \quad (0 < r < 1), \quad (\text{eq 7-6})$$

- (b) A flat magnetic field only in the convection zone

$$B(r) = 0 \quad (0 < r < 0.65), \quad B(r) = B_0 \quad (0.65 \leq r < 1), \quad (\text{eq 7-7})$$

(c) An Akhmedov type profile (see Fig. 7.13) [ref 7-6]

$$B(r) = B_1 \left(\frac{0.1}{0.1 + r} \right)^2 \quad (0 < r < 0.65), \quad (\text{eq 7-8})$$

$$B(r) = B_0 \left\{ 1 - \left(\frac{r - 0.7}{0.3} \right)^2 \right\} \quad (0.65 \leq r < 1), \quad (\text{eq 7-9})$$

where r is the radius in units of $R_{\text{sun}} = 6.96 \times 10^8$ m and B_0 and B_1 are representative values of the magnetic strength in the convection zone and in the radiation zone. B_0 was scanned over 1k, 2k, 5k, 10k, 20k, 25k, 30k, 35k, 40k, 45k, 50k and 60 kGauss as a time-varying quantity (in combination with the fixed quantity of B_1 which has the various values of 100k, 300k, 1M, 3M, 10 MGauss for an Akhmedov type profile).

(ii) Neutrino production

The distribution of the neutrino production points depends on the neutrino production reactions as shown in Fig. 7.14 [ref 1-5]. Neutrinos were generated at 56 different points in the core region ($r < 0.35$) of the sun considering the production region particular for each reaction. The resonance point of the MSW effect takes place at the deep inner region if the parameters are in the adiabatic region. The production point of the neutrinos is crucial for the calculation for the gallium experiments, since the pp reaction takes place at a rather shallow part of the core. It is less crucial for the Kamiokande experiment which observes only ^8B neutrinos being produced at the quite deep region of the core.

The energy of the neutrinos was fixed at 1 MeV, because the energy contributing to the Hamiltonian (eq 3-45) appears always in the form, $\delta m^2/E$. The parameters $\sin^2 2\theta$ and δm^2 in the ranges 10^{-3} to 1 and $10^{-10.15}$ eV² to $10^{-3.65}$ eV² were searched for.

(iii) Neutrino propagation

The wave function of the neutrinos begins with

$$\phi_{\nu} = \begin{pmatrix} \nu_e \\ \nu_{\mu} \\ \bar{\nu}_e \\ \bar{\nu}_{\mu} \end{pmatrix} = \begin{pmatrix} 1 \\ 0 \\ 0 \\ 0 \end{pmatrix}, \quad (\text{eq 7-10})$$

at $t=0$. The neutrinos propagate following the equation, $i \frac{d}{dt} \phi = H \phi$ (see also (eq 3-45) for the Hamiltonian, H). We then must integrate the Hamiltonian along the path from the production point to the surface of the sun. Most of the CPU time is spent in these steps. When we used an orthogonalized matrix at each step instead of the flavor basis matrix, we could then achieve a speed up of the integration. In the case of an orthogonalized matrix, the integration step where the matrix can be considered constant can be kept large, contrary to the very small step (significantly smaller than the oscillation length) needed to integrate the unorthogonalized matrix. Suppose that the Hamiltonian $H(t)$ can be regarded as constant in a step Δt $\{H(t) \simeq H(t + \Delta t) = H_0\}$, then the propagation equation $i \frac{d}{dt} \phi(t) = H_0 \phi(t)$ can be easily solved, and the result is

$$\phi(t + \Delta t) = \phi(t) e^{-iH_0 \Delta t}, \quad (\text{eq 7-11})$$

where $H_0' = V H_0 V^{-1}$ is an orthogonal-matrix, V the rotation matrix, and $\phi'(t) = V \phi(t)$ is the eigen-vector. Then the wave function at $t = t + \Delta t$ can be obtained ($V(t + \Delta t) \simeq V(t)$ is also required),

$$\phi(t + \Delta t) = V^{-1} (V \phi(t) e^{-iH_0' \Delta t}). \quad (\text{eq 7-12})$$

The rotation matrix V can be numerically obtained by the following way:

(1) In the case of a 2×2 matrix, the rotation matrix is analytically obtained.

$$H = \begin{pmatrix} \alpha & \beta \\ \gamma & \delta \end{pmatrix} \Rightarrow V = \begin{pmatrix} \cos \theta & \sin \theta \\ -\sin \theta & \cos \theta \end{pmatrix}, \quad \text{where } \tan 2\theta = \frac{2\beta}{\alpha - \gamma}.$$

(2) In the case of a $n \times n$ matrix, procedure (1) is repeated for each element till the off-diagonal elements become zero.

$$H = \begin{pmatrix} H_{11} & & 0 \\ & \cdots & \\ 0 & & H_{nn} \end{pmatrix}$$

$$=V_N \dots \begin{pmatrix} \cos\theta_i & 0 & \sin\theta_i & 0 \\ 0 & 1 & 0 & 0 \\ -\sin\theta_i & 0 & \cos\theta_i & 0 \\ 0 & 0 & 0 & 1 \end{pmatrix} \dots V_1 H V_1^{-1} \dots \begin{pmatrix} \cos\theta_i & 0 & -\sin\theta_i & 0 \\ 0 & 1 & 0 & 0 \\ \sin\theta_i & 0 & \cos\theta_i & 0 \\ 0 & 0 & 0 & 1 \end{pmatrix} \dots V_N^{-1}, \quad (\text{eq 7-13})$$

then the rotation matrix,

$$V = \prod_{i=1}^N V_i. \quad (\text{eq 7-14})$$

is obtained.

We chose the step size of $1/5000 R_{\text{sun}}$. It is sufficiently small to trace the change of the propagation matrix ($1/1000 R_{\text{sun}}$ is actually acceptable), but it is enormously large in comparison with the step size used for the integration method without the matrix orthogonalization (much smaller step size than $10^{-5} R_{\text{sun}}$ is needed in the adiabatic region). In Fig. 7.15, neutrino propagation is shown for typical parameter sets.

By using the technique described above in our hybrid model calculation (the propagation matrix is 4×4 , but the actual matrix is 8×8 because the elements consist of real and imaginary parts), the calculation speed was ~ 2 propagation / sec with double precision calculation on a HP Apollo 9000/730.

(iv) Averaging probabilities

The probabilities of observing ν_α at time t (created as ν_e) are given by

$$P_\alpha(t) = \langle \nu_\alpha | \phi(t) \rangle. \quad (\text{eq 7-15})$$

These probabilities oscillate in time (distance) and the oscillation length is

$$L = \frac{4\pi E}{\delta m^2} = 2.48 \times \frac{E(\text{MeV})}{\delta m^2(\text{eV}^2)} \text{ [meter]}, \quad (\text{eq 7-16})$$

which is short in comparison with the change of the revolution radius of the earth ($\sim 5 \times 10^9$ m). Therefore, the phase information is smeared out for long time observation. The neutrino is traced only one oscillation length after exiting the surface of the sun and the probabilities are then averaged along the path: this is equivalent to the analytic result,

$$\langle P_e \rangle = \cos^2 2\theta \times P_e(t) + \frac{\sin^2 2\theta}{2} - \cos 2\theta \sin 2\theta [\text{Re}(\nu_e(t))\text{Re}(\nu_\mu(t)) + \text{Im}(\nu_e(t))\text{Im}(\nu_\mu(t))].$$

(v) Neutrino reactions in the detector

The consideration of the detector response is not needed for the radiochemical experiments. The capture rate R is simply derived by the integration,

$$R = \sum_i \left\{ \int_{E_{\text{th}}}^{E_{\text{max},i}} dE \int d\mathbf{r} \varphi_i(E) P_{\nu_e}(E, \mathbf{r}) \sigma(E) \rho_i(\mathbf{r}) \right\}, \quad (\text{eq 7-17})$$

where i is the suffix for 8 individual neutrino production reactions (pp, ^8B , ^{13}N , ^{15}O , ^{17}F , ^7Be , pep and hep), E the energy of neutrinos, E_{th} the threshold energy of the neutrino capture reaction, $E_{\text{max},i}$ the maximum neutrino energy generated by the i -th reaction, φ_i the neutrino flux predicted by the SSM, P_{ν_e} the probability that the neutrino is still ν_e (obtained by the above numerical calculations), σ the cross section of the neutrino capture reaction [ref 1-26], and $\rho(\mathbf{r})d\mathbf{r}$ the fraction of the neutrino production rate in the volume $d\mathbf{r}$ (\mathbf{r} runs over the core region where neutrino production reactions takes place).

In the Kamiokande case, all four types of neutrinos ($\nu_e, \nu_\mu, \bar{\nu}_e, \bar{\nu}_\mu$) interact with electron targets and the energy of the recoil electron distributes with the form of (eq 4-8). The total cross section on electrons is already shown in Fig. 4.1 as a function of neutrino energy, and the expected energy spectrum of the recoil electron is obtained by considering the different performance of the Kamiokande detector (see Fig. 4.15). The energy spectra are averaged with the weight of their data taking time.

7.2.2. Allowed region for the non-time-variation solution with a magnetic field

Let us put aside the problem of time variation for a moment. The regions shown in Fig. 7.16 and 7.17 are allowed at 90% C.L. for the two radio-chemical experiments (^{37}Cl and ^{71}Ga , respectively) to explain the solar neutrino deficit for each assumed magnetic profile and magnetic field strength. Fig. 7.18 shows allowed regions at 90% C.L. from Kamiokande considering the energy spectrum. The parameter region of

$\delta m^2 \sim 10^{-7} \text{ eV}^2$ is strongly influenced by the consideration of resonant spin flavor precession.

7.2.3. Allowed region of the hybrid solution

As seen in Fig. 7.16, 7.17 and 7.18, the shape of the allowed regions greatly changes at $\mu_\nu B_0 \geq 20 \text{ kGauss} \times 10^{-11} \mu_B$. Such a characteristic will be useful for an explanation of the time variation reported in the chlorine experiment. We first searched for a parameter region where the ^{37}Cl time variation can be reproduced. Then, possible solutions to satisfy the results from all the experiments (neutrino deficit and time variation) are obtained.

(i) Region where the time variation can occur in the ^{37}Cl experiment

We have parametrized the observed time variation with the linear function of sun-spot numbers (eq 6-10). On the other hand, we calculated the solar neutrino flux for various configurations of the magnetic field in the sun. But, we do not even know the relation between the magnitude of the magnetic field in the convection zone B_0 and sun-spot numbers N_{ss} . Hence, we selected all possible combinations of $B_{0\text{min}}$ and $B_{0\text{max}}$ which were supposed to represent the strength of the magnetic field at a solar minimum ($N_{ss,\text{min}} \sim 20$) and at a solar maximum ($N_{ss,\text{max}} \sim 150$).

We have determined a correlation function between solar neutrino flux and sun-spot numbers to evaluate the time variation:

$$R = \frac{\text{expected}}{\text{SSM}} = \alpha N_{ss} + \beta, \quad (\text{eq 7-18})$$

where the coefficient α is obtained by

$$\alpha = \frac{R(B_{0\text{min}}) - R(B_{0\text{max}})}{N_{ss,\text{min}} - N_{ss,\text{max}}} = \frac{R_{\text{min}} - R_{\text{max}}}{20 - 150}, \quad (\text{eq 7-19})$$

$$R(R_{0\text{min}}) = R_{\text{min}}, R(B_{0\text{max}}) = R_{\text{max}}$$

and β is obtained by

$$\beta = R_{\text{min}} - \alpha \times 20. \quad (\text{eq 7-20})$$

This correlation function is obtained for every oscillation parameter ($\sin^2 2\theta, \delta m^2$). The confidence level of these parameter sets (α, β) in the linear fit is derived by χ^2 test with the 92 observed data points in comparison with the χ^2 value of 92.34 which corresponds to the best fit of the reported time variation (eq 6-10). Fig. 7.19 shows the ($\sin^2 2\theta, \delta m^2$) region where at least one parameter set (α, β) is allowed at 90% C.L. for several configurations of the magnetic field. The strength of the magnetic field (B_0) at the solar minimum and at the solar maximum is ranging between about 20 kGauss and 50 kGauss for those allowed sets of (α, β).

(ii) Region where the observable flux with ^{71}Ga is kept at a high value

The average sun-spot numbers for the period the ^{71}Ga experiments have been taking data are the following [ref 6-2]:

| | | |
|----------|-----------------|-----------------------------------|
| SAGE-30 | '90/1 to '91/7 | $\langle N_{ss} \rangle \sim 120$ |
| SAGE-60 | '91/8 to '91/12 | $\langle N_{ss} \rangle \sim 140$ |
| GALLEX-1 | '91/6 to '92/4 | $\langle N_{ss} \rangle \sim 140$ |
| GALLEX-2 | '92/8 to '93/4 | $\langle N_{ss} \rangle \sim 75$ |

The first three experiments took data during the solar maximum period (N_{ss} are large), and GALLEX-2 data was taken in the period when sun-spot numbers had started to decrease. To simplify the situation we have used the combined flux from the first three experiments,

$$\frac{\text{data}}{\text{SSM}} = 0.55 \pm 0.11, \quad (\text{eq 7-21})$$

as the flux at the solar maximum period when the assigned magnetic field is $B_{0\text{max}}$. Fig. 7.20 shows the 90% C.L. allowed region of the gallium experiments where it is further limited to the region which overlaps with that already obtained for the chlorine experiment. The allowed region has moved outside of the MSW triangle. Fig. 7.21 shows the time variation of the neutrino flux for the ^{37}Cl and ^{71}Ga experiments in terms of the magnetic field for typical parameters in the allowed region.

(iii) Region where the Kamiokande result is also satisfied

The Kamiokande result does not show any significant time variation in correlation with sun-spot numbers. This outcome must be satisfied.

The expected time variation of a hybrid model in Kamiokande is calculated by

$$R_{\text{kam}} = \alpha_{\text{kam}} N_{\text{ss}} + \beta_{\text{kam}}, \quad (\text{eq 7-22})$$

where R_{kam} is the expected ratio, and α_{kam} and β_{kam} are obtained by

$$\alpha_{\text{kam}} = \frac{R_{\text{kam}}(B_{0\text{min}}) - R_{\text{kam}}(B_{0\text{max}})}{20 - 150}, \quad \beta_{\text{kam}} = R_{\text{kam}}(B_{0\text{min}}) - \alpha \times 20. \quad (\text{eq 7-23})$$

The relation (eq 7-22) is also checked for each oscillation parameter set by the χ^2 test defined in (eq 6-12) for the 7 data points from different data taking periods. If the χ^2 is allowed at 90% C.L., the input configuration of magnetic field and parameters $\mu_{\nu} B$, $\sin^2 2\theta$ and δm^2 was regarded as an allowed parameter set for the Kamiokande result.

The regions of 90% C.L. allowed points simultaneously satisfying both the Kamiokande and chlorine experiments are shown in Fig. 7.22. The expected time variations of these experiments with typical parameters in that region are shown in Fig. 7.23. The event rate of the gallium experiments tends to be small in these regions.

The regions where the three types of experiments are simultaneously satisfied are limited to the small areas shown in Fig. 7.24. The regions are

$$(s1) \sin^2 2\theta \sim 1, \quad \delta m^2 \sim 2 \times 10^{-9} \text{ eV}^2$$

for an Akhmedov type profile with $B_1 \leq 1$ MGauss (assuming $\mu_{\nu} = 10^{-11} \mu_B$),

$$(s2) \sin^2 2\theta \sim 0.01, \quad \delta m^2 \sim 6 \times 10^{-8} \text{ eV}^2$$

for an Akhmedov type profile, but with $B_1 \sim 3$ MGauss,

$$(s3) \sin^2 2\theta \leq 6 \times 10^{-2}, \quad \delta m^2 \sim 10^{-8}$$

for a profile where the magnetic field is flat at $0.65 < r/R_{\text{sun}} < 1$, and zero at $r/R_{\text{sun}} < 0.65$,

$$(s4) \sin^2 2\theta \leq 3 \times 10^{-2}, \quad \delta m^2 \sim 10^{-8}$$

for a profile where the magnetic field is flat in the sun, $0 < r/R_{\text{sun}} < 1$.

These parameter regions require a change of magnetic field in the convection zone from about 20 kGauss (at solar minimum) to 50 kGauss (at solar maximum) in order to vary

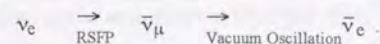
the solar neutrino flux sufficiently for the ^{37}Cl experiment. Expected time variations with typical parameters in those regions are shown in Fig. 7.25.

We found that if we assume an Akhmedov type profile of the solar magnetic field, the possible solutions are limited to a very small region and a large mixing angle ($\sin^2 2\theta \sim 1$, $\delta m^2 \sim 2 \times 10^{-9} \text{ eV}^2$) seems to be favored. We must note that a large mixing solution creates a large amount of $\bar{\nu}_e$, and the $\bar{\nu}_e$ flux limit obtained by Kamiokande may be able to exclude the region. If we suppose a flat profile of the magnetic field, an allowed region appears around $\sin^2 2\theta < 0.1$ and $\delta m^2 \sim 10^{-8} \text{ eV}^2$. In [ref 1-32], which assumes a flat magnetic field in the sun, an allowed region for the chlorine and Kamiokande results is indicated around $\sin^2 2\theta \sim 0.2$ and $\delta m^2 \leq 10^{-7}$ (see Fig. 7.26), and they claim that the neutrino flux for gallium becomes so small in this region that none of the parameters can satisfy all the experimental results. This is inconsistent with our results. The difference seems to arise from the fact that we have chosen the best fit function for the time variation of the chlorine experiment to match the central value derived by the experimental group.

The neutrino spectrum and its time variation depends on the configuration of the magnetic field and, therefore, if the hybrid model is the right solution, we will be able to probe the profile of the magnetic field in the sun with neutrino observations.

7.3. Implication of the $\bar{\nu}_e$ flux limit to the hybrid solution7.3.1. $\bar{\nu}_e$ creation in the hybrid model

Possible solutions to the neutrino deficit and the time variation were found in the framework of the hybrid model as shown in the previous subsection. There is an allowed region at large mixing angle $\sin^2 2\theta \sim 1$ and with $\delta m^2 \sim 2 \times 10^{-9} \text{ eV}^2$ for a particular profile of the solar magnetic field. With such parameters, a large amount of $\bar{\nu}_e$ creation could take place as seen in Fig. 7.27 through the process:



Kamiokande has an ability to observe those $\bar{\nu}_e$ very efficiently because of the large cross section of $\bar{\nu}_e$ on protons (eq 4-21). We calculated the expected number of $\bar{\nu}_e$ events in Kamiokande for various configurations of the solar magnetic field. Fig. 7.28 shows the expected number of events per day (passing all the selection criteria) above 13 MeV of positron energy, where the observed event rate was 16 events / 594 days. When the strength of the magnetic field in the radiation zone is large ($\mu_\nu B_1 \geq 1$ MGauss $\times 10^{-11} \mu_B$), $\bar{\nu}_e$ are efficiently created due to spin flavor precession in the radiation zone (see Fig. 7.29) for the parameter range of $10^{-7} \leq \delta m^2/E \leq 10^{-4}$ (eV²/MeV), $10^{-1.2} \leq \sin^2 2\theta \leq 10^{-0.5}$. For the case of the parameter region $\delta m^2/E \leq 10^{-7}$ (eV²/MeV), $\sin^2 2\theta \geq 10^{-1.5}$, spin flavor precession occurs mostly in the convection zone (see Fig. 7.27), and a large amount of $\bar{\nu}_e$ creation can be expected with $\mu_\nu B_0 \geq 20$ kGauss $\times 10^{-11} \mu_B$.

7.3.2. Excluded region of hybrid model

We obtained a spectrum independent but conservative flux limit on $\bar{\nu}_e$ at each energy point in section 6.4. We found some possible parameter sets ($\mu_\nu B_{\text{sun}}$, $\sin^2 2\theta$, δm^2) with which all the experimental results, including both neutrino deficit and time variation, can be explained simultaneously. There is a large mixing solution where a large amount of $\bar{\nu}_e$ creation is expected. Hence, the $\bar{\nu}_e$ flux limit in the parameter space of $\mu_\nu B_{\text{sun}}$, $\sin^2 2\theta$, δm^2 will be important information in order to find the right solution. We used the data from Kam-2 gain $\times 2$ in order to limit the parameter space. The average sun-spot number for this period was about 145, and the limit from the data can be regarded as that for a solar maximum period.

The spectrum independent $\bar{\nu}_e$ flux limit gives most the strict value, $4.5\% \times \text{MeV}$ (unit of MeV represents the width of the $\bar{\nu}_e$ energy distribution), at 12.5 MeV with respect to the ⁸B solar neutrino flux of the SSM prediction. But if we once fix the parameters $\mu_\nu B_{\text{sun}}$, $\sin^2 2\theta$, δm^2 , we can derive the expected energy spectrum of positrons which are created by the $\bar{\nu}_e p \rightarrow e^+ n$ reaction, then we can utilize the spectrum information to obtain the $\bar{\nu}_e$ limits. We can therefore obtain a much stricter limit such as

an $O(1\%)$ transition of ⁸B neutrino to $\bar{\nu}_e$. Expected energy spectra with typical parameters are shown in Fig. 7.30. Fig. 7.31 shows exclusion regions (90%C.L.) in the $\sin^2 2\theta$ vs. δm^2 plane for various configurations of solar magnetic field.

The resulting excluded region is slightly influenced by the profile of the magnetic field. They are

$$(e1) 10^{-7} \leq \delta m^2 \leq 10^{-4}, 10^{-1.4} \leq \sin^2 2\theta \leq 10^{-0.4}$$

$$\text{with } B_1 \geq 3 \text{ MGauss } (\mu_\nu = 10^{-11} \mu_B), \text{ and}$$

$$(e2) \sin^2 2\theta \geq 10^{-1.5}, \delta m^2 \leq 10^{-6.5}$$

$$\text{with } B_0 \sim 50 \text{ kGauss.}$$

The excluded region (e2) depends only on the strength of magnetic field in the convection zone which is essential for inducing the time variation of neutrino flux. We can give an exclusion region when B_0 is greater than about 20 kGauss. All hybrid solutions obtained in subsection 7.2.3 requires larger magnetic strength than 20 kGauss. The excluded region (e2) covers almost the whole area obtained in reference [ref 1-32] (Fig. 7.26), in which the chlorine and Kamiokande results but not gallium results are explained at the same time. The $\bar{\nu}_e$ flux limit (e2) also reject the large mixing solution (s1) obtained in the previous section. Therefore, the remaining allowed regions are the small mixing solutions (s2), (s3) and (s4).

References

- [7-1] A.Yu.Smirnov, Proceedings of the International Symposium on Neutrino Astrophysics, Takayama/Kamioka, Japan, 1992, p105, edited by Y.Suzuki and K.Nakamura (Universal Academy Press, Inc. Tokyo, Japan 1993).
- [7-2] T.H.Jordan and D.L.Anderson, Geophys.J.R.Astro.Soc. **36**(1974)411.
- [7-3] T.M.Brown and C.A.Murrow, Astrop.J.Lett. **314**(1987)L21; A.B.Balantekin, P.J.Hatchell and F.Loreti, Phys.Rev. **D41**(1990)3583.
- [7-4] W.A.Dziembowski and P.R.Goode, Proceedings of the 121st Colloquium of the International Astronomical Union "Inside the Sun", Versailles, France, May 1989, p341, edited by G.Berthomieu and M.Cribier (Kluwer Academic Publishers, 1990).
- [7-5] H.Yoshimura, Astrop.J.Suppl. **52**(1983)363.

8. Conclusion & Summary

The Kamiokande solar neutrino observation entered into a new phase called Kamiokande-3 in December 1990. The performance of the detector was improved by new electronics, light reflectors and a new radon free air system (see chapter 4). Due to this improvement, the threshold energy for the solar neutrino observation was lowered to 7.0 MeV as of November 1991. The solar neutrino measurement extended up to 514 days, and the observation period has covered an entire solar maximum period. The solar neutrino flux obtained by Kamiokande-3 (section 6.1),

$$\frac{\text{data}}{\text{SSM}_{\text{BP92}}} = 0.574^{+0.064}_{-0.059} \pm 0.061,$$

is consistent with the previous Kamiokande-2 result. The combined result from 1557 days of data is

$$\frac{\text{data}}{\text{SSM}_{\text{BP92}}} = 0.514^{+0.043}_{-0.037} \pm 0.061.$$

This ratio corresponds to $439^{+36.6}_{-31.4}$ solar neutrino events in 1557 days of observation. All four ongoing solar neutrino experiments, Chlorine, Kamiokande, SAGE and GALLEX have reported neutrino deficits. This solar neutrino problem is difficult to explain by any SSM modifications (section 1.4). Neutrino oscillation solutions are possible explanations of the problem. The allowed MSW parameter regions where all of the solar neutrino measurements, including the energy spectrum observation by Kamiokande, can be explained are limited to two separated areas around $(\sin^2 2\theta, \delta m^2 [\text{eV}^2]) = (10^{-2.1}, 10^{-5.3})$ and $(10^{-0.1}, 10^{-5.3})$. The just-so solution of neutrino oscillations has been ruled out at 90% C.L. (section 7.1).

The time variation of the neutrino flux observed by the Chlorine experiment was parametrized as a the linear function of the sun-spot numbers (section 6.3),

$$\frac{\text{data}}{\text{SSM}_{37\text{Cl}}} = (-0.90 \pm 0.34) \times 10^{-3} N_{\text{SS}} + (0.369 \pm 0.045),$$

and the significance level was found to be 2.7σ . If one takes this correlation positively, it requires, for example, a neutrino (transition) magnetic moment as large as $\sim 10^{-11}\mu_B$.

The same relation obtained from Kamiokande for all the available data is

$$\frac{\text{data}}{\text{SSM}_{\text{kam}}} = (-0.21^{+1.02}_{-1.05}) \times 10^{-3} N_{\text{ss}} + (0.536^{+0.140}_{-0.128})$$

and that for 9.3 MeV common threshold is

$$\frac{\text{data}}{\text{SSM}_{\text{kam}}} = (-0.57^{+1.07}_{-1.08}) \times 10^{-3} N_{\text{ss}} + (0.534^{+0.141}_{-0.133})$$

These results are consistent with no correlation.

A spectrum independent solar $\bar{\nu}_e$ flux limit (see Fig. 6.12) taking advantage of the large cross section of $\bar{\nu}_e$ on proton targets was given in this thesis for the first time. The flux limit was compared to the ^8B solar neutrino flux, and the most strict limit (but a conservative limit) was obtained as (section 6.4)

$$\left. \frac{\phi(\bar{\nu}_e)}{\phi_{\text{SSM}}(\nu_{^8\text{B}})} \right|_{E_{\nu}=12.5\text{MeV}} < 4.5\% \times \text{MeV}.$$

If we assume a specific mechanism such as a hybrid model of $\bar{\nu}_e$ creation, then we can calculate the energy spectrum of $\bar{\nu}_e$. In this case, we can reject more than a 1% transition of ^8B neutrinos to $\bar{\nu}_e$ (section 7.3).

The most plausible approach to explain both the time variation and the deficit of the solar neutrino flux is a hybrid model. An extensive study on this aspect was undertaken in this thesis and the results of the solar $\bar{\nu}_e$ limits were used as a valuable input for this study.

A transition magnetic moment of a Majorana neutrino is less restricted than that of a Dirac neutrino and the required value to explain the solar neutrino problem seems not to contradict the upper limits deduced from terrestrial experiments and astrophysical observations (section 2.2). Hence, we studied hybrid solutions (section 7.2) with the assumption of Majorana neutrinos. We found the parameters with which all the experimental data (the neutrino deficit in the ^{37}Cl , Kamiokande and ^{71}Ga experiments

along with the time variation in the ^{37}Cl experiment and the lack of time variation in Kamiokande) are satisfied. The parameters obtained are:

$$(s1) \sin^2 2\theta \sim 1, \delta m^2 \sim 2 \times 10^{-9} \text{ eV}^2$$

for an Akhmedov type profile with $B_1 \leq 1$ MGauss (assuming $\mu_{\nu} = 10^{-11}\mu_B$),

$$(s2) \sin^2 2\theta \sim 0.01, \delta m^2 \sim 6 \times 10^{-8} \text{ eV}^2$$

for an Akhmedov type profile, but with $B_1 \sim 3$ MGauss,

$$(s3) \sin^2 2\theta \leq 6 \times 10^{-2}, \delta m^2 \sim 10^{-8}$$

for a profile where the magnetic field is flat at $0.65 < r/R_{\text{sun}} < 1$, and zero at $r/R_{\text{sun}} < 0.65$,

$$(s4) \sin^2 2\theta \leq 3 \times 10^{-2}, \delta m^2 \sim 10^{-8}$$

for a profile where the magnetic field is flat in the sun, $0 < r/R_{\text{sun}} < 1$.

These parameter regions require the change of magnetic field in the convection zone from about 20 kGauss (at solar minimum) to 50 kGauss (at solar maximum) in order to obtain sufficient time variation of the solar neutrino flux.

Hybrid models with Majorana type neutrinos generate $\bar{\nu}_e$ through the process,

$$\nu_e \xrightarrow{\text{RSFP}} \bar{\nu}_\mu \xrightarrow{\text{Vacuum Oscillation}} \bar{\nu}_e$$

This $\bar{\nu}_e$ creation is efficient when the mixing angle is large and the magnetic field is larger than ~ 20 kGauss (assuming $\mu_{\nu} = 10^{-11}\mu_B$): the hybrid solution (s1) satisfies the above condition. We gave excluded regions in the parameter space ($\mu_{\nu} B_{\text{sun}}, \sin^2 2\theta, \delta m^2$) from the $\bar{\nu}_e$ flux limit of Kamiokande (section 7.3):

$$(e1) 10^{-7} \lesssim \delta m^2 \lesssim 10^{-4}, 10^{-1.4} \lesssim \sin^2 2\theta \lesssim 10^{-0.4}$$

with $B_1 \geq 3$ MGauss ($\mu_{\nu} = 10^{-11}\mu_B$), and

$$(e2) \sin^2 2\theta \geq 10^{-1.5}, \delta m^2 \leq 10^{-6.5}$$

with $B_0 \sim 50$ kGauss.

The excluded region in (e2) comes to appear when $B_0 \geq 20$ kGauss.

Region (e2) includes region (s1), and therefore, the large mixing solution (s1) is rejected by the $\bar{\nu}_e$ flux limit from Kamiokande. The remaining hybrid model solutions are small mixing (s2), (s3) and (s4).

...the first of the ... the second ... the third ... the fourth ... the fifth ... the sixth ... the seventh ... the eighth ... the ninth ... the tenth ...

...the first of the ... the second ... the third ... the fourth ... the fifth ... the sixth ... the seventh ... the eighth ... the ninth ... the tenth ...

...the first of the ... the second ... the third ... the fourth ... the fifth ... the sixth ... the seventh ... the eighth ... the ninth ... the tenth ...

...the first of the ... the second ... the third ... the fourth ... the fifth ... the sixth ... the seventh ... the eighth ... the ninth ... the tenth ...

...the first of the ... the second ... the third ... the fourth ... the fifth ... the sixth ... the seventh ... the eighth ... the ninth ... the tenth ...

...the first of the ... the second ... the third ... the fourth ... the fifth ... the sixth ... the seventh ... the eighth ... the ninth ... the tenth ...

Appendix A Plots for Kashiokanda 3

...the first of the ... the second ... the third ... the fourth ... the fifth ... the sixth ... the seventh ... the eighth ... the ninth ... the tenth ...

...the first of the ... the second ... the third ... the fourth ... the fifth ... the sixth ... the seventh ... the eighth ... the ninth ... the tenth ...

...the first of the ... the second ... the third ... the fourth ... the fifth ... the sixth ... the seventh ... the eighth ... the ninth ... the tenth ...

...the first of the ... the second ... the third ... the fourth ... the fifth ... the sixth ... the seventh ... the eighth ... the ninth ... the tenth ...

Appendix A. PMTs for Kamiokande-II

The 20 inch-diameter photo-multiplier tube (20" ϕ PMT) used in the Kamiokande detector was specially developed by Hamamatsu Photonics Co. in cooperation with some members of the Kamiokande collaboration [ref A-1]. This large PMT enable us to obtain a large photosensitive coverage ($\sim 20\%$) with a relatively small number of PMTs. This development was essential for performing solar neutrino observation with the water Cherenkov detector.

The structure of the 20" ϕ PMT is shown in Fig. A.1. The structure and the arrangement of the focusing electrode were carefully designed on the basis of an electron trajectory simulation to optimize both the transit time spread and the photoelectron collection efficiency at the same time.

The electron trajectories shown in Fig. 4.6 are examples of the computer simulation with a voltage bias of 800 V between the cathode and the focusing electrode. The voltage divider was designed to provide sufficient gain and good photoelectron collection efficiency even under the weak magnetic field of the earth.

Fig. A.2 shows the spectral dependence of its quantum efficiency, which exhibits the typical characteristics of a bi-alkali photo-cathode. The Cherenkov light spectrum (with the peak normalized to 100%) after traversing 15 m of pure water is also shown in the same figure. The wave length at the peak quantum efficiency is well matched to the Cherenkov radiation spectrum. The uniformity of the photo-cathode quantum efficiency (called the cathode uniformity) is reasonably flat. The pulse height of the output signal, however, depends on the position of the incident light at the photo-cathode surface (called the anode uniformity) as shown in Fig. A.3.

The time response of the PMT is very good in spite of the long distance between the photo-cathode and the first dynode. The transit time spread (1σ) is 4.7 nsec at 1 p.e. for a typical PMT.

The effect of a magnetic field on the PMT gain (see Fig. A.4) cannot be avoided. The existence of a magnetic field (of the order of several hundred mGauss) is a serious problem for the $20^\circ\phi$ PMT, because of the long distance between the photo-cathode and the first dynode. Therefore, we tried to eliminate the geomagnetic field (0.45 gauss) by the following two methods:

- A compensation coil surrounding the detector was arranged as shown in Fig. A.5 for a global cancellation of the magnetic field. The typical strength of the geomagnetic field near a PMT was reduced to 0.1 gauss;
- Each PMT is shielded with a μ -metal (78% Ni) mesh (which causes 13% absorption of the incident light) in front and with a cone-shape μ -metal plate at the back as shown in Fig. A.6. This combination of shields suppresses the magnetic field by a factor of 3 to 8, depending on the relative orientation of the PMT with respect to the geomagnetic field.

The resultant magnetic field inside the PMT is less than 0.03 gauss. The effect of the residual magnetic field is, then, negligible as seen in Fig. A.4.

The gain of the PMT has been monitored using the light output of penetrating muons, and it has been stable within $\pm 3\%$ for more than 6 years.

Since the PMTs are placed in water for long time, they must be waterproof. The PMT base is surrounded by a PVC pipe and filled with polyurethane (see Fig. A.7). Two coaxial cables, one for the H.V. and the other for the signal, are waterproofed by using a small PVC pipe tightened by a heat-shrinking tube at the connection to the base.

Each PMT of the inner detector is held by a housing that is attached to the support frame on the inner surface of the water tank as shown in Fig. A.8. The PMT housing is made by two stainless steel belts with neoprene rubber to support the PMT onto a 1 m \times 1 m stainless frame. The support frame, which is designed by considering the centers of buoyancy and mass, is bolted to the tank at the barrel every 1 m in the horizontal

direction and every 3 m in the vertical direction, at the top every 3 m and 1 m in perpendicular directions, and at the bottom every 2 m and 1 m in perpendicular directions. The top and bottom sections accommodate 164 and 160 PMTs, respectively, and the spacing is exactly 1 m between adjacent PMT in rows and columns. The barrel section accommodates 624 PMTs (13 in column by 48 in row) with a spacing of 0.945 m between PMTs in adjacent columns and 1 m between PMTs in adjacent rows.

References

- [A-1] H.Kume et al., NIM 205(1986)443.

Appendix B. Electronics for Kamiokande-II

For Kamiokande-II [ref 4-3,B-1], the signal was divided into two: one was fed to the electronics which had been used for Kamiokande-I, and the other to that for the Kam-2. In the solar neutrino observation, timing information is crucial. The block diagram of the signal flow is shown in Fig. B.1.

The special features of the Kamiokande-II electronics are

- low noise for one photo-electron counting (the threshold could be set to ~ 0.35 p.e. and finally to ~ 0.18 p.e. after the gain doubling),
- 4 depth analog memory capacitors for both timing and charge measurement aiming at being dead time free (the single channel dead time is 800 nsec after a signal detection),
- 1 nsec precision for the timing information with a 10-bit full scale,
- 0.1 p.e. (gain $\times 1$) precision for the pulse height measurement with a 14-bit full scale,
- 44-bit clock which can record the global trigger time with the precision of 20 nsec,
- on-line controllable discriminator for each channel (0.1 p.e. to 3 p.e. for gain $\times 1$ with 6-bit full scale),
- 6 channels of global trigger inputs which can be separately enabled or disabled under computer control, and
- 8-bit trigger identification so as not to mix up the data from different physical events.

The electronics consists of 272 front end cards (FEC), 16 control cards (CC), 15 trigger processing cards and one timing card. There were 15 crates for the inner detector and 2 crates for the anti-counter. Every crate for the inner counter contains 16 FECs, 1 CC and 1 trigger processing card, while the crate for the anti-counter contains 16 FECs,

and only one CC for the two crates. A FEC can process four channels of signals. The function of each card is given below.

◆ Front end card (FEC):

A FEC processes signals from 4 PMTs. It splits the PMT signal into two. One of them is sent to the Kamiokande-I electronics which has only ADC information and is not used for this analysis. Another one is amplified and discriminated with the threshold of ~ 0.35 p.e. for gain $\times 1$ set by a computer with a 6-bit full scale (0.1 to 3 p.e. for gain $\times 1$) DAC. If the input signal exceeds the threshold, digital (100 nsec in width and ~ 5 mV in height) and analog signals are transmitted to the trigger card. The FEC integrates the charge of the input signal for the pulse-height measurement, and constantly charges up the capacitor for the timing measurement until the global trigger distributed from the trigger card stops it. If the global trigger does not arrive within 400 nsec after the discrimination, it needs an additional 400 nsec to reset the capacitors. If the global trigger occurs, then the FEC holds the voltages for charge and time information on one of four sets of analog memories until the CC in the same crate digitizes them. The FEC loads the trigger identification from the trigger card through the CC and holds it until the CC reads it. The linearity of the data is kept up to 400 nsec and 800 p.e. (gain $\times 1$) within 1% of the full scale.

◆ Control card (CC):

A CC scans 16 FECs (64 channels) in the same crate and digitizes the time and charge with 10-bit and 14-bit full scales, if they exist. It takes about 2.7 msec to scan all the FECs and takes about 50 μ sec for one charge digitization. The CC loads the trigger ID from the FEC and stores it in a 8-bit \times 512 FIFO memory with the digitized data. It needs 6 bytes for a hit. The CC distributes the new trigger ID, which is counted up by the timing card for next event, to the FECs. The stored data are read out asynchronously by the on-line computer.

◆ Trigger card:

A trigger card sums up the discriminator outputs from 64 channels in the same crate. One hit corresponds to about 5 mV. Then, the master trigger card performs the

total sum of the signals from the 15 trigger cards. If the total sum exceeds the preset master threshold (~ 112 mV), the trigger is fed into the timing card which generates a global trigger.

◆ Timing card:

The timing card receives the trigger signal from the master trigger card and distributes the trigger to the FECs, the CCs and so on. It records the time with the precision of 20 nsec (44-bit full width), the trigger ID and the trigger mode onto FIFO memories (two fast 8-bit \times 64 word memories arranged in parallel). Then, the timing card counts up the trigger ID (8-bit) for the next event. The event time can be counted up to 9.77 hours with the 44-bit counter.

References

[B-1] S.B.Kim, Ph.D.thesis, Univ.of Pennsylvania (1989).

Appendix C. Calibration & Stability Check

C.1. Energy Calibration

Energy measurement is an advantage of the Kamiokande detector. The energy spectrum of the solar neutrinos can be tested through a measurement of that of the recoil electrons from $\nu_e e^-$ elastic scattering. In the case of $\bar{\nu}_e$ observation by $\bar{\nu}_e p \rightarrow e^+ n$ interaction, we can obtain an incident neutrino energy on an event by event basis through the relation $E_{e^+} = E_{\bar{\nu}_e} - 1.293$ MeV. This ability makes Kamiokande sensitive to possible $\bar{\nu}_e$ creation in the sun as expected in a certain hybrid model.

It is, therefore, important to calibrate the absolute energy scale of the detector in either case.

We have frequently performed precise calibrations of the absolute energy scale with gamma rays emitted from $\text{Ni}(n,\gamma)\text{Ni}'$ reaction; the energy is similar to that of solar neutrinos. Additional energy calibrations in the different energy regions were also performed with spallation products and with electrons from μ -e decays.

C.1.1. $\text{Ni}(n,\gamma)\text{Ni}'$ calibration

The most precise calibration of the absolute energy scale has been done using gamma rays from a neutron capture reaction of nickel nuclei. A schematic view of the calibration source is shown in Fig. C.1. This calibration was also used for the adjustment of detector parameters used in the Monte Carlo simulation as described in subsection 5.2.3.

We used natural nickel for the calibration, for which the abundance is ^{58}Ni : 68.27%, ^{60}Ni : 26.10%, ^{61}Ni : 1.13%, ^{62}Ni : 3.59% and ^{64}Ni : 0.91%. Their capture cross sections for thermal neutrons are 4.4, 2.6, 2.0, 15 and 1.52 barn, respectively. They emit gamma rays with the energies of 9.0, 7.8, 10.6, 6.8 and 6.1 MeV, respectively.

Energy levels of each gamma ray emission are shown in Fig. C.2. The major branch of the capture emits a 9.0 MeV gamma ray with the branching ratio of 26%.

A ^{252}Cf fission source is used as the neutron source. ^{252}Cf has a half life of $T_{1/2}=2.65\text{y}$ and disintegrates through α -decay (96.9%) and fission (3.1%). It emits 3.76 neutrons in a fission with an average energy of about 2 MeV. The neutrons get thermalized after an average of 19 scatterings off of protons in the water and travel about 2 cm over a few micro seconds during these thermalization processes. The capture cross section on a proton is 0.33 barn and the mean life in water is about 200 μsec . The thermalized neutrons diffuse about 3 cm before a capture takes place. We used 97 μCi (4.2×10^5 n/s) and 150 nCi (6.5×10^2 n/s) sources for the calibration.

The ^{252}Cf fission source is placed at the center of the cylindrical neutron converter made of Ni with 0.1 cm thickness. The size of the converter is 9.5 cm in diameter and 16 cm in height. The inside of the converter is naturally filled with pure water when immersed in the water tank, which works as a moderator of the fission neutrons (hereafter Ni-Cf γ -source). About one tenth of the neutrons are captured by the Ni with this configuration. This high-rate-source can provide high statistics and a precise calibration of the absolute energy scale.

The energy spectrum obtained by the Ni-Cf source is shown in Fig. C.3. The Ni-Cf source contains some backgrounds such as low energy gamma rays from fission itself and from the $p(n,\gamma)\text{D}$ reaction which emits 2.2 MeV gamma rays. We used data taken without the Ni converter in order to subtract their contributions. When we take the background data, we must consider the distortion of the energy spectrum which is caused by the beta ray emitted from the fission products and the Compton scattering of gamma rays by the moderating water and by the fact that the removal of the Ni converter makes the Cherenkov emission in the region near the source more likely to be seen by the PMTs. We avoided these distortions by using the same size polyethylene container instead of the Ni converter in measuring the background.

The background subtraction is the main source of the systematic error for this calibration. The background spectrum is monotonously decreasing as a function of

energy as seen in Fig. C.4. Hence, when we subtract the background spectrum, if the background is overestimated then the peak value of the $\text{Ni}(n,\gamma)\text{Ni}'$ spectrum will be shifted to a larger value, and if underestimated then the peak will become lower. The calibration-runs were taken at a very low energy threshold (about 2.5 MeV) and the trigger rate was so high that the dead time was rather large. It makes it difficult to obtain the exact run-time; a 0.5% shift of the peak is caused by a 4% error of the run-time estimation. We avoided this difficulty by counting up the muon event rate, being considered as constant for a short calibration time (a few hours), and we were able to calculate the run time with about 2% accuracy. This corresponds to 0.25% systematic error for the calibration.

The alternative way to subtract the background spectrum is to adjust the shape of the Ni+Cf data and the Ni(M.C.)+Cf data (this means the normalization factor of the background spectrum is treated as free parameter), which was adopted for the Kamiokande-II analysis. From the difference between the muon counting method and the shape adjustment method, we estimated the systematic error to be less than 0.5%. Fig. C.5 shows the energy spectrum of the $\text{Ni}(n,\gamma)\text{Ni}'$ reaction which is obtained by subtracting the spectrum in Fig. C.4 from that in Fig. C.3 after the normalization.

The long time stability of the detector is important in studying time variations such as an anti-correlation of neutrino flux with sunspot numbers. The stability of the detector is regularly checked by the total number of photo-electrons of penetrating muons. This process is much higher than the solar neutrino energy. The frequent calibrations with the $\text{Ni}(n,\gamma)\text{Ni}'$, which represents the low energy response of the detector, are also used to study the long term stability. The stability of the Kamiokande detector has been found to be within $\pm 2.3\%$ throughout all of the observation time; Kam-2 (gain $\times 1$), Kam-2 (gain $\times 2$) [ref 1-8] and Kam-3 as shown in Fig. C.6. We must note that a 1% uncertainty in the absolute energy scale results in 5%, 3% or 2% systematic errors on the solar neutrino flux for a 9.3 MeV, 7.5 MeV or 7.0 MeV threshold, respectively. We estimated the systematic error on the average solar neutrino flux from the absolute gain calibration as 7.5% for all combined data.

C.1.2. μ -e decay

We can also use μ -e decay as another calibration source. The spectrum of the decay electron is expressed as follows [ref C-1],

$$\frac{dN}{dE_e} = \frac{G^2}{12\pi^3} m_\mu^2 E_e^2 \left(3 - \frac{4E_e}{m_\mu}\right), \quad \left(E_e \leq \frac{m_\mu}{2}\right). \quad (\text{eq C-1})$$

The maximum energy and the average energy are 53 MeV and 37 MeV, respectively. This high energy calibration source supplements the Ni(n, γ)Ni' calibration for which the energy region is around 9 MeV.

Kamiokande observes stopping muons at a rate of ~ 400 events/day ($\sim 1/100$ of the total muon rate) and ~ 100 events/day in the fiducial volume (680 tons). We used the electrons, which are observed in the fiducial volume and decayed with the time difference of 1.5 μ sec to 20 μ sec from the parent muons for the energy calibration. This electron spectrum can be compared with the Monte Carlo simulation in which the energy scale is adjusted by the Ni(n, γ)Ni' calibration. The ratio of their mean pulse heights is obtained [ref 1-8],

$$\frac{\text{Data}(\mu \rightarrow e)}{\text{M.C.}(\mu \rightarrow e)} = 0.99 \pm 0.03,$$

where the error of the ratio is evaluated from the systematic error of the Ni(n, γ)Ni' calibration mentioned in subsection C.1.1. The pulse height distribution of the decay electron is well reproduced by the Monte Carlo simulation within the systematic error of the absolute energy calibration.

Unfortunately, we could not use the decay electrons for the absolute energy calibration in Kam-3, because a hit channel is disabled for 240 μ sec at most after the detection of a large pulse height such as a high energy muons.

C.2. Timing Calibration

The timing information of each PMT is essential for vertex reconstruction. The relative timing is obtained for each PMT-hit, but it is influenced by the pulse height of the hit PMT (the slewing effect). Hence, we need correction maps to adjust timing (T)

for different pulse heights (Q), for all channels. The map is called the TQ-map. The map further includes the effect of the difference of each PMT response, the time delay in cable. The slewing effect in master trigger discrimination is not important to the vertex reconstruction because it does not affect the relative timing of each hit within an event.

A light source, a N₂-laser, which emits intense light within a very short time was used to make the TQ-map. The flash timing can be accurately controlled and measured. The N₂ laser can emit intense 337 nm light with a pulse width less than 3 nsec. The configuration of the light source is shown in Fig. C.7. The N₂ laser is placed outside of the Kamiokande detector. For Kamiokande-2, the emitted light is attenuated by the combination of 5 filters and guided in the detector through a 50m quartz fiber. It is injected into a Pyrex container at the center of the detector. The solution of colloidal silica in the container diffuses the light which, subsequently, is emitted spherically. For Kamiokande-3, the wave length of the light is converted by dye (BPBD365, peak 366 nm, region 360-390 nm) to produce light closer to the Cherenkov spectrum. This light imitating Cherenkov spectrum is attenuated by 7 filters and then goes into MgO diffuser resolved in a 7 cm ϕ acrylic ball at the center of the detector and goes out spherically. The effective difference between Kam-2 and Kam-3 is the spectrum of the light: a monochromatic wave length (337 nm) for Kam-2 and a wave length spread by dye for Kam-3. Trigger timing is determined by the PIN photo-diode which gets laser light from a beam splitter set before the filters for light attenuation. Various filter configurations are used for each calibration so that all PMTs can receive photons with the required intensity ranging 0 to 300 photo-electrons. We subtract the time of flight from observed timing information and fill every hit in a two dimensional (photo-electrons vs. time) histogram (TQ-map). A typical pattern of the TQ-map is shown in Fig. C.8. We have correction parameter maps for all 948 inner-PMTs. Each PMT has two electronics circuits called the A channel and B channel in the Kam-3 case. They must be separately considered; therefore the number of parameter maps becomes 948 \times 2. Time spread (timing resolution) for various photo-electrons is already shown in

Fig. 4.11. The new PMTs, which have an improved dynode and focusing, achieved less than 3 nsec timing resolution at the one photo-electron level.

C.3. Transparency of the water

A PMT catches the Cherenkov light which traverses the water with an average path length of about 10m. A change of the water transparency causes a change in the pulse height through the attenuation of the light in the water. If the attenuation length is sufficiently long, its change will only slightly influence the PMT output. We want to stabilize the number of hit PMTs within a few percent accuracy. Therefore, we have monitored the water transparency by using through-going muons, continuously.

Neglecting the anisotropy of the cathode sensitivity (this is small factor as described in appendix A and section 4.5), charge output from the i -th PMT, Q_i , is expressed by

$$Q_i = A_i \frac{S(\theta_i)}{L_i} e^{-\frac{L_i}{L_0}}, \quad (\text{eq C-2})$$

where A_i is related to the total pulse height of the through-going muon, L_i the distance from the hit PMT to the point where muon emitted the Cherenkov photon, θ_i is the opening angle between the photon direction and the direction PMT $_i$ is facing, and $S(\theta_i)$ is the effective surface area of the PMT cathode from the direction of θ_i . We can measure the quantities Q_i , L_i , θ_i and $S(\theta_i)$, and therefore, can calculate the attenuation length of the Cherenkov light in the following way.

The expression (eq C-2) can be rewritten as

$$\log \frac{Q_i L_i}{S(\theta_i)} = -\frac{L_i}{L_0} + \log A_i, \quad (\text{eq C-3})$$

or with new parameters $x \equiv L_i$, $y \equiv \log \frac{Q_i L_i}{S(\theta_i)}$,

$$y = -\frac{1}{L_0} x + \log A_i. \quad (\text{eq C-4})$$

If we plot the observed data on the x - y plane, we can obtain a linear distribution like Fig. C.9. Then, the inverse of the slope factor is the attenuation length of the

Cherenkov light. We must note that the attenuation length is an averaged and approximate value, because a realistic expression of (eq C-2) is more complex,

$$Q = \int d\lambda A_i(\lambda) \frac{S(\theta)}{L} e^{-\frac{L}{L_0(\lambda)} + (\text{scattering})}. \quad (\text{eq C-5})$$

The transparencies thus obtained are plotted in Fig. C.10. It is found that the attenuation length is stable at a value of around 60 m.

The wave length dependence of the attenuation length used for the detector simulation in Kam-3 are shown in Fig. C.11 [ref C-2,C-3]. The detector simulation well reproduces the measured transparency. For example, if we apply the above procedure to the detector simulation used in Kam-3, the attenuation length becomes about 55m. We want to mention that the value 60 m is not limited by a basic physical process such as Rayleigh scattering. In Fig. C.11, long wave length light is mainly absorbed by water itself and we cannot extend the attenuation length in that region. Fortunately, the most valuable wave length for the quantum efficiency of the PMT is around 390 nm and the light attenuation in this efficient region is not dominated by the absorption by water. Short wave lengths seem to be mainly absorbed or scattered by impurities or dust in the water. The cross section of Rayleigh scattering (also shown in Fig. C.11) which mainly limits the transparency for short wave lengths ($\sigma \propto 1/\lambda^4$) is one order of magnitude smaller than the value used. We can, therefore, improve the attenuation length by purifying the water more and more.

One may worry about the small discrepancy of the attenuation length between the measured value (60 m) and the value used in the detector simulation (55 m). But, this effect turned out to be sufficiently small. The detector simulation is used for phenomena where photons traverse the water for only about 10m. Then the effect of this discrepancy to the energy scale will be less than

$$\left[\exp(-10/60) - \exp(-10/55) \right] / \exp(-10/60) = 1.5\%.$$

We want to control the effect of the discrepancy in the energy scale to be within 2.3%, which is the maximum contribution from the absolute energy calibration in the known systematic errors.

The attenuation length of the water has varied greatly in the early stage of Kam-2 as seen in the Fig. C.10. Hence, we have made a correction for the transparency when we calculate an energy in the Kam-2 analysis (see subsection 5.1.4). Fortunately, the attenuation length is quite stable and long enough (60 m) in Kam-3, we, therefore, do not make the correction.

C.4. Gain Stability

Drift of the PMT gain rarely influences the solar neutrino observation, for which we mainly use the number of hit PMTs for the energy scale. A 5% change of PMT gain induces about a 1% change in the number of hit PMTs. A gain change may instead affect the efficiency of the spallation cut used for the solar neutrino analysis because the spallation cut uses light output information for the parent muon selection.

The long term stability of the absolute energy scale has been traced by the $Ni(n,\gamma)Ni^{\dagger}$. But, this is a stability check for the number of hit PMTs. We have monitored the real time gain stability, indirectly, by the light output of penetrating muons. Fig. C.12 shows the observed number of photo-electrons per unit track-length (m) of a penetration muon. The average value of the number of photo-electrons increased by a factor of 1.27 due to light reflectors in Kam-3.

Strong light from a "flash tube" sometimes lowered the PMT gain. The cause of a flash tube is thought to be the leakage of water into the PMT. The resultant luminous light lowers the gain of surrounding PMTs. Such a gain change is at most 10% and its maximum change results in a 2% change of the absolute energy scale (number of hit PMTs). Thus, we did not use such data for the solar neutrino analysis. Event loss due to this cut amounted to about 5% even with the improvement of the H.V. monitor system described in subsection 4.5.3. A quick search for "flash tubes" is an important task for long term solar neutrino observation.

C.5. Dead tubes

The PMT was carefully designed to be waterproof. But unexpected damage to cables, incomplete water-tightness for the bleeder-chain and the cable exit, and cracks in the junction of the PMT and water proofing structure cause leaks of water. Such a PMT suddenly or gradually becomes a flash tube, which ends its life. As the number of dead tubes increases, the number of hit PMT for the same energy decreases.

There are also noisy PMTs and broken electronics channels which sometimes produce fake signals with very high rates. These channels accidentally increase the number of hit PMTs. Therefore, we masked such noisy channels in the analysis.

We must correct the energy scale considering the change of the number of masked channels. We used a correction factor, $(948 - N_0) / (948 - N_{\text{dead}})$ for the energy calculation, where N_0 is the number of dead or noisy PMTs (which were masked) at a fixed time and N_{dead} is the number of dead or noisy PMTs at the time when the event was observed. We replaced all the dead PMTs when we improved the Kamiokande detector from Kam-2 to Kam-3. Unfortunately, the sudden temperature change from $\sim 20^{\circ}\text{C}$ to $\sim 11^{\circ}\text{C}$ caused by filling up the tank with water made 70 PMTs go out of order instantly. After that the rate of dead PMTs was about 20 PMTs/year.

References

- [C-1] For example see F.Halzen and A.D.Martin, Quarks and Leptons: An Introductory Course in Modern Particle Physics, 1983 (John Wiley & Sons, Inc., New York 1984).
- [C-2] Sudbury Neutrino Observatory: feasibility study for a neutrino observatory based on a large heavy water detector deep underground, SNO-85-3.
- [C-3] T.I.Quickenden and J.A.Irvin, J.Chem.Phys. 72(1980)4416.

Appendix D. Future Prospects

The solar neutrino problem has not yet been resolved by the first generation experiments. What is needed in second generation experiments are (i) high statistics, (ii) neutral current measurement, and (iii) energy spectrum observation in the low energy region such as that of pp and ${}^7\text{Be}$ neutrinos as well as ${}^8\text{B}$ neutrinos.

(a) Super Kamiokande [ref 4-16,D-1]

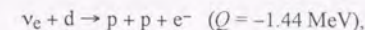
Super Kamiokande, the scaled up version of Kamiokande, is a high statistics experiment for which the expected event rate of ${}^8\text{B}$ neutrinos is 60 times larger than that in Kamiokande. Such high statistics is accomplished because of its large fiducial volume (the design value is 22,000 tons which gains a factor of 30 with respect to the Kamiokande fiducial volume: 680 tons) and its low analysis threshold (we aim for a 5 MeV threshold which gains a factor of 2 with respect to the Kamiokande analysis threshold: 7 MeV).

Super Kamiokande is fully funded and is now in the excavation stage. Half of the dome had already appeared in October 1993. The physics run will be started in April 1996. The characteristics and the estimated performance of Super Kamiokande is listed in table D-1 together with that for Kamiokande-3.

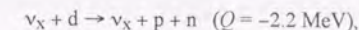
The high statistics measurement of ${}^8\text{B}$ solar neutrino spectrum will distinguish the non-adiabatic solution from the quasi-vacuum solution which are still alive under the neutrino oscillation hypothesis, and will determine the existence of time variations such as day/night, seasonal and 11 years. Then, it will be possible to test the remaining quasi-vacuum solutions using day/night flux information, and the just-so neutrino oscillation solution will be judged using seasonal variation (note that the just-so solution for two flavor mixing hypothesis has already been rejected at 90% C.L. in this thesis). Also, the 11 years' variability of the neutrino flux will tightly constrain the hybrid solutions.

(b) SNO [ref D-2]

Sudbury Neutrino Observatory (SNO) is also a high statistics experiment for ${}^8\text{B}$ neutrinos and is characterized by its ability to measure neutral current events. SNO is a heavy-water Cherenkov detector filled with 1,000 tons of D_2O and 1,700 tons of H_2O . The neutrinos are detected through the charged current interaction (CC),

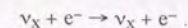


the neutral current interaction (NC),



(the resultant neutron is observed by (n,γ) reaction with the chlorine of MgCl_2 dissolved in D_2O .)

and also the neutrino-electron elastic scattering reaction (ES),



(the predicted count rate of ES is about one tenth of CC reaction, but this is the primary detection mechanism for H_2O detectors.)

The experimental site of SNO is located at the Creighton mine near Sudbury, Ontario, Canada. Excavation of the 10,000 m^3 dome had been finished in April 1993, and construction is scheduled to be completed in 1995.

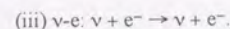
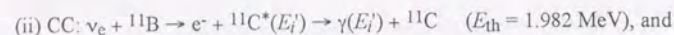
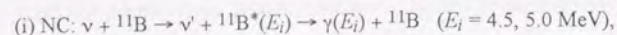
An excess of neutral current interaction rate over the charged current interaction rate can be a direct result of properties of neutrinos such as flavor mixing. This can determine whether the neutrino oscillation happens or not. The event rate of ${}^8\text{B}$ neutrinos is about half of that of Super Kamiokande, since the event rate of CC is about 10 times larger than ES and the fiducial mass is about one twentieth of super Kamiokande's.

(c) BOREX and BOREXINO [ref D-3]

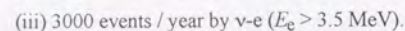
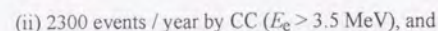
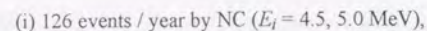
BOREX (Gran Sasso) can observe both charged current interactions and neutral current interactions with 2,000 tons (fiducial mass) of boron-loaded liquid scintillator which contains about 200 tons of natural boron. BOREXINO is the prototype

Appendix D. Future Prospects

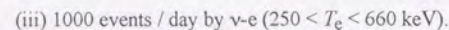
experiment of BOREX and it consists of 100 tons of liquid scintillator (about 10 tons of natural boron). Basic reactions in the detector are



Expected event rates (BOREX) from the SSM are



They also aim for a very low energy threshold (250 keV) for ${}^7\text{Be}$ neutrino observation, and the expected event rate for ${}^7\text{Be}$ neutrinos is



The high statistics measurement of ${}^7\text{Be}$ neutrinos can be achieved even by the BOREXINO detector (50 events / day). Small neutrino mass differences, $10^{-11}\text{eV}^2 < \delta m^2 < 10^{-8}\text{eV}^2$, could cause the measured flux of ${}^7\text{Be}$ neutrinos to oscillate with a period in the range of a week up to a year. Since ${}^7\text{Be}$ neutrinos have monochromatic energies (0.38, 0.86 MeV) and the flux is relatively larger than that of neutrinos from other reactions except for pp neutrinos, the time variation is not smeared by a continuous neutrino spectrum. Hence, the experiment is suitable to search for neutrino oscillation in such a parameter region. The importance of the neutral current measurement is the same for SNO.

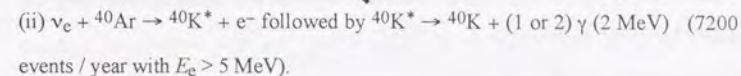
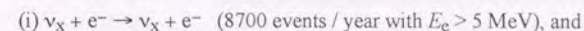
In order to observe ${}^7\text{Be}$ neutrinos, they must first overcome a severe requirement on radio-active impurity level in the scintillator (10^{-16}g/g).

(d) ICARUS, Indium, Hellaz and etc.

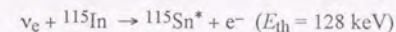
Many other solar neutrino experiments are proposed and are in R&D stage.

Appendix D. Future Prospects

ICARUS (Gran Sasso) [ref D-4] is a large (15,000 tons of) liquid argon time projection chamber which is geared forward high statistics observation of ${}^8\text{B}$ neutrinos through the reactions,



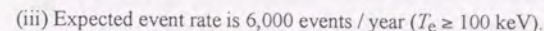
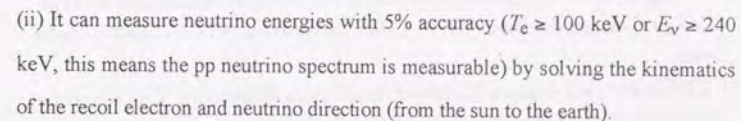
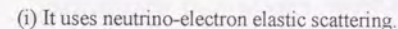
Indium experiments have the potential to observe the energy spectrum of pp neutrinos [ref D-5] through the reaction,



followed by ${}^{115}\text{Sn}^* \rightarrow {}^{115}\text{Sn} + \gamma$ (116 keV) or $\text{IT} + \gamma$ (498 keV) ($T_{1/2} = 3.26$ μsec).

But in order to overcome the difficulty of the background from indium itself (${}^{115}\text{In} \rightarrow {}^{115}\text{Sn} + e^-$, $E_{\text{max}} = 486$ keV, 0.22 decays/sec/g), one [ref D-6] has changed the goal of the detector development to the observation of ${}^7\text{Be}$ and pep neutrinos. The required performance will be accomplished by an indium loaded liquid scintillator. But the estimated event rate for ${}^7\text{Be}$ neutrinos from the SSM is only about 70 events / year / 10 tons of indium.

The Recently proposed Hellaz experiment [ref D-7] may be one of the ultimate solar neutrino experiments. It is a large Helium gas time projection chamber (1900m^3 at 10 bar and 77°K weighing 12 tons). The salient characteristics of Hellaz are as follows.



Hellaz can measure the solar neutrino spectrum in almost the entire energy region and with high statistics, especially in the low energy region, which will supplement the

Appendix D. Future Prospects

precise measurement of the ^8B neutrino spectrum by Super Kamiokande, SNO, BOREX and ICARUS.

(We do not discuss it here, but there are great activities on new solar neutrino experiments at Baksan. They are briefly summarized in [ref D-8].)

These second and third generation solar neutrino experiments can provide accurate neutrino spectrum information in the entire energy region and moreover neutrino oscillation information through neutral current measurement. Also, it must be noted that the SNO and the BOREX / BOREXINO experiments have a much greater ability to observe the $\bar{\nu}_e$ flux than Kamiokande. This new information will resolve the complicated solar neutrino problem in near future. We are looking forward to the completion of Super-Kamiokande!

References

- [D-1] M.Takita, Proceedings of the International Symposium on Neutrino Astrophysics, Takayama/Kamioka, Japan, 1992, p135, edited by Y.Suzuki and K.Nakamura (Universal Academy Press, Inc. Tokyo, Japan 1993).
- [D-2] H.H.Chen, Phys.Rev.Lett. **55**(1985)1534; H.H.Chen, NIM **A264**(1988)48; "Scientific and Technical Description of the Mark II SNO Detector" edited by E.W.Beier and D.Sinclair, SNO-89-15, October 1989; G.T.Evan, Proceedings of the International Symposium on Neutrino Astrophysics, Takayama/Kamioka, Japan, 1992, p147, edited by Y.Suzuki and K.Nakamura (Universal Academy Press, Inc. Tokyo, Japan 1993).
- [D-3] R.S.Raghavan, S.Pakvasa and B.A.Brown, Phys.Rev.Lett. **57**(1986)1801; R.S.Raghavan and S.Pakvasa, Phys.Rev. **D37**(1988)849; R.S.Raghavan et al., "Design Concepts for Borex", AT&T Bell Laboratories, ATT-BX-88-01, March 1988.
- [D-4] CERN-Harvard-Milano-Padova-Roma-Tokyo-Wisconsin Collaboration, INFN/AE-85/7, Frascati, 1985; ICARUS Collaboration, ICARUS I: An Optimized Real Time Detector of Solar Neutrinos, LNF-89/005(R), 1989.
- [D-5] R.S.Raghavan, Phys.Rev.Lett. **37**(1976)259; L.Pfeiffer et al., Phys.Rev.Lett. **41**(1978)63, Phys.Rev. **C19**(1979)1035; A.G.D.Payne and N.E.Booth, NIM **A288**(1990)632; see references in N.E.Booth, Proceedings of the International

Appendix D. Future Prospects

Symposium on Neutrino Astrophysics, Takayama/Kamioka, Japan, 1992, p177, edited by Y.Suzuki and K.Nakamura (Universal Academy Press, Inc. Tokyo, Japan 1993).

- [D-6] A.K.Drukier and R.Nest, NIM **A239**(1985)605; Y.Suzuki et al., NIM **A293**(1990)615; A de Bellefon et al., "Feasibility study of an Indium Scintillator Solar Neutrino Experiment", DPhPE 89-17, Saclay, 1989; K.Inoue et al., ICRR-Report-252-91-21, 1991, ICRR University of Tokyo.
- [D-7] J.Seguino, T.Ypsilantis and A.Zichichi, LPC 92-31, College de France, 12/8/92; G.Laurenti et al., CERN/LAA/PC/93-10, 24/2/1993.
- [D-8] A.Kopylov, Proceedings of the International Symposium on Neutrino Astrophysics, Takayama/Kamioka, Japan, 1992, p157, edited by Y.Suzuki and K.Nakamura (Universal Academy Press, Inc. Tokyo, Japan 1993).